Numerical Modeling of Floater Dynamics of a FOWT

For Wind Tunnel Hardware-in-the-Loop Testing

Matthijs de Lange

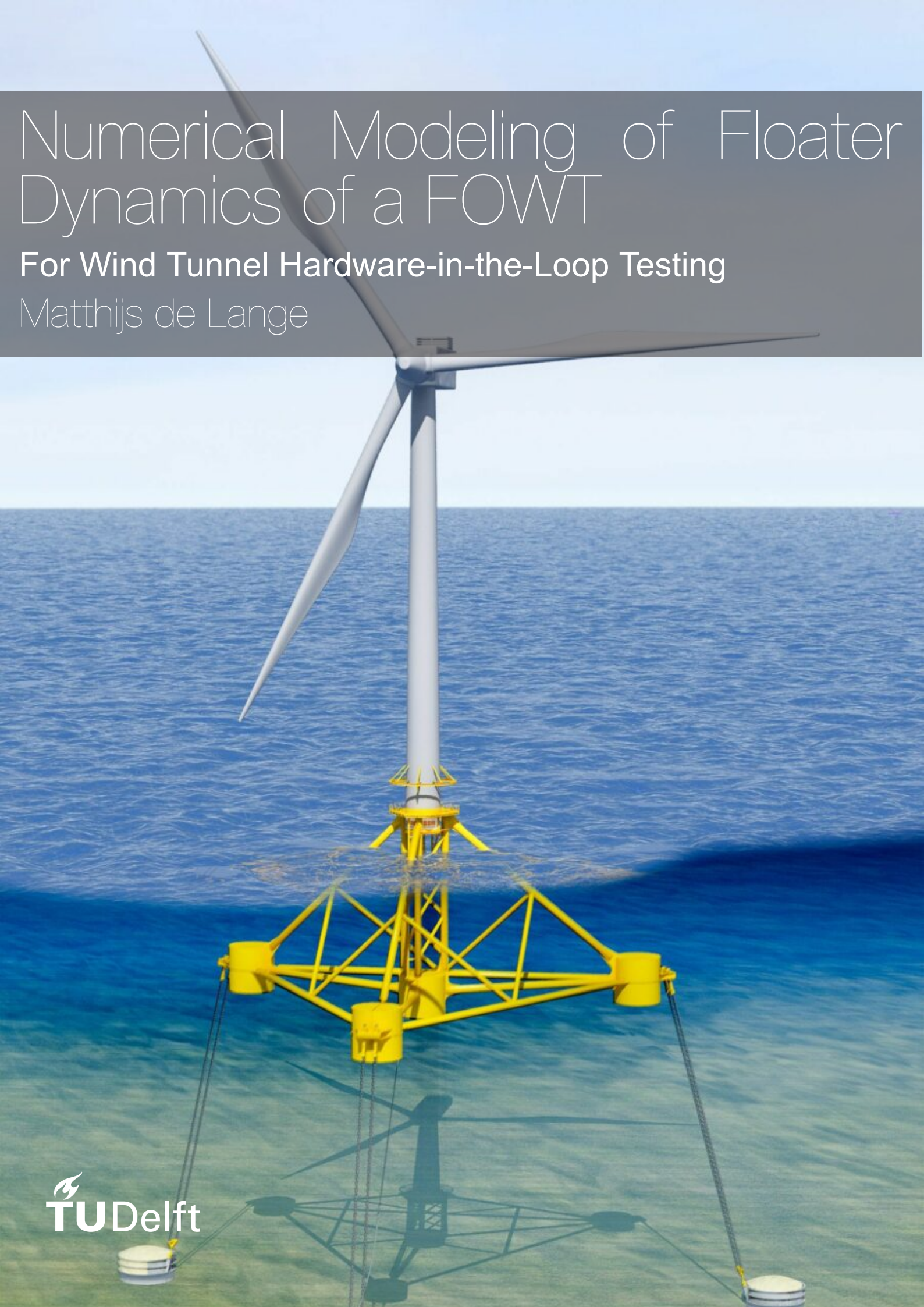

TU Delft

Numerical Modeling of Floater Dynamics of a FOWT

For Wind Tunnel Hardware-in-the-Loop Testing

by

Matthijs de Lange

To obtain the degree of Master of Science in Aerospace Engineering
at the Delft University of Technology, Faculty of Aerospace Engineering, Wind Energy Group
to be defended publicly on Friday July 18, 2025 at 13:00.

Student number: 4785487
Project duration: September 1, 2024 – July 18, 2025
Thesis committee: Prof. Dr. Ir. L.L.M. Veldhuis, TU Delft, Committee chair
Dr. Ir. F. Taruffi, TU Delft, Daily supervisor
Dr. Ing. S. Schreier, TU Delft, Committee member

An electronic version of this thesis is available at http://repository.tudelft.nl/.
Cover image is adopted from SBM Offshore, 2021

TU Delft

Preface

This thesis has been written as partial fulfillment to obtain the degree of Master of Science in Aerospace Engineering. It reflects the results of 9 months of hard work, dedication, and personal development. Working on this thesis has been both intellectually demanding and rewarding. It has taught me about the many aspects and challenges of real-time simulation, hardware-in-the-loop wind tunnel experiments, and floating offshore wind turbines, and given me the opportunity to engage with complex challenges and contribute to ongoing academic discussions.

I would like to thank my daily supervisor, Dr. Federico Taruffi, for the guidance and advice he gave me during the thesis. His experience has taught me about the many aspects of Hardware-in-the-Loop simulation, which has been extremely helpful in the completion of this thesis and has made it a joy to do. Additionally, I would like to thank Carlos and Mathis for their help, presence, and advice during the wind-tunnel campaign. I also would like to thank Prof.dr.ir. Leo Veldhuis and Dr. Sebastian Schreier for being part of my thesis committee.

Finally, I would like to thank my family and friends, who offered both words of encouragement and moments of welcome distraction from the ever-present work ahead.

Matthijs de Lange
Delft, July 2025

Summary

Offshore wind energy generation is increasing all around the world. Consequently, developers find themselves in deeper and deeper waters. Bottom-fixed wind turbines perform great in shallow waters; however, they become economically unfeasible after 50-60 meters of water depth, found in many places around the world close to large population centers such as the United States, China, Korea, and Japan. Floating wind turbines could offer a solution here, as they can be used in much deeper waters.

Floating offshore wind turbines have challenges of their own. They are subject to much larger motions compared to bottom-fixed turbines, and these motions affect aero-, structural-, and control dynamics. These effects are hard to study experimentally; full-scale experiments are costly and only possible after model-scale experiments have been executed. However, scaled models have their own challenges; the hydrodynamic and aerodynamic effects have different scaling similitudes, leading to a mismatch in scaling factors. A solution to this is to perform hybrid experiments, where one domain is simulated numerically, and force/motion is applied by an actuator. Hardware-in-the-Loop (HIL) is a specific type of hybrid experiment in which there is an emphasis on the feedback between the numerically simulated and physical system.

In this study, a HIL methodology is used to numerically simulate the hydrodynamics and floating motion of a floating offshore wind turbine (FOWT), to be able to do wind tunnel experiments and analyze the effects of combined wind-wave action. A scaled wind turbine model is placed on top of a Hexapod, a robot that is able to actuate the six degrees of freedom (6-DOF) motion of the FOWT. The scaled wind turbine model has a fixed (zero) pitch rotor, designed for low-Reynolds-number wind speeds, that is designed to be thrust-matched to the full-scale model. Force and acceleration sensors are used to determine the aerodynamic forces and torques on the rotor, which are input to the numerical simulation. The numerical simulation solves the equation of motion of the floating system, taking into account radiation forces, user-defined sea state, mooring system, and the aerodynamic forces and torques.

One challenge in HIL simulation is that the simulation has to be in real-time. This puts a computational limit on the fidelity of the numerical simulation. By increasing the fidelity of the simulation, computational time per timestep increases, and the size of the timestep decreases, which means more computational power is required to be able to simulate in real-time. This creates a fine balance between fidelity and computational efficiency that is not trivial to maintain.

The scope of this thesis is to model and analyze the effects of different mooring line representations, each having a higher level of fidelity, in a linear, quasi-static, and dynamic approach. Additionally, the fidelity of the sea-state is increased by including the second-order wave forces, as determined by Newman's Approximation. The modeling approach is verified against OpenFast, a mid-fidelity engineering tool widely used in industry, for the numerical simulation of FOWTs.

The verified models are subsequently used in wind tunnel experiments to analyse the effect of aerodynamic forces on wind-wave action, as well as the effect of second-order wave excitation forces on floater motion. The dynamic mooring line representation was, unfortunately, too computationally expensive to be able to test in real-time simulation. However, it is verified numerically, and some possible solutions are offered for future research. The analysis of second-order forces shows that they significantly affect the floater motion, especially in surging and pitching motion, leading to higher amplitude oscillation in mooring tensions as well. The analysis of aerodynamic forcing in operational sea-states finds that in mellow sea-states, aerodynamic forcing aggravates the motion of the FOWT. However, as sea-state roughness increases, the aerodynamic forcing starts to act as a dampening effect. Additionally, a more fundamental study is done on the effect of wind speed on aerodynamic damping and natural frequency for a range of wind speeds. Decay tests are done in surging, pitching, and yawing motions. The results show that increasing wind speeds greatly affect the damping ratio in pitching in yawing motion, and slightly less so in surging motion.

Nomenclature

List of Abbreviations

Abbreviation	Definition
BEM	Blade Element Momentum
CFD	Computational Fluid Dynamics
CL	Closed Loop
CoM	Center of Mass
CPSD	Cross Probability Spectral Density
DOF	Degree Of Freedom
EOM	Equation of Motion
FEA	Finite Element Analysis
FOWT	Floating Offshore Wind Turbine
HIL/SIL	Hardware-in-the-Loop/Software-in-the-Loop
JONSWAP	Joint North Sea Wave Project
LM	Lumped Mass
MAP	Mooring Analysis Program
NREL	National Renewable Energy Laboratory
OL	Open Loop
O&M	Operations & Maintenance
QS	Quasi-static
QTF	Quadratic Transfer Function
RAO	Response Amplitude Operator
RNA	Rotor Nacelle Assembly
SWL	Still Water Level
TLP	Tension Leg Platform
TSR	Tip Speed Ratio
WAMIT	Wave Analysis MIT
WB	Wave-Basin

List of Symbols

Latin Symbol	Definition	Unit
a	Amplitude	$-$
f_n	Natural Frequency	Hz
Fr	Froude Number	$-$
$F_k^-(\omega_m, \omega_m)$	Diagonal Terms of Difference-Frequency QTF	N/m
H_s	Significant Wave Height	m
$K(\omega)$	Response Amplitude Operator as a function of angular frequency	N/m
L	Length	m
r	Radius	m
Re	Reynolds Number	$-$
S_{xx}	Power Spectral Density in surge	m^2/Hz
$S_{\theta\theta}$	Power Spectral Density in pitch	deg^2/Hz
S_{Fx}	Cross Power Spectral Density of aerodynamic force and surge	$N.m/Hz$
$S_{T\theta}$	Cross Power Spectral Density of aerodynamic moment and pitch	$N.m.\mathrm{deg}/Hz$
T_p	Peak Period	s
U	Velocity	m/s
x	Floater position in Surge	m

y	Floater position in Sway	m
z	Floater position in Heave	m

Greek Symbol	Definition	Unit
γ^r	Peak Enhancement Factor	$-$
ζ	Damping ratio	$-$
η	Wave Elevation	m
σ	Spectral Width Parameter	$-$
ϕ	Floater Inclination in Roll	deg
ϕ_i	Phase Angle	deg
θ	Floater Inclination in Pitch	deg
θ_i	Random Phase Angle of Stochastic Process	deg
ψ	Floater Inclination in Yaw	deg
ω	Angular Frequency	rad/s
Ω	Rotational Velocity	rad/s

Matrices	Definition
$\mathbf{A}$	Added Mass Matrix
$\mathbf{D^{(1)}}$	Linear Damping Matrix
$\mathbf{D^{(2)}}$	Quadratic Damping Matrix
$\mathbf{K}$	Linear Stiffness Matrix
$\mathbf{R}$	Rotational Matrix
$\mathbf{R_x}$	Rotational Matrix around x-axis
$\mathbf{R_y}$	Rotational Matrix around y-axis
$\mathbf{R_z}$	Rotational Matrix around z-axis
$\mathbf{x}$	State Vector = $[x\ y\ z\ \phi\ \theta\ \psi]^T$
$\dot{\mathbf{x}}$	Velocity State Vector, time derivative of $\mathbf{x}$
$\ddot{\mathbf{x}}$	Acceleration State Vector, time derivative of $\dot{\mathbf{x}}$

Contents

List of Figures

List of Tables

1

Introduction

Offshore wind energy generation has steadily increased over the last decade, but in water depths of more than 50 meters, bottom-fixed wind turbines are no longer economically feasible due to the increasing cost of offshore foundations. Floating wind turbines offer a solution for increasing water depths, opening up locations where offshore wind turbines were previously impractical. In Europe, this opens up many locations in the Atlantic and Mediterranean. Additionally, it opens up many locations outside of Europe, close to large population centers, where bottom-fixed offshore wind turbines are not feasible. This includes the US (west and east coast), Japan, Korea, and China (Arapogianni et al., 2013; Barooni et al., 2022; Henderson & Witcher, 2010).

There are many challenges to overcome, however. A floating structure is required to give buoyancy and stability to the turbine; nevertheless, the system will encounter much larger motions than its bottom-fixed counterparts. These floating system motions influence the aerodynamics of the rotor, leading to instabilities and generally inducing a loss of power production (Butterfield et al., 2007).

Additionally, the operation and maintenance of FOWTs require robust port infrastructure, which proves to be a large hurdle to overcome. Currently, the maintenance on floating wind turbines is done in port, but as floating wind parks move farther offshore, it can become prohibitively expensive to tow the individual turbines all the way to port for maintenance. However, on-site maintenance requires the development of new tools and support vessels. All in all, the installation, operation, and maintenance (O&M) of floating wind is more complex and costly than its bottom-fixed counterparts. The extra costs due to the floater, electrical power system, and O&M are, to an extent, offset due to the higher wind speeds found at deeper water depths.

The three most commonly used floating configurations are: Spar-buoy, Semi-submersibles, and Tension Leg Platforms (TLP). These floater types differ in the stabilizing mechanism they use to stay afloat (C. Wang et al., 2010). Spar-buoy-type floaters use a gravity-based stabilizing system. The floater consists of a large ballast with its center of mass well below the center of buoyancy of the system, ensuring that the system remains upright due to a large righting moment arm. The floating structure is connected to the seabed using catenary or taut mooring lines to ensure that the structure does not float away. Semi-submersible floaters consist of multiple large columns, connected to each other by slender members. The stability of the system is generated by the columns, and a catenary mooring line system is used to stay in place. The TLP-type floater consists of a floating platform that is connected to the seabed using taut mooring lines. The stability of the system is derived from the tension in the mooring lines. This type of floater can provide lower motion amplitudes than the other floater types (H. Wang, 2022).

In the early design stages of FOWTs, numerical simulations play a fundamental role. The design of FOWTs consists of numerical simulations (low to mid-fidelity) and experimental testing (mid to high-fidelity). In early development, industry uses numerical models for first indications of feasibility, power production, system motions & loading. Experimental testing is required in later stages as a higher fidelity testing method. Furthermore, many numerical models neglect certain effects for the sake of

simplicity or computational efficiency, or they fail altogether due to instabilities; experimental testing is thus required to validate these numerical tools and provide a deeper understanding of the physical system (Hmedi et al., 2023).

The experimental testing of floating wind turbines offers its own challenges. Scaled experiments regarding hydrodynamics need to follow Froude number similitude to accurately scale the dominant loading. The aerodynamic loads, however, should be scaled according to Reynolds number similitude. This mismatch in scaling factors leads to a situation where either the hydrodynamic or the aerodynamic loading is not representative of the real loading encountered by the full-scale system (Taruffi et al., 2024). Multiple studies have been carried out to create a test environment that respects both the Reynolds and Froude scaling in wave basin tests. Traditional wave-basin experiments account for this mismatch in scaling in various ways. For instance, by making use of Froude-scaled wind, resulting in higher aerodynamic forces and higher Reynolds numbers, though this also affects other aerodynamic aspects, because the tip speed ratio of the design will not be maintained. Another possible solution entails the use of a different airfoil geometry for the rotor blades, which performs better at low Reynolds numbers.

Recently, Hybrid testing has proven to be a very useful technique for experimental testing of FOWTs. In hybrid testing, a part of the physical system is replaced by sensors, numerical (real-time) simulation, and actuators. Hybrid testing methodologies can be applied to FOWTs in two ways. Firstly, in HIL Wave-basin (WB) experiments, the earliest campaigns replaced the rotor with cables to emulate a static aerodynamic load on the rotor. Later studies used drag discs, propellers, and multi-fan setups to replicate rotor thrust or Froude-scaled rotors with high wind speeds to match the rotor thrust. The second approach consists of wind tunnel experiments, where the floater motion and wave-induced forces are modeled numerically and applied to the turbine system by a robot at the base of the turbine model. This allows for a detailed aerodynamic analysis that is generally not possible in WB experiments, due to difficulty in accurately recreating the non-linearities in aerodynamic forcing.

Hybrid testing is not without its own challenges. A requirement for hybrid simulation is that it has to be run in real-time, which creates problems when the computational load is increased past a certain point. There is an intricate balance between fidelity and computational efficiency that is difficult to maintain. At model scales, as fidelity increases, the size of the time step decreases, requiring more computational power to be able to simulate in real-time. One of the motivations of this study is to analyze the effects of increased fidelity in HIL wind tunnel experiments and to see how this affects computational efficiency and real-time simulation. Additionally, it provides an opportunity to execute combined wind-wave tests to analyze aerodynamic effects on the FOWT.

The report is structured as follows. A literature study is done in chapter 2, which discusses the varying aspects of numerical simulation of floating turbines, challenges of (real-time) HIL simulation, and the research objective and research questions central to this study. The study itself will focus on three distinct parts. Firstly, it will discuss the numerical modeling aspects of HIL simulation that are the foundation of this study, as presented in chapter 3. Secondly, these numerical models will be verified using OpenFast as a benchmark, a numerical tool used widely in industry for the numerical modeling of FOWTs (Jonkman et al., 2024), in chapter 4. Finally, the verified models will be used in HIL wind tunnel experiments, where combined effects of wind-wave action will be tested, as well as aerodynamic effects on system dynamics, in chapter 5.

2

Literature Study

A specific method of hybrid testing is Hardware-in-the-loop (HIL) testing. HIL testing puts emphasis on the feedback between the numerical simulation and physical loading on the system. With regards to FOWTs, this means that the floater dynamics lead to changes in aerodynamic loading, but also that the aerodynamic loading on the turbine leads to changes in floater dynamics. So while prescribed motion of the floater (such as sinusoidal motion) in a wind tunnel is considered hybrid testing, it is not considered HIL testing. For HIL testing there needs to be a feedback between the physical and numerical loading & motion. In literature it can also be found under the name Software-in-the-loop (SIL). The process of actuators and sensors can be partially simulated, because the sensors and control hardware often form integrated systems and actuators are difficult to simulate in real time (Bacic, 2005; Isermann et al., 1999).

In the second half of the 20th century, HIL simulation was first utilized in the aviation industry for real time flight simulation (Isermann et al., 1999). HIL simulation is particularly useful in this industry due to the long development times, expensive prototype costs and potential danger in control system testing with real prototypes. Having proven the usefulness in aviation, other industries were quick to adapt the HIL methodology. Currently, HIL simulation has been used in a variety of industries.

For instance, HIL has been used in train development for the testing of pantograph dynamics (Collina et al., 2004; Facchinetti & Mauri, 2009; Gil et al., 2024) and wheel slide protection systems (Pugi et al., 2023). Similarly, the automotive industry has adopted HIL simulation for a variety of purposes, including (but not limited to) anti-lock braking systems (K. Lee et al., 2004; Nauri et al., 2020; Suh et al., 1998), testing of longitudinal vehicle dynamics (Verma et al., 2008), engine control (Isermann et al., 1999) and hybrid electric/electric vehicle battery testing (Petersheim & Brennan, 2009)

HIL methodology also proves to be useful in Power and energy systems, more commonly referred to as Power Hardware in the Loop (PHIL) (Edrington et al., 2015; Lauss et al., 2015). Applications of PHIL include battery management system testing (Fleischer et al., 2016) and microgrid simulation (Limpaecher et al., 2017; J. Wang et al., 2014).

In the last 20 years HIL testing has has been extensively used in the Wind energy industry, for instance for testing of power control (Puleva et al., 2016) and certification testing (Kaven et al., 2022). Particularly interesting are the HIL studies done on FOWTs. HIL simulation proves to be especially viable in this research area due to the high costs of prototyping, and difficulty creating a representative physical environment. There are two variations for HIL simulation of FOWTs, wave-basin testing (Carmo et al., 2024; de Ridder et al., 2014; Du et al., 2016; Fontanella et al., 2020; Fowler et al., 2013; Hall et al., 2018; Martin et al., 2014) and wind tunnel testing (Ambrosini et al., 2020; Bayati et al., 2013; Fontanella, Facchinetti, et al., 2023; Giberti & Ferrari, 2015; Thinakaran, 2024).

These methods differ in the part of the physical system that is simulated. Wave-basin testing entails the testing of a scale model floater and turbine tower, where the aerodynamic loading of the rotor is simulated numerically and applied by actuators such as fans or cables. The wave-basin tank then

applies real wave loading, and the (scale model) physical floater reacts as the real system would due to combined hydrodynamic and aerodynamic loading.

In wind tunnel testing, the wave loading and floater dynamics are replaced with numerical simulation; these forces and moments are then applied to an actuation system at the base of the turbine tower model. Wind tunnel experiments provide valuable insight into the influence of the floating motion on the aerodynamics of the turbine. Indeed, the choice of wind tunnel or wave-basin experiment comes down to what part of the system one wants to accurately study. To be able to accurately study aerodynamic phenomena or floater dynamics/mooring line forces in a HIL experiment, one needs to make sure that the numerical simulation is accurate enough to represent a real scenario.

2.1. Wave Basin Experiments

Heather R. Martin et al. suggest a set of rules that determine the scaling of the floating offshore wind turbine (Martin et al., 2014). The suggested rules are as follows:

- **Froude number model scaling** is commonly used in offshore engineering, as the gravity and inertial forces are correctly scaled, which are the most dominant factors in hydrodynamics. The Froude number is defined in Equation 2.1, where u is the wave propagation velocity, g is the local gravitational acceleration, and L is the characteristic length.

$$Fr = \frac{u}{\sqrt{gL}} \tag{2.1}$$

- **Froude-scaled wind** ensures that the ratio of wave to wind forces is consistent with the reference model. This method, however, can only be used in cases where the aerodynamics are insensitive to Reynolds number.
- **Tip Speed Ratio (TSR) similitude** Employing the same TSR in the model as the reference makes sure that the rotational speed is correctly scaled, in tandem with the natural frequencies of rotor imbalance or tower interaction. Additionally, turbine thrust and torque will be correctly scaled if TSR similitude is employed along a Froude-scaled wind. The TSR is defined in Equation 2.2, where Ω is the rotational velocity of the rotor, r is the rotor radius and U is the wind velocity.

$$TSR = \frac{\Omega r}{U} \tag{2.2}$$

The Reynolds number difference between reference and model scale does change significantly, the initial study in the paper by Heather R. Martin et al. suggests that at a scale factor of λ = 50, the peak Power coefficient is off by an order of magnitude at only half the TSR, indicating a greatly reduced rotor performance (Martin et al., 2014). The second half of their paper offers three possible solutions to the Reynolds number dissimilitude, which aims to establish the correct rotor thrust.

- Increase model inflow wind speed.
- Addition of leading edge roughness on the model blade to reattach the boundary layer around the blade.
- Use a different blade geometry specifically designed for low-Reynolds use to capture the correct thrust forces at the lower Reynolds number.

The increase of model inflow wind speed breaks the TSR similitude between the model and the reference. However, tests show that the wind turbine damping is not greatly affected by the increase in wind speed, though this might not be true for all damping effects. The addition of leading edge roughness is advised to be used as a complementary measure rather than as a solution on its own. The final recommendation is that a specifically Reynolds number designed blade is used in tandem with the Froude scaled winds to be able to match the required thrust forces, as this will better capture wind turbine damping effects. Similar methods of thrust matching by using a redesigned turbine blade were also employed in (de Ridder et al., 2014; Du et al., 2016; Fowler et al., 2013).

A different approach can be employed, where instead of using a scaled rotor with physical wind inflow, a hybrid numerical setup is used for the aerodynamic loading (Carmo et al., 2024). In this approach, a HIL method is used to emulate the aerodynamic thrust by the rotor using a numerical simulation of the aerodynamic forces and moments, and applying them to the model using a single ducted propeller. Other studies have used different actuation methods such as cables and winches (Bachynski et al., 2016; Sauder et al., 2016).

2.2. Modeling Techniques for HIL Wind Tunnel Testing

HIL wind tunnel testing of FOWTs is quite a new technique, first developed at Politecnico di Milano (Ambrosini et al., 2020; Giberti & Ferrari, 2015). (Ambrosini et al., 2020) provides an overview of some of the challenges and technical aspects associated with HIL testing of FOWTs in a wind tunnel. Their experimental setup has a 2-DOF system in the surge and pitch direction. They note five distinct aspects that ought to be taken into account when designing HIL wind tunnel experimental tests. Though these problems are specific to their experimental setup, it is important to take note of these issues.

- **Scaling issues** Scaling proves to be challenging due to the number of devices that need to be installed on the turbine while also accurately representing the natural frequency, mass, moment of inertia, and center of mass of the system. Additionally, difficulties arise in accurately measuring the forces on the system, as the load cell and acceleration measurements are taken at the bottom of the tower, thus measuring the inertial loads of the system in tandem with the desired aerodynamic loading.
- **Numerical issues** In real-time simulation, computational efficiency is of the essence. The implementation of hydrodynamic forcing was done in the frequency domain, and each time step, an inverse cosine Fourier transform is performed to get the contribution in the time domain. Additionally, time domain wave history and time step size are crucial for both the final solution as well as simulation stability.
- **System characterization** A series of experimental tests were executed to determine the required inertial properties: Mass, moment of inertia, and center of gravity. This is done experimentally to account for design and manufacturing discrepancies. The values found in the process account for the tower, turbine, and dynamometer.
- **Force correction** For the numerical simulation of the floater, accurate values for aerodynamic and inertial loading are required. As mentioned before, the load cell is at the bottom of the tower, measuring both inertial loads and aerodynamic loads at the same time. It would be possible to measure the contributions directly if a Froude scaling were applied (thus the acceleration scaling is equal to 1), and mass, inertia, and length are all perfectly scaled. If these conditions are not met, a force correction has to be applied to calculate the contribution of the aerodynamic forces. This requires accurate measurements of the mass and inertia of the tower and Rotor-Nacelle Assembly (RNA).
- **Measurement & Signal processing** The design of the turbine model requires filtering of the output response due to the location of the eigen frequency of the fore-aft bending moment on the frequency spectrum. This additional filter introduces a phase shift and a time delay.

2.2.1. Force correction Methodology

Two force correction methods are mentioned in (Ambrosini et al., 2020), A measured acceleration approach and a simulated state approach. The measured acceleration approach makes use of two accelerometers, one installed at the bottom of the tower and one installed at the top. With both acceleration measurements, the force correction can be calculated. The acceleration is measured at the same time as the force signal from the dynamometer; thus, no additional time lag is generated using this method. The simulated state approach works under the assumption that simulated positions and accelerations accurately represent the real positions and accelerations of the system. If a time delay is introduced to the system in actuation or measurement systems, then this method can introduce an extra time delay that acts like positive or negative damping.

This extra damping can be negated by synchronizing the force correction with the force signal. The

time delay introduced per actuator needs to be known. This can be acquired by executing a number of imposed motion tests where only one actuator is used at a time. The simulated state input signal can then be synchronized to the physical model by a series of filters and time delays, as described in (Ambrosini et al., 2020).

The proposed methods were used in a 2-DOF system, which greatly simplifies some of the dynamics. Nonetheless, the methods used are not solely applicable to 2-degree-of-freedom systems and can be extended for use in full 6-DOF experiments. M. Belloli et al. also make use of a simulated state approach in their 6-DOF wind tunnel test, mentioning that accurate measurement of the current position and acceleration is a tough task (Belloli et al., 2020).

2.2.2. Aerodynamic Damping

The usage of HIL testing in wind turbine testing allows for the experimental analysis of the effects of aerodynamic damping on wind turbine operations. For wind turbines, aerodynamic damping forms the single largest contribution to damping in the system.(C. Chen & Duffour, 2018) have found that aerodynamic damping values, both predicted and measured, vary substantially across multiple studies of on- and offshore wind turbines. It is clear however, that the damping in fore-aft motion is an order of magnitude larger than that in side-to-side motion.

J. Chen and Hu, 2018 have done experimental wave-basin tests on the effect of aerodynamic damping on an OC4 semi-submersible floating wind turbine. In their test, they did not implement a HIL approach, however. They chose to do model-scale tests in a wave-basin, with a Froude-scaled model, leading to a non-Reynolds-scaled blade. To match the rotor thrust, they employed a 'adjusting wind speed method'. In their experimental tests, they compared wave cases without wind against wave cases with varying levels of inflow wind. They found that the aerodynamic damping results in a reduction in resonant response at the low-frequency range, with little effect in the wave-frequency range. Additionally, they found in comparison between parked conditions and operating conditions that the induction induced by the rotor impacts the aerodynamic damping.

Yang et al., 2023 have done frequency domain analytical tests, which they verified versus experimental wave-basin model tests. In the paper, they discuss the dynamic characteristics of aerodynamic damping in surge and pitching motion. They note an increase in aerodynamic damping as wind speed increases up until rated wind speed, after which the damping ratio decreases again for increasing wind speed, in both surging and pitching motion.

Besides experimental studies, there are also analytical studies that have analyzed the effect of aerodynamic damping. Meng et al., 2022 have done a numerical study based on an aerodynamic damping matrix derived from the linearisation of aerodynamic forces at the tower top. They make use of the Blade Element Momentum (BEM) theory to calculate the aerodynamic forces on individual blades. The summation of total forces at the tower top results in an aerodynamic damping matrix in 6-DOF. They found that aerodynamic damping has a great influence on the resonant motion response in surge, pitch, and yaw.

2.2.3. Hydrodynamic Modeling

In HIL wind tunnel tests, the floater dynamics and wave forcing need to be simulated numerically. The simulation can be formulated in a number of different ways, with varying degrees of fidelity. The different aspects of numerical modeling of the hydrodynamics of floating structures are discussed in the next chapter separately, concluding with a summary of hydrodynamic aspects used in wind tunnel HIL experimental setups.

2.3. Hydrodynamics

This section covers some of the aspects of numerically modeling hydrodynamic forces and floater dynamics. The first section will go over some of the distinguishable components of the hydrodynamic forcing on a floating structure. subsection 2.3.2-2.3.4 covers formulations for the modeling of hydrodynamic forces used in literature. subsection 2.3.5 discusses the effect of higher-order hydrodynamic forces. In subsection 2.3.6, the use of CFD modeling in the simulation of hydrodynamic forcing on floating structures is discussed. subsection 2.3.7 presents different formulations for the simulation of

regular and irregular waves, and wave spectra. subsection 2.3.8 discusses different approaches for the numerical modeling of mooring lines. Finally, subsection 2.3.9 discusses the hydrodynamic formulations used in previous wind tunnel HIL experimental setups for the study of FOWTs.

2.3.1. Hydrodynamics Force Components

The hydrodynamic forcing on a floating structure can be separated into different contributions. The following contributions can be distinguished.

- **Froude-Krylov** The Froude-Krylov (FK) force is generated due to the unsteady pressure field generated by the undisturbed waves.
- **Diffraction** The diffraction force comes from the effect that the structure has on the incident wave, distorting the wave field.
- **Radiation** Radiation forces are generated due to an oscillating body in still water.
- **Viscous drag** Viscous drag is generated due to the viscosity of the fluid. The force is proportional and opposite to the relative velocity between the structure and the fluid, leading to a damping force.
- **Vortex-Induced Forces** Vortex-induced forces are generated due to the shedding of vortices due to flow separation over the structure. These vortices induce oscillating forces in line with the flow and transverse to the flow. The generated oscillating pressure field can induce large oscillations on the structure if the vortices are shed symmetrically (typically around a bluff cylinder) and at a constant frequency close to the natural frequency of the structure. This could cause problems for catenaries or mooring lines of TLPs.

2.3.2. Potential Flow Theory

In potential flow theory, the flow is assumed to be irrotational, inviscid, and incompressible. Applying these limits to the Navier-Stokes equations will provide an equation called the Laplace equation, denoted in Equation 2.3 (Lin, 2008).

$$\nabla \cdot u = \nabla(-\nabla\phi) = -\nabla^2\phi = 0 \tag{2.3}$$

The potential flow method can be used when the expected effect of viscous forces is small and when the characteristic length of the body (D) is large compared to the wavelength (L). The FK force can be obtained by integrating the pressure distribution around the body.

Numerical solvers such as WAMIT use linear and second-order potential flow theory to analyze floating bodies. The panel method is used to solve the fluid pressure around the submerged body, while diffraction and radiation problems are solved separately (C. Lee, 1995). The resulting hydrodynamic parameters can be used in time domain analyses such as OpenFast or OrcaFlex.

2.3.3. The Morison Equation

The Morison equation is an empirical relation that describes the inline force due to an oscillatory flow. The equation consists of two distinct parts, the inertial force and the drag force.

$$F(t) = \rho C_m V \dot{u} + \frac{1}{2}\rho C_d A u|u| \tag{2.4}$$

Where ρ is the density of the fluid, V is the volume of the body, u is the undisturbed velocity, and C_d is the drag coefficient, which is a function of Reynolds number, skin roughness, and body shape. The Morison equation can be used when the influence of drag forces is significant and the characteristic length of the body (D) is small compared to the wavelength (L)

Often, potential flow methods are combined with Morison methods. For instance, floating structures that consist of slender parts can be modeled using Morison's equation, while the other parts are modeled using potential flow methods. Another way of combining these methods is using potential flow methods

for the calculation of the wave forces and adding the Morison Drag equation to account for viscous effects (Otter et al., 2022).

2.3.4. Cummins' Equation

A different time domain approach is proposed by Cummins (Cummins, 1962). This approach uses a convolution integral approach to describe the time history of the fluid memory effects. The frequency-independent coefficients make this approach suitable for transient processes. The retardation functions in this approach are linked to the velocity potential function. T.F. Ogilvie found a way to calculate these retardation function from the hydrodynamic parameters, such that they could be calculated from the frequency domain (Ogilvie, 1964). However, the convolution functions make this a cumbersome and computationally expensive option. Cummins' equation is presented in Equation 2.5.

$$[\mathbf{M} + \mathbf{M_a}]\,\ddot{\mathbf{x}}(t) + \int_0^t \mathbf{K}(t-\tau)\dot{\mathbf{x}}(\tau)\mathrm{d}\tau + \mathbf{C}\mathbf{x}(t) = \mathbf{f}^{\mathrm{exc}}(t) \tag{2.5}$$

Where $\mathbf{M}$ is the mass matrix, $\mathbf{M_a}$ is the added mass matrix, $\mathbf{K}(\mathbf{t})$ is the retardation function matrix, $\mathbf{C}$ is the restoring matrix, $\mathbf{f}^{\mathrm{exc}}(t)$ is the wave force. $\mathbf{x}(t), \dot{\mathbf{x}}(t)$ and $\ddot{\mathbf{x}}(t)$ are the displacement, velocity and acceleration vectors respectively.

Since then, studies have focused on avoiding these convolution terms by replacing the frequency-dependent hydrodynamic parameters with constant coefficients or by replacing the retardation functions with state-space models (T. Duarte et al., 2013; Taghipour et al., 2008).

In literature, a number of different methods have been used to model the radiation force time history. Frequency response functions of the floating structure are obtained from standard codes such as WAMIT, which are based on linear theory. For non-linear effects such as viscous effects, this linearity assumption breaks down. One way to overcome this is to apply higher-order frequency-domain approaches based on Volterra series. The problem with these frequency techniques lies in the fact that they only apply to steady-state processes, while transients are also of interest. Furthermore, higher order techniques are difficult to implement and computationally expensive (Taghipour et al., 2008).

F. Liu et al., 2017 propose a different method to solve the frequency domain equation, by representing the frequency domain convolution terms in the Laplace domain. This new representation aims to find a replacement for the retardation functions based on the estimated frequency-dependent damping matrix.

Lu et al., 2022 propose a state-space model approach. They estimate the rational part of the transfer function by using a quasi-linear regression method and use this to build the state-space model. The inputs to this system are the wave forces on the floating structure, while the outputs are the displacements of the floating structure.

The retardation effects of the radiation force can be calculated directly in the time domain by fitting a state-space model. This requires the system identification of the state-space model. T. Duarte et al., 2013 describes the time domain identification process used within FAST to determine the state-space matrices. This state-space method allows for comparable results while providing a computationally more efficient method.

2.3.5. Higher Order Hydrodynamics

Second-order hydrodynamic forces can be separated into three components: mean drift loads, difference-frequency loads, and sum-frequency loads. These second-order components are generally an order of magnitude lower in amplitude than the first-order loads. However, floaters and offshore systems are often designed such that the first-order loads do not act at the resonant frequency of the structure, but for the second-order forces this is not necessarily the case.

Mean drift loads are generated due to an interaction between first-order motion and the first-order wave field, resulting in a mean offset of the body to its undisplaced position. Difference- and sum-frequency loads are generated due to the same phenomenon, but they differ in the frequency of the force; difference-frequency loads have a frequency that is lower than the first-order wave excitation forces, while the sum-frequency loads have a frequency that is higher than the first-order wave excitation forces. difference-frequency loads (also known as slow varying drift forces) are generated as

a result of the interaction between waves of different frequencies. These (generally small amplitude) forces can generate large displacements in catenary-moored floating wind turbines if the frequency coincides with the resonant frequency of the structure.

sum-frequency forces are generated in a similar fashion; the contribution of these forces is often important in cases where ”ringing” or ”springing” effects are prone to occur, which for FOWT is often the case in configurations with taut mooring lines such as TLP concepts (Matha et al., 2011).

Bayati et al., 2014 have investigated the effect of second-order excitation effects on a floating semi-submersible FOWT. WAMIT was used to solve the first and second-order hydrodynamics problems in the frequency domain. Applied to the OC4-DeepCwind semi-submersible and NREL 5 MW reference turbine. (at the time of writing their paper) Fast was not configured to utilize the second-order quadratic transfer function (QTF) calculated by WAMIT. Assessment of the paper was conducted within WAMIT only.

The results show a comparison between the Response Amplitude Operator (RAO) to the first-order forces and the second-order forces. The comparison shows that in surge, the second-order *forces* are significantly smaller in magnitude than the first-order effects; however, the surge *motion* is largely dominated by second-order difference response.

In pitch, the second-order forces are also significantly smaller than first-order, just like in surge. However, the motion response is not dominated by second-order effects like in surge. The motion response does show a peak at the lower frequency second-order forces; however, this motion amplitude is significantly smaller than at the first-order peak. (order of 10 smaller)

The heave responses tell a similar story to pitch. However, the motion response of the second-order effects is, while still smaller, not nearly as small as in the pitch response. (order of 3 smaller)

The paper concludes that, even though WAMIT likely overestimates the response of the system due to a lack of viscous drag, ”the frequency content of second-order difference-frequency loads cannot be neglected in the dynamic analysis of such a system”.

Karimirad, 2013 has carried out a dynamic response analysis of FOWT with a spar-buoy type floater, using a combination of Simo-Riflex, HAWC2, and FAST. In this study, the effects of higher-order hydrodynamics are investigated by comparing different hydrodynamic approaches within Simo-Riflex. The comparison shows that the mean drift forces, while small, excite the resonant frequency of the heave motion, resulting in large motion amplitudes. However, little difference is seen in the other motion responses. Regarding the second-order sum and difference forces, a similar relation is found; second-order forces are significantly smaller than the first-order forces. The motion response, however, is significantly influenced in the heave direction.

The inclusion of second-order forces is often dependent on the type of system that is being researched. As mentioned, the ”springing” and ”ringing” effects in systems with taut mooring lines are caused by the second-order sum-frequency effect. Difference-frequency and mean drift forces lead to large motion in surge for floaters with catenary-type mooring line systems. Thus, a study of a TLP concept would be suitable for including the second-order sum-frequency force, while in floater types with catenary mooring line systems, it would be better to include the second-order difference-frequency force and mean drift force.

2.3.6. CFD Modeling

One distinction between CFD and potential flow modeling is the ability of CFD to compute the viscous damping at the natural frequency. This is calculated using free decay tests and is of importance due to the reliance of potential flow methods on externally calculated viscous (damping) forces (Zhang et al., 2024). Besides viscous effects, CFD also offers the ability to take into account other non-linearities such as turbulence effects and wave-breaking.

In potential flow solvers, viscous damping is introduced as an external forcing term, as they are inherently incapable of reproducing this effect. CFD generally solves the flow by solving the continuity and Navier-Stokes equation for incompressible viscous flow. Turbulence in the flow is added using one of a few different types of turbulence models. Y. Liu et al., 2017 uses a two-equation $k - \omega$ shear stress

transport (SST) turbulence model, for instance. For wave generation, a wave generation module is included, which allows the modeling of various wave types. Additionally, a quasi-static mooring line model is used. At the start of a time step, the fairlead tension components are estimated using the last time step values, and then an iterative approach is employed to calculate the current values.

Difficulties arise in the mesh deformation due to the large body motions of the system, inherent to fully coupled FOWTs. When modeling the hydrodynamics of the floater, a cylindrical sliding mesh can be used such that the rotation of the inner cylindrical mesh represents the pitching motion of the floater.

PF underestimates the added mass at low frequencies by over 10% (Li & Bachynski-Polić, 2021). QTF determined from CFD shows that at the surge natural frequency, the magnitudes are similar, at higher frequency (around the pitch natural frequency), the CFD QTF shows a larger magnitude. Furthermore, they find that all numerical models (CFD & SIMA) underestimate the damping present compared to the experimental data, though the CFD model does perform significantly better than the PF solvers.

The authors conclude that CFD simulations can provide a more accurate estimation of the non-linear hydrodynamics. This would reduce under underprediction of low-frequency dynamic response that is present in potential flow solutions and show better agreement with experiments. CFD could then be of interest in the generation of the hydrodynamic parameters used in the real-time simulation.

2.3.7. Sea States

Hydrodynamic forcing on the floater is caused by incident waves on the floating structure. Waves can be modeled numerically as either regular waves or irregular waves. Regular waves are the simplest waveforms, consisting of a pure sinusoidal wave with constant amplitude (a), frequency (ω), and phase angle (ϕ).

$$\eta(t) = asin(\omega t + \phi) \tag{2.6}$$

Typically, irregular waveforms are represented by a spectral model. In such a model, the wave elevation of the irregular wave is approximated by a linear superposition of regular sinusoidal waves, as presented in Equation 2.7

$$\eta(t) = \sum_{i=1}^{n} a_i sin(\omega t + \phi_i) \tag{2.7}$$

Common formulations used to model irregular sea states are the Pierson-Mokowitz (PM) spectrum and the JONSWAP spectrum. The PM spectrum assumes a fully developed sea state, that is, wave-wave interaction is neglected, and it is assumed that the wave state remains constant over time (Moskowitz, 1964). The PM spectrum is modeled using Equation 2.8

$$S(f) = \alpha g^2 (2\pi)^{-4} f^{-5} exp\left(-\frac{5}{4}\left(\frac{f_m}{f}\right)^4\right) \tag{2.8}$$

Where α is the Philips constant and f_m is the peak frequency.

During the Joint North Sea Wave Observation Project (JONSWAP) Hasselmann et al., 1973 found that in reality, the wave state is never fully developed. The JONSWAP spectrum adds an extra factor to the PM spectrum to account for the ever-developing sea state. This extra factor is called the peak enhancement factor.

$$S(f) = \alpha g^2 (2\pi)^{-4} f^{-5} exp\left(-\frac{5}{4}\left(\frac{f_m}{f}\right)^4\right)\gamma^r \tag{2.9}$$

$$r = exp\left(-\frac{(f - f_p)^2}{2\sigma^2 f_p^2}\right) \tag{2.10}$$

Where γ^r is the peak enhancement factor. For a peak enhancement factor of 1, the JONSWAP spectrum is equal to the PM spectrum, and thus a fully developed sea state.

Another aspect of sea states is directionality or directional spreading. In many cases, sea states are modeled using unidirectional wave fields. However, the different waves that form an irregular wave field all have different headings (T. Duarte et al., 2014). Multidirectional wave states are often modeled using spreading functions (T. Duarte et al., 2014; Young, 2017).

Engineering tools such as OpenFast offer wave loading with both PM and JONSWAP spectra as well as multidirectional wave states. Generally, using the JONSWAP spectra is preferred due to the more realistic approach to the development of sea states.

Sharma and Dean, 1981 found that the use of a multidirectional wave state will reduce the total wave loading on the floater; that is, a multidirectional randomly generated wave state, summed over all piling of the structure, generates less total force than a unidirectional train of waves with the same one-dimensional spectrum. For single pilings, it was found that the total force on the structure reduces to a factor of 0.61 for a uniformly distributed wave over the half-plane.

Additionally, it is noted that the use of directional effects can and should be used in the design of floating structures. The use of unidirectional wave states overstates the wave forcing on the offshore structure to provide a less realistic picture, requiring an over-engineered design, thus costing the manufacturer.

The directionality of the sea state can also cause wind-wave misalignment. Philippe et al., 2013 shows that this non-linear effect can excite motion in different modes if the waves and wind are misaligned. The study shows the RAO of a spar-buoy type floating wind turbine for different wave directions. The misalignment causes spectral peaks in sway, roll, and yaw.

Bachynski et al., 2014 have studied the effect of wind-wave misalignment for different floater types. They have found that the wind-wave misalignment causes increased motion in the system. Of all considered floater types, the TLP has the lowest standard deviation in the considered degrees of freedom. The spar-type and semi-submersible-type floaters show larger standard deviations for increasing misalignment in the sway, roll, and yaw motion.

Besides the effect on motion, the authors note that the highest loading on the structure in terms of tower base stress is caused by the aligned cases. Further studies by Barj et al., 2014 also note that the highest loading on the tower occurs in aligned wind-wave cases, except for tower-base side-to-side bending mode, which is greatly affected by the misalignment. Fatigue analyses show similar results.

2.3.8. Mooring Lines

As mentioned before, different floating systems configurations use different mooring line systems. Semi-submersible type floaters typically use catenary mooring line systems, while TLP type floaters use taut mooring line systems. Spar-buoy type floaters can use either depending on the design. TLP floaters (and some spar-buoy types) rely on the mooring system for the stability of the floating system, while other types rely on stability provided by the floating platform itself. Advantages of taut mooring lines include reduced platform motion and shorter mooring cables. Though the cables do need to carry much larger loads due to the required pre-tension.

Mooring Line Models

In numerical simulation, there are several ways to model the effects of a mooring line system on the dynamics of a floating body, they can be divided into three categories: a linear, quasi-static, or dynamic approach. The difference between these types of models lies in the fidelity and computational cost of the modeling approach, where increasing fidelity becomes more computationally expensive.

Linear Approach

Linear mooring line models (also known as linear force-displacement-velocity models) are the simplest type of mooring line model. The mooring line is represented as a simple mass-damper-spring system where the Damping and stiffness matrix represent the total stiffness and damping capabilities of the system, and no information about individual lines is available (Borg et al., 2014). This simple approach is often used in the early design process, when little information regarding the setup is known and doesn't provide a particularly accurate mooring line model.

Quasi-Static Approach
In a Quasi-Static (QS) approach, at each time step, the catenary equation is solved as if the solution has reached a steady state value. This method rests on two assumptions: That inertia effects are negligible compared to drag, and that the line can at any time be approximated as a quasi-static catenary (Bauduin & Naciri, 2000).

This approach is a mid-fidelity method that is mostly used in cases where the goal of the simulation is connected to global system dynamics of the floating structure, and not necessarily the mooring system itself. In cases where the loads on the mooring lines are of interest, the transient response of the mooring lines and the vibrations carried by the cables are not reproducible by such a quasi-static model (Bauduin & Naciri, 2000).

Dynamic Approach
Whereas QS approaches calculate a steady state at each time step, dynamic models also capture transient effects. Dynamic mooring line models differ in the following way: the formulation accounts for inertia, internal damping, and viscous & drag effects. Additionally, it allows for the propagation of transverse and longitudinal effects (vibrations), which allows the model to capture vortex-induced vibrations (VIV). Furthermore, a dynamic approach provides the ability to measure ultimate and fatigue loads in mooring lines.

Within dynamic models, three groups of models can be distinguished; Finite Element Method (FEM) models, Finite Difference (FD) models, and Lumped mass (LM) models (Masciola et al., 2014). The governing formulation of the mooring line is a partial differential equation (PDE); the type of dynamic model follows from the method of solving the PDE. Two methods of solving the PDE are discussed in (Masciola et al., 2014):

Galerkins method can be used to eliminate spatial derivatives and transform the equation into a ODE, which leads to a FEM model. This FEM model has a mass matrix with off-diagonal terms, if these off-diagonal terms are eliminated, the model becomes a LM model. The second approach is a Taylor series expansion of differential terms to obtain derivatives around an operating point, which leads to an FD approach. According to (Masciola et al., 2014), the LM and FEA models are inherently less prone to numerical errors due to the conservation of energy flux.

Hall and Goupee, 2015 found that for platforms with small responses, the fidelity of the mooring line model does not significantly impact the motion response of the structure. However, for the mooring line forces themselves, it is important.

Zhong et al., 2024 have done a comparison between three dynamic and three quasi-static mooring line models. They present similar results, in a CFD analysis coupled to an FEM mooring line analysis and 3 quasi-static models. The difference in total axial loading of the mooring lines differs quite substantially between the FEM and quasi-static models, but the total motion of the floater remains quite similar. Additionally, they note that between the dynamic models, the FEM and LM models are better suited to be used in a coupled numerical approach than the FD model due to computational costs.

2.3.9. Hydrodynamic Formulations Used in HIL Experiments
Previous HIL experiments done by the Politecnico di Milano have used Cummins' equation to solve the dynamics of the floater, both in 2-DOF (Ambrosini et al., 2020) and 6-DOF (Bayati et al., 2018).

The required hydrodynamic parameters were obtained from the potential flow solver WAMIT, which also accounts for the radiation and wave excitation forces. The study also takes into account viscous forces, based on Morison drag forces, and Mooring line forces in a dynamic lumped mass method based on the formulation used in the MoorDyn module of FAST/OpenFast (Bayati et al., 2018).

Ambrosini et al., 2020 have also included the second-order diffraction forces. Specifically, the second-order difference-frequency contribution is accounted for, while the sum-frequency is omitted. The sum-frequency contribution is negligible compared to the first-order and cannot excite the system. The mooring line system in their study is modeled using a look-up table; the corresponding forces due to displacement in the respective degrees of freedom were obtained from numerical analyses using FAST.

Fontanella, Facchinetti, et al., 2023 also note the importance of including the second-order difference-frequency component. They also used a slightly different approach to the viscous forces. Instead of including Morison drag forces, a quadratic and linear damping term is added to the 6 DOF equation of motion. These damping terms were identified using a wave-basin experiment. The mooring lines are modeled using a linear approach to save computational effort.

Recently, TU Delft has created a HIL setup for wind tunnel testing. The setup consists of a 1:148 scale model of the DTU 10 MW reference turbine (Bak et al., 2013). Taruffi et al., 2024 presents the effect of prescribed motions on the loading of the rotor.

Thinakaran, 2024 presents the HIL setup with complete coupling between the (physical) aerodynamics and (numerically simulated) floater dynamics. The floater design is the TripleSpar floater (Lemmer et al., 2020). The study obtains the hydrodynamic parameters of the floater from WAMIT. The hydrodynamic radiation force is modeled using a state-space approach, similar to the one used in OpenFast and WAMIT. Only first-order hydrodynamic forces were considered. The mooring line system is modeled using a linear approach that is presented in the definition of the floater; a 6x6 stiffness matrix is found. Viscous damping is modeled using a linear diagonal damping matrix and a contribution from the drag part of the Morison equation using an estimated drag coefficient of 0.61.

The experiments consisted of a number of steps. The first step was to test the static case, to make sure that the wind turbine design itself is performing as it is supposed to, regardless of the HIL setup. The second step was to perform a comparison between an open-loop test and a closed-loop test. This comparison is required to determine whether or not the HIL setup is performing adequately. These tests are done using decay tests to allow for easy comparison using the frequency and damping values in all degrees of freedom.

The final step consists of the simulation of irregular wave states. The JONSWAP spectrum was used for wave generation, with a gamma value of 3.3. The experiments only considered unidirectional sea states and no wind-wave misalignment.

2.4. Concluding remarks

Based on the research presented in the previous chapters, it can be established that the hydrodynamics and floater modeling of the TU Delft HIL setup uses fairly simplified formulations. Other HIL experimental setups from Politecnico di Milano have used higher fidelity modeling techniques for the representation of the mooring line system, and included the contribution of higher-order hydrodynamic forces.

It is known that the use of higher fidelity modeling techniques for the mooring line system will provide a more realistic response of the floater, but previous HIL experiments have not compared the use of the different mooring line formulations to assess the effect on overall system dynamics. Additionally, these different modeling approaches offer insight into mooring line ultimate and fatigue loads that are not available in stiffness matrices or lookup tables.

Additionally, the sea states considered did not include multidirectional effects. The unidirectional sea state does provide the highest loading on the system but also overestimates the loading encountered in a realistic setting. For FOWT, it is ever more important to design according to actual conditions that will be encountered; overstating the encountered forces will lead to costly, over-engineered designs that could economically hurt the floating system.

Hardware-in-the-loop wind tunnel testing provides a good testing environment for the analysis of aerodynamic effects on floater dynamics. The effect of aerodynamic thrust and torque can be accurately simulated on scaled wind turbine designs, such that the effects of wind-wave interaction and aerodynamic damping can be quantified.

To improve the fidelity of the TUDelft HIL simulation of a FOWT and research the effect of more complex metocean conditions on the dynamics of the system.

This goal will be met by incorporating the effects of second-order hydrodynamics. Additionally, a comparison will be made using different formulations for the mooring line system. The effects of aerodynamic damping will be investigated in the wind tunnel with a combination of wind-wave cases and

decay tests in multiple degrees of freedom for a range of operating wind velocities. Finally, the following research questions will be answered:

Research Questions

1. To what extent do the higher-order wave forces affect the dynamic behaviour of the FOWT system in a hybrid testing environment?
2. Does the inclusion of a quasi-static or dynamic mooring line system significantly affect the FOWT system dynamics? Does the increase in fidelity justify the increase in computational cost?
3. What is the effect of aerodynamic forces on the damping and natural frequency of a floating offshore wind turbine?

3

Methodology

This chapter will present the methodology that the work is based on. Firstly, section 3.1 will present the wind turbine and floater model that will be considered in this study. Additionally, it will introduce the verification tool used later on to verify the results. The experimental setup of the HIL experimental wind tunnel tests and the required hardware will be presented in section 3.2. The theoretical basis of this study will be discussed in section 3.3. A method is presented to calculate the pre-determined first- and second-order wave forces acting on the floating platform. Additionally, the mathematical representations for the quasi-static and dynamic mooring line model will be discussed. Finally, section 3.4 will cover how these mathematical models are implemented into the Simulink model. Furthermore, the architecture of the Simulink model is presented, discussing the subsystems it contains.

3.1. Wind Turbine and Floater Characteristics

The wind turbine model considered in this study is the DTU10MW wind turbine, a design used primarily as a publicly available reference turbine for research purposes (Bak et al., 2013). As part of the LIFES50+ research project, publicly available FAST v8 (precursor to OpenFast) models have been created according to this reference turbine. As the name suggests, the reference turbine is designed for a rated power production of 10 MW, at a rated wind speed of 11.4 m/s. A summary of the most important characteristics can be found in Table 3.1

Table 3.1: Summary of characteristics of the DTU10MW wind turbine.

Parameter	Value
Rating	10 MW
Control	Variable speed, collective pitch
Rotor Diameter	178.3 m
Hub height	119 m
Cut-in, Rated, Cut-out wind speed	4 m/s, 11.4 m/s, 25 m/s
Cut-in, Rater rotor speed	6 RPM, 9.6 RPM
Rotor Mass	229 tons
Nacelle Mass	446 tons
Tower Mass	605 tons

The floater considered is the SWE-TripleSpar Floating platform (Lemmer et al., 2020), specifically designed for use with the DTU10MW wind turbine as part of the LIFES50+ project. The semisubmersible floater consists of three concrete cylinders, connected by a steel tripod. A verification study of the structural mechanics of the Triple Spar floater was done by Manolas et al., 2018. The structural characteristics of the TripleSpar are summarized in Table 3.2. The mooring system consists of three catenary (slack) mooring lines, consisting of steel chain at the bottom, and polyester at the upper part of the mooring line.

Table 3.2: Summary of characteristics of the TripleSpar Floater.

Part	Parameter	Value
Platform	Elevation above SWL	25 m
	CoM below SWL	35.97 m
	Platform total mass	28268 tons
Columns	Length	65 m
	Distance to centre	26 m
	Diameter	15 m
	Elevation above SWL	10.5 m
	mass (per column)	3279.5 tons
Heave Plates	Thickness	0.5 m
	Diameter	22.5 m
	Mass	1639.3 tons
Tripod	Total Height	15 m
	Mass	948.36 tons

OpenFast
The implementation of both wave forcing and mooring models will be verified using OpenFast v3.5.4 as a benchmark (Jonkman et al., 2024). OpenFast (previously known as FAST v8) is an open-source, mid-fidelity engineering tool widely used in industry for the modeling of (floating) wind turbines. It consists of an overarching structure, which couples modules for aerodynamic, hydrodynamic, control, and elastic structural dynamics, for the simulation of non-linear aero-hydro-servo-elastic dynamics in the time domain. The definition of the TripleSpar floater includes a repository with OpenFast input files, using the DTU10MW wind turbine. Though the input files had to be updated to a newer version of OpenFast, this allows for verification of the developed numerical simulation in this study. The mathematical representations of the mooring models will be adapted from the Mooring Analysis Programme (MAP++) and MoorDyn, which are submodules that can be used within OpenFast to model quasi-static and dynamic mooring lines, respectively.

3.2. Experimental Setup

This section aims to provide an overview of the experimental setup used in the HIL wind tunnel tests. The setup will be discussed in terms of subsystems and components, as well as the wind tunnel and logistics of the setup. A visual overview of the system and its components can be found in Figure 3.1.

3.2.1. Open Jet Facility

The experimental setup will be tested in the Open Jet Facility (OJF) to generate the aerodynamic loads on the wind turbine model. The OJF is a low-speed wind tunnel that has a maximum wind speed of 35 m/s. The OJF is used for the testing of scaled-wind turbine models because of the low required wind speed at model scale, and a large octagonal nozzle of 2.85 x 2.85 m that reduces the influence of wall effects (“The Open Jet Facility”, 2025). The wind tunnel is powered by a 500 kW motor in a horizontal loop wind tunnel design, achieving a turbulence level of 0.5% at a distance of 1 m, and a turbulence level of less than 2% at 6 m. The Wind turbine model will be located 3.1 meters away from the nozzle opening for safety. If it were any closer, then the rotor would be in front of a door. Even though this door would be closed at all times during operation, this could be potentially hazardous if there are any issues with the rotating equipment, especially at the high rotational speeds that are required at model scale. Additionally, the Hexapod will be positioned on top of a pneumatic table, allowing the rotor hub to be positioned in the middle of the nozzle, with the help of a laser level.

3.2.2. Wind turbine model

The wind turbine model used in this study is a 1:148 scale model of the DTU10MW reference turbine (Bak et al., 2013), paired with a velocity scaling of 1:3. The scaling factors can be seen in Table 3.3. The aerodynamic design was not performed in this study, rather the same model was used from earlier studies (Thinakaran, 2024) and (Taruffi et al., 2024). The aerodynamic design of the rotor was done in an earlier study by Politecnico di Milano (Fontanella, Da Pra, & Belloli, 2023). This design does not

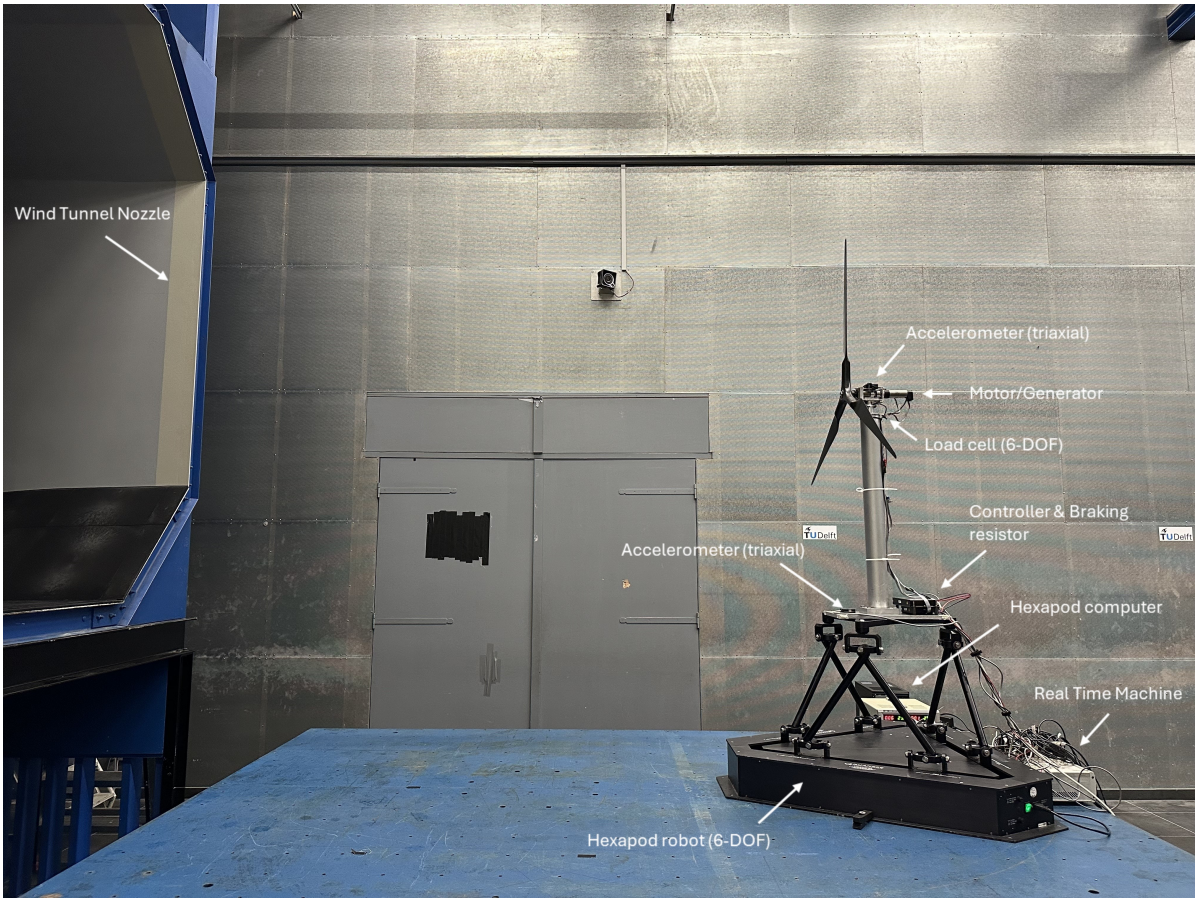

Figure 3.1: Overview of the wind turbine model and Hexapod in the wind tunnel test section.

follow the geometrical scaling of the original aerodynamic design of the DTU10MW wind turbine; the design philosophy instead aims to match the thrust generated by the rotor, since the thrust force plays a large role in the overall system dynamics of a floating wind turbine. The Rotor Nacelle Assembly (RNA) is mounted on top of a cylindrical, aluminium tower, with a first fore-aft bending mode at 12.5 Hz. This is substantially higher than the 1p and 3p frequency, such that it is not excited during testing.

3.2.3. Sensing and Actuation

2 triaxial MEMS accelerometers are applied to the wind turbine model, one at the top of the nacelle and one at the bottom plate in front of the tower. In the numerical simulation, only the output from the accelerometer at the tower top is used; the second one at the tower bottom can still be used to verify the motion tracking of the Hexapod.

The load cell is located in between the RNA and the tower top. From this load cell, aerodynamic forces can be measured along with gravitational and inertial forces of the RNA above it. The motor (model:Maxon EC-4pole 30 200W) that drives the rotor is capable of working as a motor or as a generator. It is connected to the rotor shaft by a gearbox (model: Maxon GP32 C5.8:1) and an Oldham coupling. For startup of the rotor, the motor is used to get the rotor up to the required rpm (480 at rated wind speed), then in power production mode, the motor will work as a generator and generate power. To this end, the generator is connected to a braking resistor (model:Maxon DRS70/30) to dissipate energy. A motor controller (model: Maxon Escon70/10) is required to set different operating conditions of the rotor, the motor encoder (model: Maxon HEDL 5540) measures actual speed and current, which allows for determining rotor torque. However, the torque measured at the motor is generally lower than the actual rotor torque, due to mechanical losses in the gearbox and electrical losses in the generator. Thus, it is preferable to measure the rotor torque using the load cell.

The actuation of the floater dynamic motion is done by a 6-DOF parallel kinematics robot produced by

Table 3.3: Scaling factors of the model scale DTU10MW wind turbine.

Parameter		Value
Length	λ_l	$1/148$
Velocity	λ_v	$1/3$
Mass	$\lambda_m = \lambda_l^3$	$1/148^3$
Time	$\lambda_t = \lambda_l/\lambda_v$	$3/148$
Frequency	$\lambda_f = 1/\lambda_t$	$148/3$
Acceleration	$\lambda_a = \lambda_v/\lambda_t$	$148/3^2$
Force	$\lambda_F = \lambda_m\lambda_a$	$1/(3^2 \times 148^2)$
Torque	$\lambda_T = \lambda_F\lambda_l$	$1/(3^2 \times 148^3)$
Reynolds Number	$\lambda_v\lambda_l$	$1/444$
Froude Number	$\lambda_v/\sqrt{\lambda_l}$	$\sqrt{148}/3$

Quanser, referred to as 'Hexapod' hereafter. The Hexapod has the ability to actuate payloads of up to 100kg. The workspace of the Hexapod is defined as the allowed distance in translational and rotational DOFs that the platform can move. If all other DOFs are kept in home position, the Hexapod is able to actuate ± 7.4 cm in surge, ± 11 cm in sway, ± 5 cm in heave. For rotational degrees of freedom, it allows for approximately ± 15 degrees in roll and pitch and ± 25 degrees in yaw.

The Hexapod has its own designated computer to handle the computation of the inverse kinematics based on the desired position and inclination of the floater, as calculated in the numerical simulation. It then outputs its commanded position as well as the actual position to the data acquisition system. These data points can then be compared to make sure that the Hexapod is able to follow the commanded position. The Hexapod also comes with its own scripts and Simulink models for calibration, homing to its 0-position and operation using sinusoidal prescribed motion, though the latter will not be used in this study.

3.2.4. Real-time Simulation Machine

The Simulink model of the floater dynamics will be run on a dedicated real-time machine, the DSpace MicroLabBox 1302. This real-time machine manages the signals from the accelerometers, load cell, hexapod, motor, and control systems. Additionally, this device runs the numerical simulation that solves the floater dynamics and outputs the signals to the Hexapod. The DSpace takes all analog signals at a sampling frequency of 1000 Hz. At the same time, all logged signals are sent to a Human-Machine interface in real-time, such that the signals can be visualized during the tests, and commands can be sent to the numerical simulation. The human-machine interface is set up in the control room of the OJF, such that the system can be safely commanded during operation of the wind turbine. During a simulation, commands can be sent for the application of wave forces or external forces on the system. Additionally, the controller of the motor can be commanded from the human-machine interface to be able to control the rotor speed.

To run a Simulink model on the DSpace, the Simulink model has to be "built and deployed". The simulation of different mooring models cannot be commanded during a simulation; instead, when a Simulink model is built, the preferred model has to be chosen beforehand. Similarly, for wave cases, when the model is built, the time history of the pre-generated wave case is loaded into the model. If a simulation has to be run with a different mooring model or wave case, this process has to be redone.

3.3. Theoretical basis

The mathematical representations the work is based on have been briefly discussed in the literature study; a more elaborate overview will be given here. First, a quick overview of the floater dynamics and the local reference system of the numerical simulation will be given. subsection 3.3.2 will present the methodology of generating the time history of wave forces, from the JONSWAP spectrum, for both first- and second-order wave excitation forces. The mathematical representation of the quasi-static and dynamic (lumped-mass) mooring model is discussed in subsection 3.3.3.

3.3.1. Floater Dynamics

The basis of HIL simulation lies in the numerical simulation of the dynamics of the floating platform. To this end, a Simulink model solves the Equation of Motion (EoM) that describes the dynamics of this system. In essence, this EoM will take the form of Equation 3.1.

$$[\mathbf{M} + \mathbf{A}]\,\ddot{\mathbf{x}} + \mathbf{D}^{(1)}\dot{\mathbf{x}} + \mathbf{D}^{(2)}\dot{\mathbf{x}}^2 + \mathbf{K}\mathbf{x} = \mathbf{F}_{ext}(\dot{\mathbf{x}}, \mathbf{x}) \tag{3.1}$$

Where $\mathbf{M}$ is the mass matrix, $\mathbf{A}$ is the added mass matrix, $\mathbf{D}^{(1)}$ and $\mathbf{D}^{(2)}$ are the damping and quadratic damping matrix respectively, and $\mathbf{K}$ is the stiffness matrix. The state vector $\mathbf{x}$ contains the current position of the floater, $\dot{\mathbf{x}}$ and $\ddot{\mathbf{x}}$ indicate the velocity and acceleration vector, respectively. The state vector contains 6 DOFs, consisting of the three translational DOFs Surge (x), Sway (y) and Heave (z), as well as the three rotational DOFs, Roll (ϕ), Pitch (θ) and Yaw (ψ). Figure 3.2 shows the coordinate system used in this study.

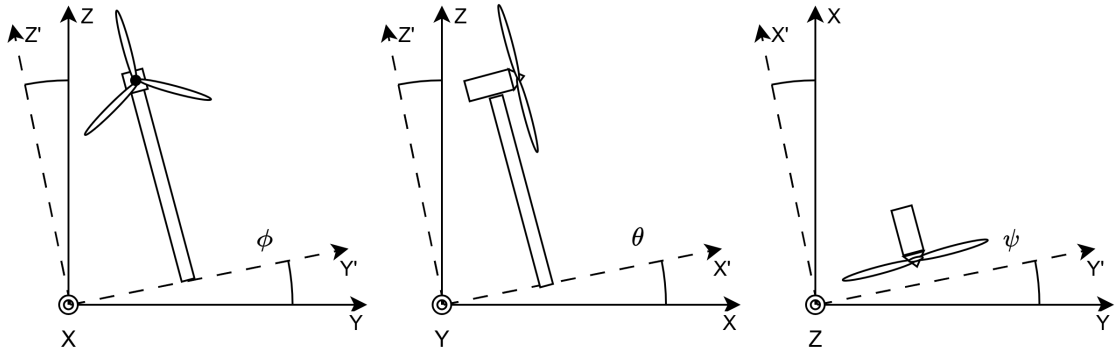

Figure 3.2: Schematic of the rotations used in the current study.

$\mathbf{F}_{ext}$ are the external forces acting on the floater. The contributions taken into account in this study can be found summarized below.

1. $\mathbf{A}(\ddot{\mathbf{x}})$ Added Mass
2. $\mathbf{F}_{aero}$ Aerodynamic forces
3. $\mathbf{F}_{rad}$ Radiation
4. $\mathbf{F}_{diff}$ Diffraction
5. $\mathbf{F}_{moor}$ Mooring Forces

The mass, damping, stiffness, and added mass matrices are obtained from the definition of the TripleSpar floater and from the definition of the DTU 10 MW wind turbine (Lemmer et al., 2020), (Bak et al., 2013). These matrices thus define the properties of the system. Viscous forces are not applied specifically; instead, their effect is accounted for by an additional damping matrix. The aerodynamic force is applied physically in the wind tunnel, by rotor operation. However, the measured forces by the load cell will have to be corrected in the numerical simulation. The remaining external forces in radiation, diffraction, and mooring forces are numerically simulated. The radiation forces will be modelled in the form of a state-space system, as used in the previous study by (Thinakaran, 2024). The diffraction and mooring forces are the main point of interest in this study, and their implementation will be explained in more depth in the next section.

3.3.2. Sea State & Waves

Ocean wave measurements of wave elevation can generally be modeled as a stationary stochastic process with a narrow-banded spectral density. Furthermore, in the analysis of ocean waves, it is common to represent the surface elevation as a linear superposition of linear (airy) waves (Young, 2017). The mathematical representation of the first-order solution of this superposition is shown in

Equation 3.2. This equation is based on the assumptions that the ocean waves can be considered an incompressible, inviscid, and irrotational fluid. (Jensen, 2001).

Additionally, each sinusoidal wave considered here is a linearly independent sample from a stochastic process, where the solution is found to a homogeneous linear differential equation with homogeneous boundary conditions.

$$h^{(1)}(X,t) = \sum_{i=1}^{n} a_i sin(k_i X - \omega_i t + \theta_i) \tag{3.2}$$

This equation is a function of space and time. For single body analysis, it is common to simplify the equation to only vary over time, which would reduce to Equation 3.3:

$$h^{(1)}(t) = \sum_{i=1}^{n} a_i sin(\omega_i t + \theta_i) \tag{3.3}$$

Where a_i, ω_i, and θ_i are the amplitude, angular frequency, and random phase angle of the i-th wave component. The amplitude of the individual wave components can be found with the relation shown in Equation 3.4. The phase angle θ represents a random sample of the stochastic process h in t. The amplitudes a_i can be calculated based on the wave spectrum according to Equation 3.4.

$$a_i = \sqrt{2S(\omega_i)\Delta\omega} \tag{3.4}$$

Where $\Delta\omega$ is the spacing in the angular frequency discretization. These amplitudes are then the connection between the frequency domain wave spectrum and the time domain wave elevation.

Wave Spectra

There are a variety of frequency domain spectra that could be used to represent the energy distribution of a sea state. In engineering applications, the most commonly used are the Pierson-Moskowitz spectrum or JONSWAP spectrum, as discussed earlier in subsection 2.3.7. In this study the JONSWAP spectrum was used to model the sea state to account for a developing sea state.

This study makes use of the Wave Analysis for Fatigue and Oceanography (WAFO) MATLAB Toolbox to determine the frequency spectra according to the JONSWAP spectrum (Brodtkorb et al., 2000). The Toolbox offers functions to directly compute a JONSWAP spectrum based on an input of significant wave height (known as H_s or H_{m0}, this study will continue with H_s), peak period (T_p), and desired wave time history duration. The duration has to be given beforehand, since it determines the required (angular) frequency discretization, that is, an array of discrete values of ω. The formulae for the frequency spectrum are given in Equation 3.5 and Equation 3.6.

$$S(\omega) = \left(\frac{A_g H_s}{4}\right)^2 \frac{\omega}{\omega_p}^{-5} e^{\left(-\frac{5}{4}\frac{\omega}{\omega_p}^{-4}\right)} \gamma^b \tag{3.5}$$

$$b = e^{-\frac{1}{2\sigma^2}\left(\frac{\omega}{\omega_p}-1\right)^2} \tag{3.6}$$

Where A_g is a normalization factor, ω_p is the peak angular frequency, which is equal to $\frac{2\pi}{T_p}$. γ^r is the peak enhancement factor. σ is the spectral width parameter, which can take one of two values depending on the value of ω. When ω is less than or equal to ω_p, $\sigma = 0.07$; when it is more than ω_p, $\sigma = 0.09$.

First-Order Wave Excitation Force
The forces caused by wave action on a floating platform can be calculated based on a Response Amplitude Operator (RAO). The RAO gives the transfer function of wave excitation force for a given frequency spectrum & heading direction for all six degrees of freedom. This RAO is determined by using boundary integral equation methods, also known as panel methods, to solve the velocity potential and fluid pressure on the floating body. Typically, numerical solvers such as WAMIT or Ansys Aqwa are used to this end.

The unit of the transfer function is generally given in terms of non-dimensionalised force per unit of elevation, where the elevation is the height of the water wave at a given point in time and space. Furthermore, the RAO is given for a range of frequencies and incident angles, and if the data is sufficiently dense, it can be interpolated to give data for any given frequency value within the range or any incident angle.

The time domain solution of the response function of the floating body due to a given wave spectrum is then found with the real part of the inverse Fourier transform of the RAO and frequency spectrum of the wave state.

$$F^{(1)}(t) = \sum_{i=1}^{n} a_i K(\omega_i) cos(\omega_i t + \phi_i + \theta_i) \tag{3.7}$$

Where a_i, ω_i and θ_i are the same as in Equation 3.3, and $K(\omega_i)$ is the RAO for the frequency ω_i and ϕ_i is the associated phase angle.

Second-Order Wave Excitation Force
The solutions to the first-order wave functions were found using a linearisation of the first order. Using a similar method at the second order gives the solution to the second-order problem. As mentioned before in subsection 2.3.5, the magnitude of these solutions will be an order of magnitude smaller, but could result in a significant response in certain scenarios. The standard way of calculating the Force response on the floating body can be found using a Quadratic Transfer Function (QTF) as opposed to the linear transfer function required for the first-order force response.

The determination of these RAOs and the determination of wave forces both take up a considerable amount of time. Thus, it is in some cases convenient to use what is known as the Newman Approximation. This approximation aims to emulate the effect of second-order forces using only the second-order mean drift forces, which can be determined from the results of only the first-order solution. This greatly reduces the computational effort compared to using the full difference QTFs.

This study will use the Newman Approximation to study the effects of higher-order hydrodynamics. This is implemented in a similar manner as the first-order forces. The exact formulation used can be seen in Equation 3.8, taken from the formulation used in the HydroDyn module of OpenFast as presented by T. M. Duarte et al., 2014.

$$F_k^{(2)}(t) = \left[\Re \left(\sum_{m=1}^{N} a_m \sqrt{2F_k^-(\omega_m, \omega_m)} \cdot e^{i\omega_m t} \right) \right]^2 \Bigg|_{F_k^-(\omega_m,\omega_m)>0} - \tag{3.8a}$$

$$\left[\Re \left(\sum_{m=1}^{N} a_m \sqrt{2F_k^-(\omega_m, \omega_m)} \cdot e^{i\omega_m t} \right) \right]^2 \Bigg|_{F_k^-(\omega_m,\omega_m)<0} \tag{3.8b}$$

Where $F_k^-(\omega_m, \omega_m)$ is the diagonal terms of the second-order difference QTF, which are defined as the mean drift loads. The mean drift loads can be determined by programs such as WAMIT or Ansys Aqwa. This study uses the output of Ansys Aqwa, as provided in the definition of the TripleSpar floater (Lemmer et al., 2020).

3.3.3. Mooring Line Representation

The mooring Line representations considered are of a linear, quasi-static, and dynamic nature. The physical data used in the analysis of these systems is given in the definition of the TripleSpar Floater (Lemmer et al., 2020).

Linear Representation

The linear mooring line model is the simplest mooring model considered. This model consists of a 6x6 stiffness matrix that is added to the Equation of Motion (EOM) that describes the floater dynamics. This is the only term in this system that gives the system stiffness in terms of surge and sway, that is, a restoring force based on a displacement from the zero position, since this term is not present in the hydrostatic matrix.

Quasi Static Representation

The quasi-static mooring line model used in this study is based on the representation used in the Mooring Analysis Program (MAP++) that can be used in combination with OpenFast to do numerical simulations on FOWTs, as presented by Masciola et al., 2013. The model makes use of a catenary equation to solve for the tension at the fairlead at each of the mooring lines. To this end, the approach takes into account line extension and seabed contact.

If the mooring line is sufficiently long, part of the mooring line will be in contact with the seabed. For such a line, a catenary equation can be used to represent the line starting from the point where the mooring line lifts off the seabed. The location where the mooring line lifts off the seabed can be found as described in the paper by Zhong et al., 2024. A schematic overview of the mooring line representation can be seen in Figure 3.3

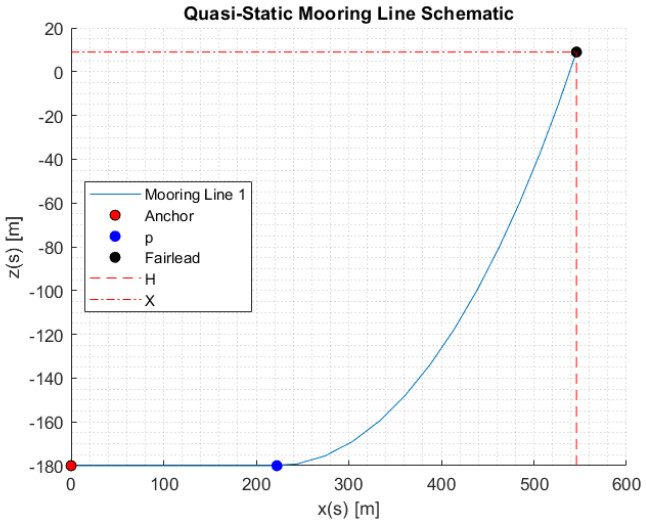

Figure 3.3: Schematic Overview of a mooring line in the Quasi-static mooring line model, in the $x(s) - z(s)$ coordinate system.

Solving Equation 3.9 for p gives the length of the line that is in contact with the seabed, where L is the total length of the line, X the horizontal distance between the anchor and fairlead, and H the vertical distance between the anchor and the fairlead.

$$e^{\left[(X-p)\frac{2H}{(L-p)^2-H^2}\right]} - \frac{2H}{L-p-H} - 1 = 0 \tag{3.9}$$

The value of p then indicates the length of the line (starting from the anchor) that is lying on the seabed. From the value of p, the horizontal tension at any point in the line can be found by using the catenary parameter, as found in Equation 3.10 and Equation 3.11

$$a = \frac{(L-p)^2 - H^2}{2H} \tag{3.10}$$

$$T_h = aW \tag{3.11}$$

Where W is the net weight of the mooring line in the fluid medium per unit length.

The cartesian coordinates of the fairlead and anchor position are transformed into a 2 dimensional plane, where the $X(s)$ is the horizontal plane of the mooring line and $Z(s)$ the vertical plane, both as a function of s, which represents the location along the unstretched length of the line. The piecewise equations for $X(s)$ and $Z(s)$, as well as the tension $T(s)$, are shown in Equation 3.12.

$$X(s) = \begin{cases} s & \text{for } 0 \leq s \leq \gamma \\ s + \frac{C_B W}{2EA}\left[s^2 - 2s\gamma + \gamma\lambda\right] & \text{for } \gamma \leq s \leq p \\ p + \frac{T_h}{W} sinh^{-1}\left[\frac{W(s-p)}{T_h}\right] + \frac{Hs}{EA} + \frac{pW}{2EA}\left[\gamma\lambda - p^2\right] & \text{for p} \leq s \leq L \end{cases} \tag{3.12a}$$

$$Z(s) = \begin{cases} 0 & \text{for } 0 \leq s \leq p \\ \frac{T_h}{W}\left[\sqrt{1 + \frac{W(s-p)}{T_h}^2} - 1\right] + \frac{W(s-p)^2}{2EA} & \text{for } p \leq s \leq L \end{cases} \tag{3.12b}$$

$$T(s) = \begin{cases} max\left[T_h + C_B W(s-p), 0\right] & \text{for } 0 \leq s \leq p \\ \sqrt{T_h^2 + \left[W(s-p)\right]^2} & \text{for } p \leq s \leq L \end{cases} \tag{3.12c}$$

Where $\gamma = p - \frac{T_h}{C_B W}$, and $\lambda = \begin{cases} \gamma & \text{if } \gamma \geq 0 \\ 0 & \text{otherwise} \end{cases}$. The tension forces need to be transformed back to the global 3-dimensional reference system before they can be applied to the floater. Additionally, the moment arm to the Center of Mass (CoM) of the floater needs to be established to determine the resultant moments. A 3-dimensional overview of the mooring system and forces is shown in Figure 3.4a. Figure 3.4b shows a close-up of the fairleads where the z-axis is drawn on the same scale as x and y.

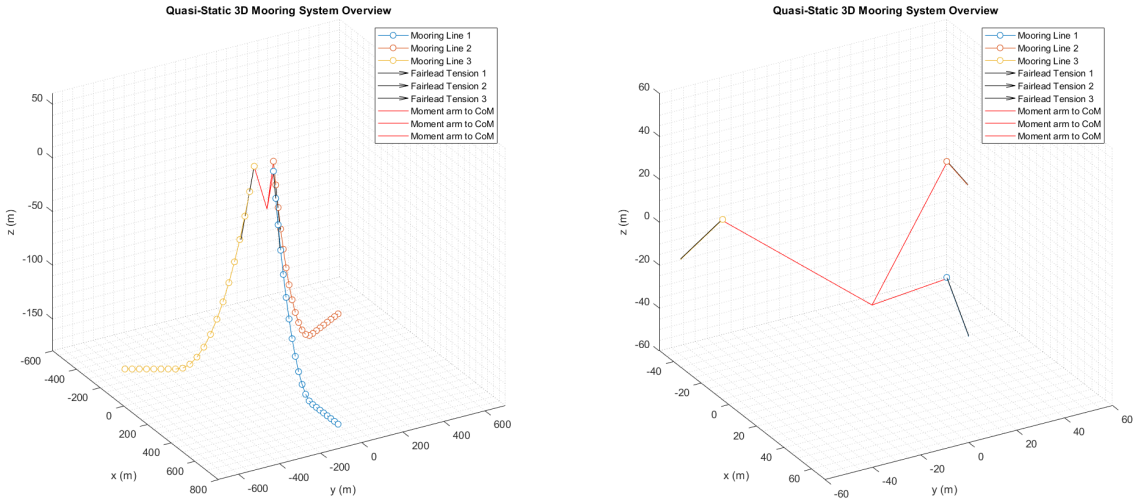

(a) Zoomed out overview (note z-axis not to scale)

(b) Close-up of the fairleads

Figure 3.4: Visual representation of the discretization of the mooring system, produced by the quasi-static model.

Dynamic Representation

In subsection 2.3.8 it was noted that there are a few methods to derive a dynamic representation of individual mooring lines. In this study, it was chosen to use a Lumped Mass (LM) model to represent the mooring lines. The exact modeling method was taken from (Hall & Goupee, 2015). In LM models, the

mooring line is split up in N equally spaced segments and $N+1$ nodes at the end of each segment. The location of each of the nodes is defined in terms of a vector $\mathbf{r}_i$ in Cartesian coordinates from the origin of the global reference system. The global reference system has its origin in the 0 position of the floater, at the intersection between the platform and the turbine tower. The location of the mooring anchors is then defined from this point. Properties of the line segments are defined in terms of unstretched length l, mass density ρ, Young's modulus E and internal damping coefficient C_{int}.

The model takes into account the effect of internal tension and damping forces, hydrodynamic forces in terms of Morison drag loads, weight and buoyancy, and seabed interaction loads. The nodes form a system of connected differential equations, where each of the nodes is affected by the segments it is connected to.

The boundary conditions are set at the anchors and fairlead. At each of these nodes, there is only one connected segment. Additionally, there are constraints that restrict the motion of the fairlead and anchor. For the anchor, the location is fixed. The total tension in the line at the anchor is counteracted by an equal and opposite force, thus remaining in place. Any effects of movement of the anchor due to seabed elasticity are not taken into account. As for the Fairlead, the location and velocity of the node are dependent on the location and velocity of the floater. The exact implementation will be discussed separately in subsection 3.4.5.

For each of the nodes, the weight of half of the segment before and after the node of interest are applied. Again, at the anchor and fairlead, there is only one segment connected to the node, so only one segment is taken into account. Each node i is connected to the previous segment $i-1$ and the next segment $i+1$. The weight at each node is calculated by taking half the previous and half the following segment. The weight of each segment can be calculated according to Equation 3.13

$$W_{i+1/2} = \frac{\pi}{4} d^2 l (\rho_w - \rho) g \tag{3.13}$$

The total weight at the node is then:

$$\mathbf{W}_i = \frac{1}{2} W_{i-1/2} + W_{i+1/2} \hat{\mathbf{e}}_z \tag{3.14}$$

Where $\hat{\mathbf{e}}_z$ is the unit vector in the z direction. The tension in cable segments is caused by the elongation of the line segment from its unstretched length. This particular model does not does not take into account negative tension (i.e. compression), when the length of a line segment is shorter than the original unstretched length, the tension is zero.

The vector force of the tension in the segment i+1/2 is then:

$$\mathbf{T}_{i+1/2} = E \frac{\pi}{4} d^2 \left(\frac{1}{l} - \frac{1}{||\mathbf{r}_{i+1} - \mathbf{r}_i||} \right) (\mathbf{r}_{i+1} - \mathbf{r}_i) \tag{3.15}$$

Internal damping forces are caused by a strain rate, that is, a change in length compared to the last time step. The internal vector force can then be calculated by Equation 3.16

$$\mathbf{C}_{i+1/2} = C_{int} \frac{\pi}{4} d^2 \dot{\epsilon}_{i+1/2} \left(\frac{\mathbf{r}_{i+1} - \mathbf{r}_i}{||\mathbf{r}_{i+1} - \mathbf{r}_i||} \right) \tag{3.16}$$

Where $\dot{\epsilon}_{i+1/2}$ is the strain rate, which can be calculated according to Equation 3.17

$$\dot{\epsilon}_{i+1/2} = \frac{\partial \epsilon}{\partial t} = \frac{\partial}{\partial t}\left(\frac{||\mathbf{r}_{i+1} - \mathbf{r}_i||}{l}\right) \tag{3.17a}$$

$$= \frac{1}{2l}\frac{1}{||\mathbf{r}_{i+1} - \mathbf{r}_i||}\frac{\partial}{\partial t}\left[(x_{i+1} - x_i)^2 + (y_{i+1} - y_i)^2 + (z_{i+1} - z_i)^2\right] \tag{3.17b}$$

$$= \frac{1}{l}\frac{1}{||\mathbf{r}_{i+1} - \mathbf{r}_i||}\left[(x_{i+1} - x_i)(\dot{x}_{i+1} - \dot{x}_i) + (y_{i+1} - y_i)(\dot{y}_{i+1} - \dot{y}_i) + (z_{i+1} - z_i)(\dot{z}_{i+1} - \dot{z}_i)\right] \tag{3.17c}$$

The previously stated equations only state the contributions of the following segments. The contributions of the preceding segments can be calculated in the same manner, swapping the indices i+1 for i-1. This concludes the total internal forces in the mooring line. For the external forces, it is important to look at local velocities and normal and tangential directions, necessary for the calculation of drag forces and added mass.

The tangent direction at any node can be calculated as the vector passing through the 2 adjacent nodes, which can be seen in Equation 3.18.

$$\hat{\mathbf{q}}_i = \frac{\mathbf{r}_{i+1} - \mathbf{r}_{i-1}}{||\mathbf{r}_{i+1} - \mathbf{r}_{i-1}||} \tag{3.18}$$

To this end, tangential and normal components of relative velocity between the medium and the mooring line can be determined as follows. In still water, the relative velocity between the water and the mooring line is equal to $-\dot{\mathbf{r}}_i$. The tangential component can be determined from the projection of the relative velocity on the tangent direction, i.e. $(-\dot{\mathbf{r}}_i \cdot \hat{\mathbf{q}}_i)\hat{\mathbf{q}}_i$. The normal component is $(\dot{\mathbf{r}}_i \cdot \hat{\mathbf{q}}_i)\hat{\mathbf{q}}_i - \dot{\mathbf{r}}_i$. In the following equations, the subscript $_{t,i}$ and $_{n,i}$ will indicate the tangential and normal directions of the ith segment, respectively.

$$\mathbf{D}_{n,i} = \frac{1}{2}\rho_w C_{D,n} dl||(\dot{\mathbf{r}}_i \cdot \hat{\mathbf{q}}_i)\hat{\mathbf{q}}_i - \dot{\mathbf{r}}_i||[(\dot{\mathbf{r}}_i \cdot \hat{\mathbf{q}}_i)\hat{\mathbf{q}}_i - \dot{\mathbf{r}}_i] \tag{3.19a}$$

$$\mathbf{D}_{t,i} = \frac{1}{2}\rho_w C_{D,t} \pi dl||(-\dot{\mathbf{r}}_i \cdot \hat{\mathbf{q}}_i)\hat{\mathbf{q}}_i||[(-\dot{\mathbf{r}}_i \cdot \hat{\mathbf{q}}_i)\hat{\mathbf{q}}_i] \tag{3.19b}$$

Where $C_{D,n}$ and $C_{D,t}$ indicate the drag coefficient in the normal and tangential direction, respectively. Similarly, added mass forces are calculated in normal and tangential directions, as is done in Equation 3.20.

$$\mathbf{a}_{n,i}\ddot{\mathbf{r}}_i = \rho_w C_{a,n}\frac{\pi}{4}d^2 l[(\ddot{\mathbf{r}}_i \cdot \hat{\mathbf{q}}_i)\hat{\mathbf{q}}_i - \ddot{\mathbf{r}}_i] \tag{3.20a}$$

$$\mathbf{a}_{t,i}\ddot{\mathbf{r}}_i = \rho_w C_{a,t}\frac{\pi}{4}d^2 l[(-\ddot{\mathbf{r}}_i \cdot \hat{\mathbf{q}}_i)\hat{\mathbf{q}}_i] \tag{3.20b}$$

The last external force that is accounted for is the reaction force of the seabed. This is a vertical force that ensures that the mooring line does not sink through the seabed. To this end, it is only applied when $z_i \leq z_{bot}$ It is calculated according to Equation 3.21.

$$\mathbf{B}_i = dl[(z_{bot} - z_i)k_b - \dot{z}_i c_b]\hat{\mathbf{e}}_z \tag{3.21}$$

The mass of the individual nodes is defined in a 3x3 matrix. In the integration scheme of the equation of motion, the added mass is added to this matrix to be able to calculate the acceleration terms. The mass matrix is defined in Equation 3.22, where I is the 3x3 identity matrix.

$$m_i = \frac{\pi}{4}d^2 l\rho\mathbf{I} \tag{3.22}$$

The total contribution of the added mass for each individual nodes can be found by factoring out the acceleration term in Equation 3.20. This leads to the expression in Equation 3.23

$$\mathbf{a}_i = \mathbf{a}_{n,i} + \mathbf{a}_{t,i} = \rho_w \frac{\pi}{4} d^2 l \left[C_{a,n}(I - \hat{\mathbf{q}}_i \hat{\mathbf{q}}_i{}^\top) + C_{a,t}(\hat{\mathbf{q}}_i \hat{\mathbf{q}}_i{}^\top) \right] \tag{3.23}$$

The final EOM can be seen in Equation 3.24

$$[\mathbf{m}_i + \mathbf{a}_i]\ddot{\mathbf{r}}_i = \mathbf{T}_{i+1/2} - \mathbf{T}_{i-1/2} + \mathbf{C}_{i+1/2} - \mathbf{C}_{i-1/2} + \mathbf{W}_\mathbf{i} + \mathbf{B}_i + \mathbf{D}_{n,i} + \mathbf{D}_{t,i} \tag{3.24}$$

The acceleration vector $\ddot{\mathbf{r}}_i$ on the left-hand side can be separated by dividing both sides by the total mass matrix $[\mathbf{m}_N + \mathbf{a}_N]$. This results in the acceleration vector for all nodes. With these results, a time variant state space system can be made, which can be used to solve the system of equations systematically. The state vector of this system consists of the location and velocity of every node, that is $\begin{bmatrix} \mathbf{r}_N \\ \dot{\mathbf{r}}_N \end{bmatrix}$. The Solution of this system will be the derivative of this vector, i.e. $\begin{bmatrix} \dot{\mathbf{r}}_N \\ \ddot{\mathbf{r}}_N \end{bmatrix}$. It is important to remember that each vector $\mathbf{r}_N$ contains N vectors of size 1 by 3 (x, y, z) coordinates. This means that the total size of the state vector for a single mooring line becomes $2N$ by 3, where N is the total nodes in the mooring line.

It is now easy to see that the size of the matrices becomes quite substantial for increasingly small discretizations of the mooring line, which drastically increases the computational time of the dynamic system. Additionally, for numerical stability of the dynamic system, a sufficiently small time step has to be taken. This time step is up to an order of magnitude smaller than for a quasi-static system, and multiple orders compared to a linear system. Herein lies the problem with dynamic mooring line systems for use in real-time simulation systems: a combination of (comparatively) computationally expensive calculations, with small time step requirements, can limit the usage of dynamic mooring line representations in real-time simulation.

3.4. Implementation In Simulink

The simulation of the floating body dynamics is solved in MATLAB Simulink. This section will describe the architecture of the Simulink files to describe how the mooring line representation and wave forces are implemented. To this end, it is important to note that the verification and HIL tests use slightly different versions, due to the nature of their setup.

This study will differentiate the Simulink architecture in 3 ways: Standalone, Open-Loop (OL), and Closed-Loop (CL). The standalone Simulink variant can be run on any machine, real-time or not, and has no connection to any hardware or sensing equipment. This simulation then only provides information on the numerical modeling of the floater & hydrodynamics. This version of the Simulink model is used in the verification stage of the research, where the mooring line and wave representations will be verified against results from OpenFast simulations. The Standalone model, with no connection to any hardware, can be run at full-scale and model-scale. That is not the case for the open-loop and closed-loop variants, which can only be run at model-scale. A schematic overview of the Simulink and physical system can be found in Figure 3.5

The open-loop and closed-loop use the same architecture, which is run on the real-time simulation machine and connected to the hardware and sensing equipment. The difference lies in the settings. The Open Loop simulation, as the name suggests, does not ”close the loop”. That is, there is no force feedback from the sensing equipment. The goal of this simulation is to produce the same results as the Standalone model, where no force feedback is possible. This is done to provide a check for the actuation of the hardware and to provide a reference for the closed-loop simulations.

The closed-loop simulations use the real-time machine as well as all hardware and sensing equipment connected and working. The force feedback of aerodynamic and inertial forces of the turbine is thus taken into account (after correcting due to scaling laws). These closed-loop simulations are used for most of the experimental wind tunnel tests. The differences in Simulink modeling will be discussed in

more depth in this section. The differences in experimental setup will be discussed in detail in the next section.

The actual Simulink model that is being solved is in each case the same. The Simulink model consists of a number of subsystems and layers. The subsystems each concern themselves with their associated external force on the dynamic system. The layers on top of the main simulation loop are required to manage inputs and outputs. It is the layers above and inputs that are different between the standalone, OL, and CL versions. For instance,the aerodynamic forces subsystem is present in the standalone model, but its input (and thus output) is zero.

In the following sections, the architecture that is discussed is the same between the standalone, OL, and CL versions. They will provide an overview of the subsystems and how the formulations discussed in section 3.3 are implemented herein. The dynamics solver, aerodynamic, and radiation subsystems are not quite the focus of this study, but they will be briefly discussed here for clarity.

3.4.1. Floater Dynamics Solver Subsystem

This subsystem solves the dynamics of the floater, i.e. the EOM presented in subsection 3.3.1. The inputs of this subsystem consist of the total summation of all external forces and moments on the floater, aerodynamic, diffraction, radiation, and mooring forces. This force and moment vector consists of the summation of forces in the 3 translational DOFs and moments in the 3 rotational DOFs. The properties of the system (mass, stiffness, and damping) are read from the MATLAB workspace. The outputs from the system consist of the position, velocity, and acceleration vector of the floater, in all 6 DOFs.

3.4.2. Aerodynamic Forces and Force Correction

In subsection 2.2.1, it was presented that due to scaling law issues, it is necessary to correct the forces measured by the load cell, such that only the aerodynamic contribution is taken into account in the numerical simulation. The load cell measures contributions of not only aerodynamic induced force, but also from other sources. The contributions can be summarized as follows:

- Aerodynamic forces from wind acting on the rotor.
- Gravitational forces due to the weight of the RNA above the load cell.
- Inertial forces due to acceleration in translational degrees of freedom.
- Forces caused by the tangential and centripetal acceleration due to rotational acceleration.
- Torque caused by the acceleration of the wind turbine model in rotational degrees of freedom
- Tangential acceleration of the induces a torque at the load cell.

For applying correct aerodynamic forces and torques in the HIL simulation, all other contributions need to be removed from the total measured forces by a force correction methodology. The force correction methodology itself was outside the scope of the thesis. The methodology presented here is a short summary based on the work done by Thinakaran, 2024.

The equation for measuring acceleration is given in Equation 3.25. The translational acceleration measurements can be directly measured from the 3-DOF MEMS accelerometer that is present in the model; however, the rotational degrees of freedom cannot be directly measured.

$$a_{\text{meas}} = \mathbf{R}^{-1} \cdot \left(-1 \underbrace{\begin{bmatrix} 0 \\ 0 \\ -g \end{bmatrix}}_{a_{\text{grav}}} + \underbrace{\begin{bmatrix} \ddot{X} \\ \ddot{Y} \\ \ddot{Z} \end{bmatrix}}_{a_{\text{trans}}} + \underbrace{\left(\begin{bmatrix} \dot{\phi} \\ \ddot{\theta} \\ \ddot{\psi} \end{bmatrix} \times \left(\mathbf{R} \begin{bmatrix} 0 \\ 0 \\ h \end{bmatrix} \right) \right)}_{a_{\text{tangential}}} + \underbrace{\left(\begin{bmatrix} \dot{\phi} \\ \dot{\theta} \\ \dot{\psi} \end{bmatrix} \times \left(\begin{bmatrix} \dot{\phi} \\ \dot{\theta} \\ \dot{\psi} \end{bmatrix} \times \overbrace{\left(\mathbf{R} \begin{bmatrix} 0 \\ 0 \\ h \end{bmatrix} \right)}^{pos_{\text{tt}}} \right) \right)}_{a_{\text{centripetal}}} \right) \tag{3.25}$$

Where $\mathbf{R}$ is the rotation matrix to move from a rotating frame to a fixed reference frame: $\mathbf{R} = \mathbf{R_z R_y R_x}$, i.e. the product of the rotation matrices in yaw, pitch, and roll, respectively. The definition of these

rotation matrices can be found in Equation 3.26. The external forces are applied in a rotating frame; however, the final dynamics solution requires a fixed frame, such that these forces have to be transformed back to the fixed frame.

$$\mathbf{R}_x = \begin{pmatrix} 1 & 0 & 0 \\ 0 & cos(\phi) & -sin(\phi) \\ 0 & sin(\phi) & cos(\phi) \end{pmatrix}, \mathbf{R}_y = \begin{pmatrix} cos(\theta) & 0 & sin(\theta) \\ 0 & 1 & 0 \\ -sin(\theta) & 0 & cos(\theta) \end{pmatrix}, \mathbf{R}_z = \begin{pmatrix} cos(\psi) & -sin(\psi) & 0 \\ sin(\psi) & cos(\psi) & 0 \\ 0 & 0 & 1 \end{pmatrix} \tag{3.26}$$

The aerodynamic contribution can be determined from the load cell, by subtracting the force correction factor from the total measured forces. The equation for the total measured forces can be seen in Equation 3.27.

$$F_{\text{meas}} = \underbrace{\begin{bmatrix} F_{a,x} \\ F_{a,y} \\ F_{a,z} \end{bmatrix}}_{F_{\text{aero}}} + \mathbf{R}^{-1} \left(+ \underbrace{\begin{bmatrix} 0 \\ 0 \\ -Mg \end{bmatrix}}_{F_{\text{grav}}} - \underbrace{\begin{bmatrix} M\ddot{X} \\ M\ddot{Y} \\ M\ddot{Z} \end{bmatrix}}_{F_{\text{trans}}} - M \underbrace{\left(\begin{bmatrix} \ddot{\phi} \\ \ddot{\theta} \\ \ddot{\psi} \end{bmatrix} \times \left(\mathbf{R} \begin{bmatrix} 0 \\ 0 \\ h \end{bmatrix} \right) \right)}_{F_{\text{tangential}}} - M \underbrace{\left(\begin{bmatrix} \dot{\phi} \\ \dot{\theta} \\ \dot{\psi} \end{bmatrix} \times \left(\begin{bmatrix} \dot{\phi} \\ \dot{\theta} \\ \dot{\psi} \end{bmatrix} \times \overbrace{\left(\mathbf{R} \begin{bmatrix} 0 \\ 0 \\ h \end{bmatrix} \right)}^{pos_{\text{tt}}} \right) \right)}_{F_{\text{centripetal}}} \right) \tag{3.27}$$

Correcting for the aerodynamic torques is not trivial, since the 3-DOF MEMS accelerometer cannot directly measure the angular acceleration. The torque estimation thus depends on translational acceleration and the double-derivative position vector. This expression is provided in Equation 3.28, where z_{lc} is the moment arm between the center of gravity of the RNA and the load cell.

$$T_{\text{meas}} = -\mathbf{R}^{-1} \underbrace{\begin{bmatrix} J_x\ddot{\phi} \\ J_y\ddot{\theta} \\ J_z\ddot{\psi} \end{bmatrix}}_{T_{inertia}} + \underbrace{\begin{bmatrix} -Ma_{\text{meas}}(y) \times z_{lc} \\ -Ma_{\text{meas}}(x) \times z_{lc} \\ 0 \end{bmatrix}}_{T_{mass}} + \underbrace{\begin{bmatrix} T_{a,x} \\ T_{a,y} \\ T_{a,z} \end{bmatrix}}_{T_{aero}} \tag{3.28}$$

The aerodynamic force can be calculated by subtracting the correction factor from the total measured force($F_{\text{aero}} = F_{\text{meas}} - F_{\text{corr}}$), and the correction factor can then be found, simply taking the expression shown in Equation 3.29. The aerodynamic torque can be calculated by subtracting the correction factor from the measured torque ($T_{\text{aero}} = T_{\text{meas}} - T_{\text{corr}}$. The expression for the correction factor in torque can be determined similarly, as done in Equation 3.30

$$F_{\text{corr}} = -M \cdot a_{\text{meas}} \tag{3.29}$$

$$T_{\text{corr}} = -\mathbf{R}^{-1} \begin{bmatrix} J_x\ddot{\phi} \\ J_y\ddot{\theta} \\ J_z\ddot{\psi} \end{bmatrix} + \begin{bmatrix} -Ma_{\text{meas}}(y) \times z_{lc} \\ -Ma_{\text{meas}}(x) \times z_{lc} \\ 0 \end{bmatrix} \tag{3.30}$$

The correction of inertial forces requires knowledge of instantaneous acceleration at the tower top. Currently, only a 3-DOF accelerometer is installed, allowing for measurement of acceleration in translational degrees of freedom. Correcting then, for the rotational degrees of freedom requires derivation using the translational degrees of freedom, which induces a time delay. The previous study by Thinakaran, 2024 found that the induced time delay was 0.7 seconds, which is too much to be able to accurately correct for the torque induced by the moment of inertia. Additionally, the actual value of the moment of inertia of the RNA is not known. In an iterative approach, it was determined that the best results were found assuming the value for moment of inertia to be zero.

This still gives good results in terms of corrected torque in roll and pitch, where other contributions outweigh this effect. However, in yaw, this is not the case, as can be seen by the fact that measured torque on the load cell is only affected by inertia and aerodynamic torques, not by mass, as pitch and roll are. It is found that in yaw, the current force correction methodology is not quite good enough to closely match the open-loop results. A solution to this problem would be to measure the angular acceleration directly and get a good estimate of the moment of inertia of the RNA. However, this would require a 6-DOF accelerometer, which is not within the scope of the current project.

3.4.3. Radiation Subsystem

The Radiation forces on the system are caused by the motion of the structure in the fluid medium. This motion creates disturbances in the surrounding water, i.e. radiated waves. These radiated waves, in turn, influence the motion of the floating structure itself in the form of a damping force.

In subsection 2.3.4, it was shown that there are a few options for modeling the effects of radiation for floating platforms; this study will use a state-space representation. The definition of the TripleSpar floater provides frequency-dependent damping coefficients, calculated by the hydrodynamic panel code WAMIT (C. Lee, 1995). These damping coefficients can be used to generate a state-space system according to system identification techniques such as the ones presented by T. Duarte et al., 2013. Using the state-space method eliminates the need for the calculation of the impulse-response function or memory matrix, which reduces computational time. The resulting state-space system contains 38 states, and as input requires the 6-DOF velocity vector.

3.4.4. Diffraction Subsystem

The Diffraction force due to wave elevation can be implemented quite simply. It was shown in subsection 3.3.2 that a time history of wave elevation and diffraction force can be determined from basic parameters of a sea state, which does not depend on the location and inclination of the floating system. This allows for a time history of diffraction forces to be determined beforehand and to be applied at every time step. This principle applies to the first-order as well as the second-order forces.

3.4.5. Mooring Line Implementation

For the mooring line implementation, two separate subsystems are made, one for the quasi-static mooring representation and one for the dynamic representation. The linear mooring line representation does not require a separate subsystem, since the effect of the mooring line representation is modelled as a stiffness matrix, which is directly added in the floater dynamics solver.

The data for the mooring line system is implemented by MATLAB scripts, which are able to read a MoorDyn input file and use this information to build the mooring models. A first script is used to read all line information (anchor and fairlead points, line material properties, etc.) into a MATLAB struct. For the quasi-static model, this struct is then used in the initialization of the simulation. For the dynamic model, a first estimate of the location of all mooring nodes is required. To this end, a separate MATLAB script is made that runs the quasi-static model. The location of the mooring nodes is then output and used as the initialization of the dynamic model, together with information on the material properties of the mooring line. This is only required before the first time step, to find initial values for the location of all mooring line nodes.

Quasi Static

The flowchart in Figure 3.6 shows an overview of the quasi-static mooring subsystem as it is implemented in the Simulink model. The quasi-static model only takes the current floater position as input. Information about line properties and anchor positions is read in from the MoorDyn input file during initialization of the simulation. For each of the 3 mooring lines, the mooring model is run in parallel.

The first step is to determine the position of the fairlead in the global reference system, based on the position and inclination of the floater. The vector of each fairlead from the zero-position has to be rotated to account for the inclination of the floater in all rotational degrees of freedom. This is done by using the rotation matrices as depicted in Equation 3.26.

Where $\mathbf{R}_x$, $\mathbf{R}_y$ and $\mathbf{R}_z$ are the rotation matrices around x, y, and z , respectively. ϕ, θ, and ψ are the current rotational positions of the floater: roll, pitch, and yaw, respectively. The actual location of the

ith fairlead ($r_{n,i}$) in cartesian coordinates, is found by taking the position of the floater, and rotating the moment arm of the ith fairlead to the center of the floater $\mathbf{r}_{fairlead,i}$, as done in Equation 3.31.

$$\mathbf{r}_{n,i} = [x, y, z]_{Floater} + \mathbf{R}_z\mathbf{R}_y\mathbf{R}_x\mathbf{r}_{fairlead,i} \tag{3.31}$$

This gives the location of the fairlead in the global reference system, which is used in the quasi-static solver to solve the catenary equation and calculate tension forces, as described in subsection 3.3.3. This tension and moment vector is calculated separately for individual mooring lines and added together before being output to the floater dynamics solver.

Dynamic
In the dynamic mooring subsystem, not only the floater position, but also the velocity is necessary. The position of the fairleads in the global reference system is determined in the same way as shown in Equation 3.26 and 3.31. The velocity vector (in Cartesian coordinates) of the fairleads is found by multiplying the angular velocity of the floater with the vectors of the fairlead moment arms, as shown in Equation 3.32.

$$\dot{\mathbf{r}}_{n,i} = [\dot{x}, \dot{y}, \dot{z}]_{Floater} + \Omega\mathbf{r}_{fairlead,i} \tag{3.32}$$

Where Ω is the angular velocity tensor, defined in Equation 3.33.

$$\Omega = \begin{pmatrix} 0 & -\dot{\psi} & \dot{\theta} \\ \dot{\psi} & 0 & -\dot{\phi} \\ -\dot{\theta} & \dot{\phi} & 0 \end{pmatrix} \tag{3.33}$$

Where $\dot{\phi}$, $\dot{\theta}$, and $\dot{\psi}$ are the angular velocities in roll, pitch, and ya,w respectively. The velocity and location of the fairleads give the boundary condition at the end of the mooring line. That is, in the total state vector $\begin{bmatrix} \mathbf{r}_N \\ \dot{\mathbf{r}}_N \end{bmatrix}$, the fairleads are found at the nth index, whereas the anchors are found at the first.

In every time step after the first, the location and velocity of individual nodes along the line are updated from the derivative of the state vector, which is calculated in the solver. The anchor and fairlead points are not updated this way, as the anchor is fixed and the fairlead is constrained by the floater motion.

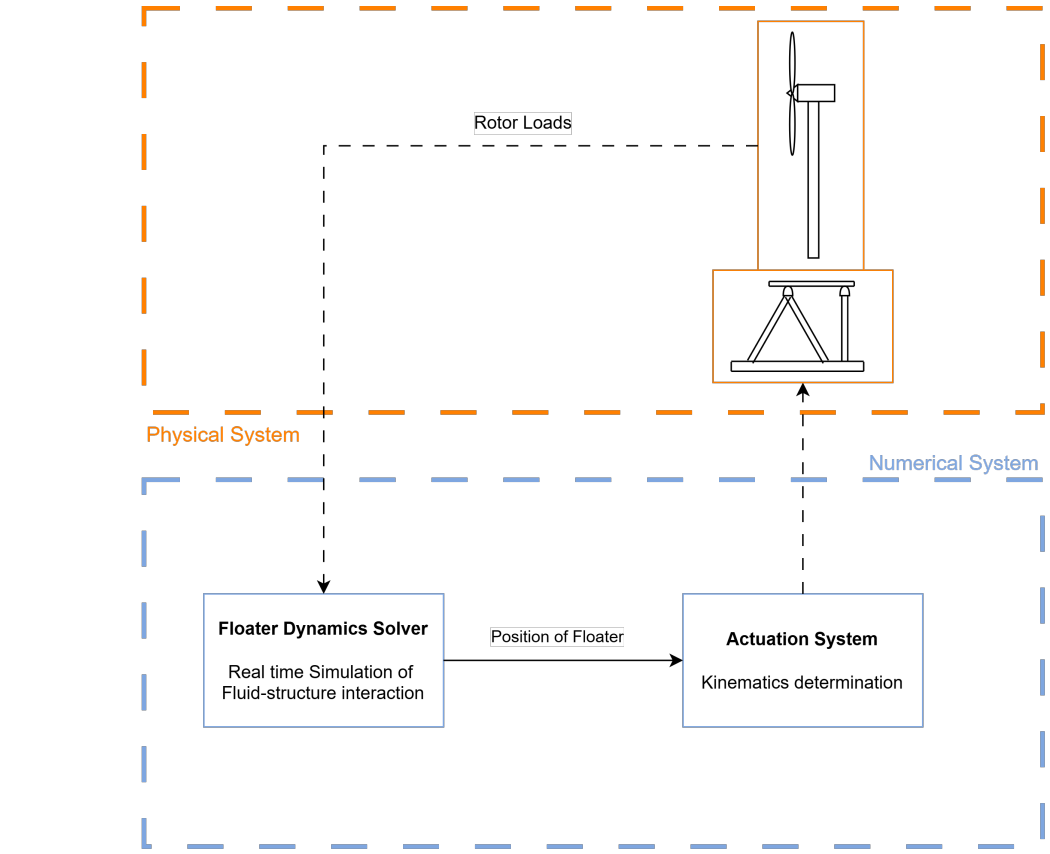

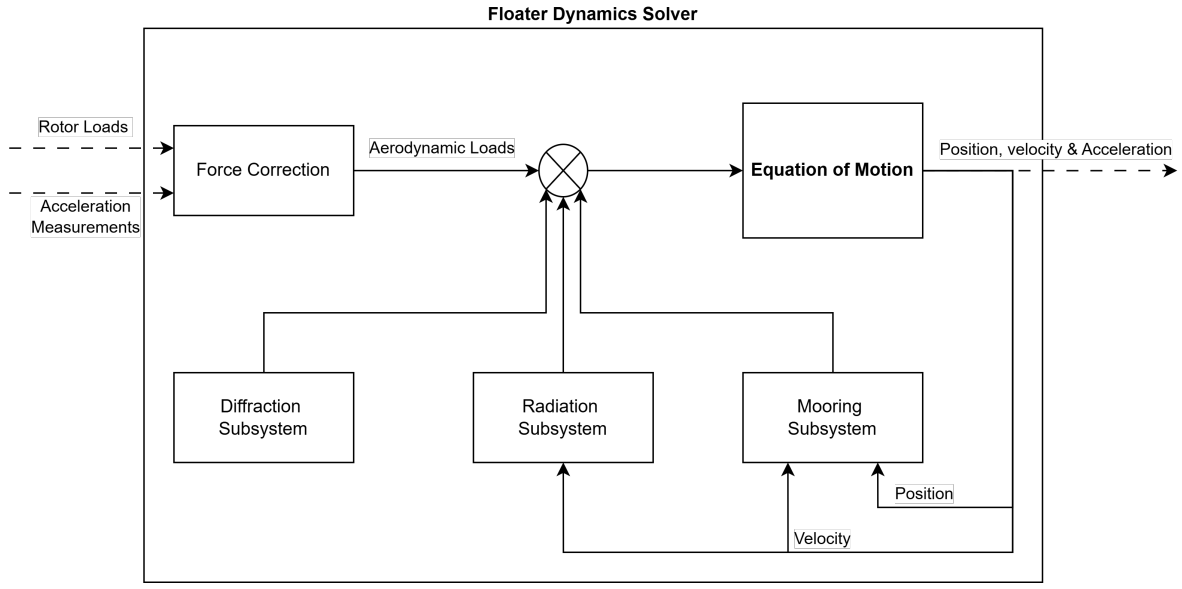

Figure 3.5: Schematic overview of the experimental setup and the floater dynamics solver

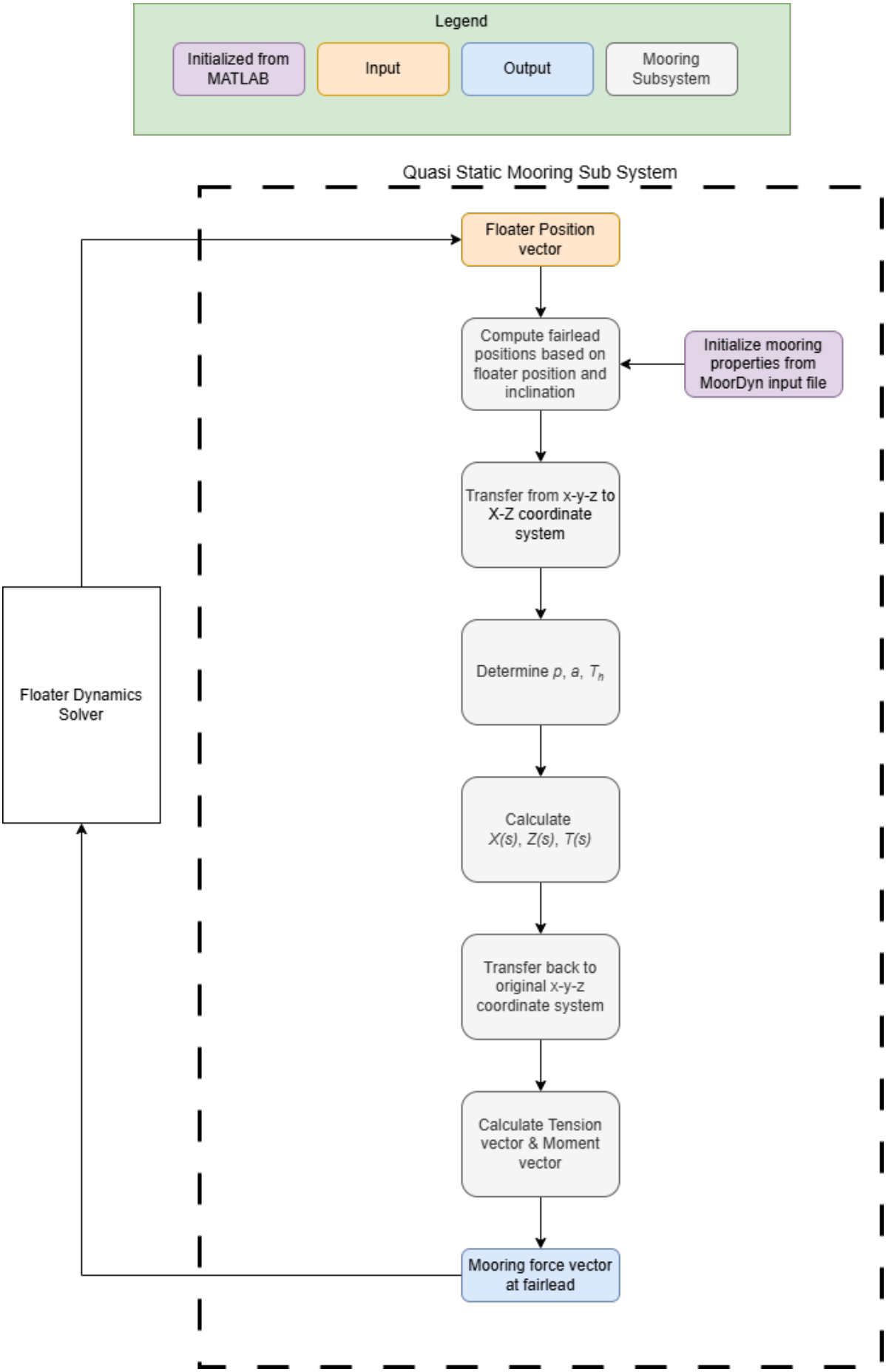

Figure 3.6: Schematic overview of the quasi-static mooring line subsystem

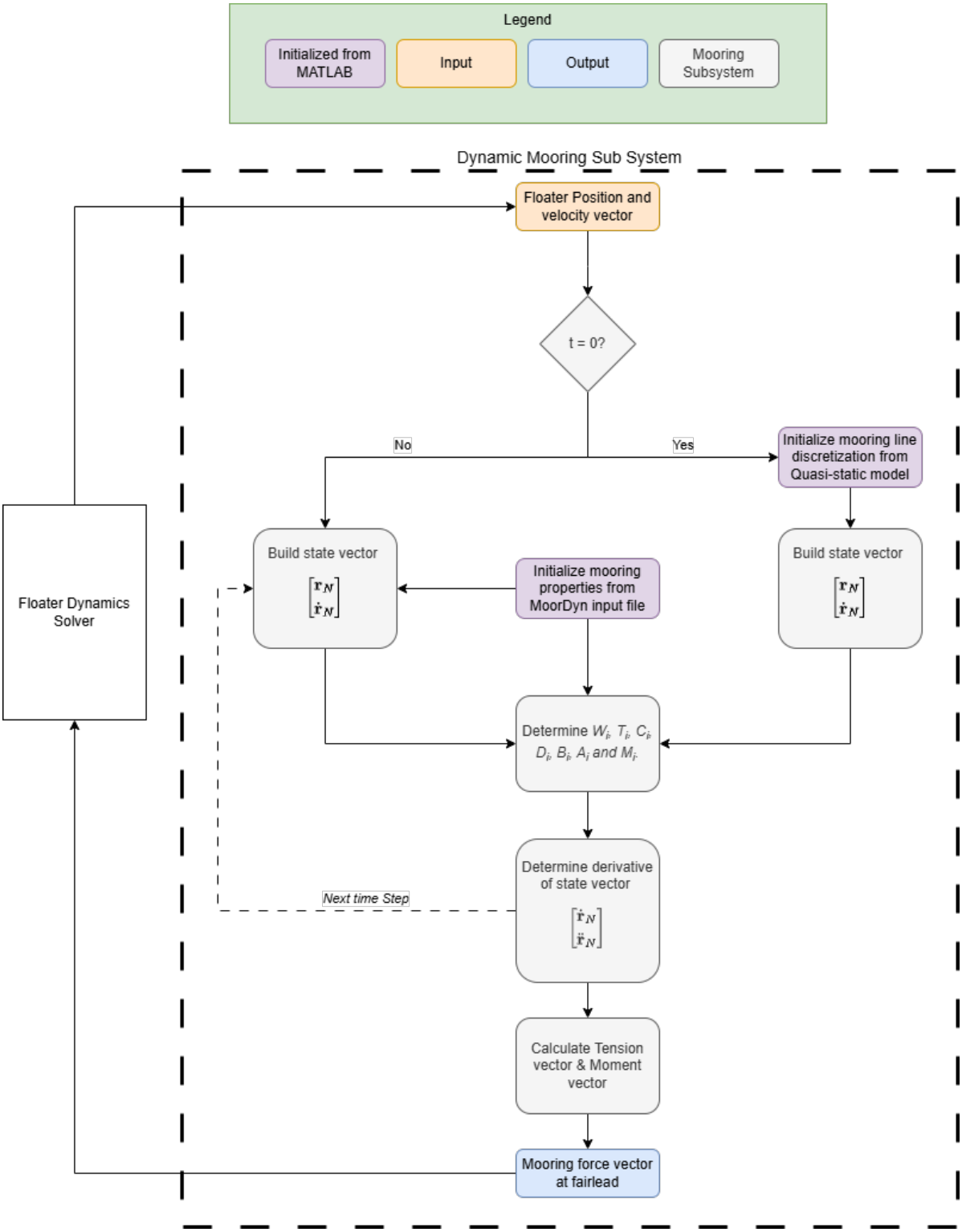

Figure 3.7: Schematic overview of the dynamic mooring line subsystem

4

Assessment

This chapter will present the verification steps that were taken to assess the methodology presented in the previous chapter. For the simulations, data is required for the wind turbine and the floater. The Definition of the TripleSpar floater by (Lemmer et al., 2020) contains an OpenFast repository that contains all the files required to run OpenFast simulations with the data of the TripleSpar floater and DTU10MW wind turbine. This same data is used for the Simulink simulations to provide a good comparison.

The wave generation for first and second-order wave forces is discussed in section 4.1, and verified with the wave generation in OpenFast. Verification of the linear, quasi-static, and dynamic mooring models, in terms of natural frequency, damping ratio, and magnitude of mooring forces, is presented in section 4.2. Additionally, the experimental setup is verified. To this end, the open-loop and closed-loop models are tested in decay tests to verify that the sensing/simulation/actuation loop is working correctly in section 4.3. Furthermore, the scaled wind turbine model is verified by reproducing the wind turbine thrust, torque, and power curves.

4.1. Wave Forces

The wave forces are generated according to the method as presented in subsection 3.3.2, with a Significant wave height H_S of 1.67 meters and a Peak period T_p of 8 seconds. Additionally, the wave heading is chosen to be 0 degrees, i.e., the wave is propagating in the surge (x) direction. For second-order wave forces, the Newman approximation is used. The wave cases examined in this study are taken from a conference paper, presenting the numerical simulation of the DTU10MW reference wind turbine, mounted on the LIFES50+ OO-star Wind Floater Semi 10 MW, in Fast v8 (Pegalajar-Jurado et al., 2018). A selection of wave cases was taken from this study that represent wave cases found in the regular operation of the FOWT. These cases are part of a set of load cases representative of Design Load Case 1.2. The cases that will be examined in this study are presented in Table 4.1. However, in the verification of the wave forces, only the first wave case will be considered. In chapter 5, the other wave cases will also be considered.

Table 4.1: Wave cases considered in verification of wave forces on floater dynamics.

Case	WC1	WC2	WC3	WC4
H_s (m)	1.67	2.2	3.04	4.29
T_p (s)	8	8	9.5	10

The results are compared to the results produced by OpenFast, which uses the same parameters. Figure 4.1 and 4.2 shows the first- and second- order wave excitation force respectively in the time domain. The OpenFast and MATLAB time domain results will never be quite the same, due to the nature of random wave states. However, it can be seen that the order of magnitude of the wave forces is quite similar. Nevertheless, a more accurate comparison can be made in the frequency domain.

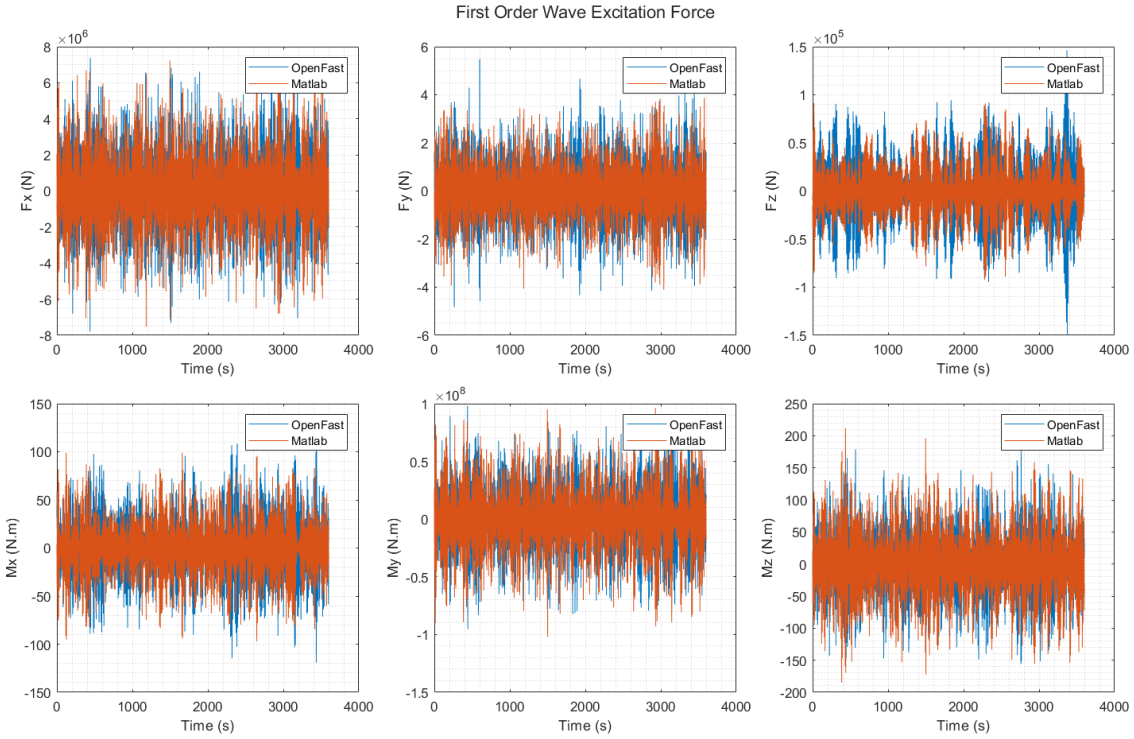

Figure 4.1: First order wave excitation force - Comparison between the MATLAB script and the OpenFast generated wave.

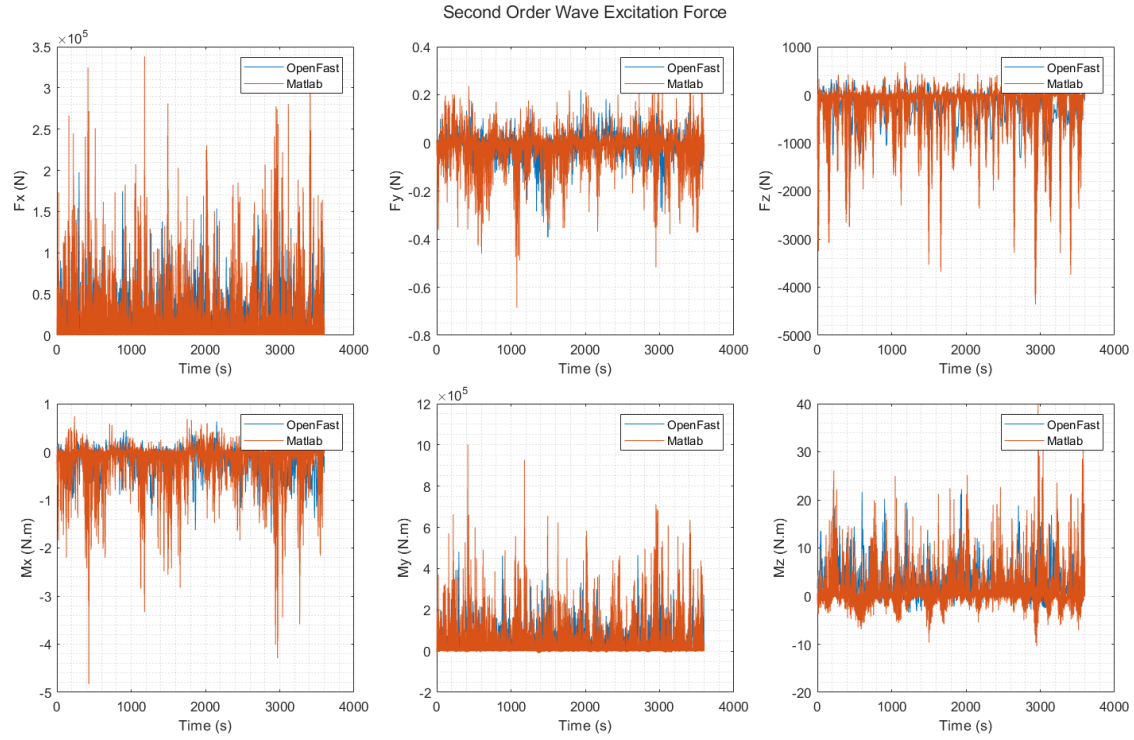

Figure 4.2: Second order wave excitation force - Comparison between the MATLAB script and the OpenFast generated wave.

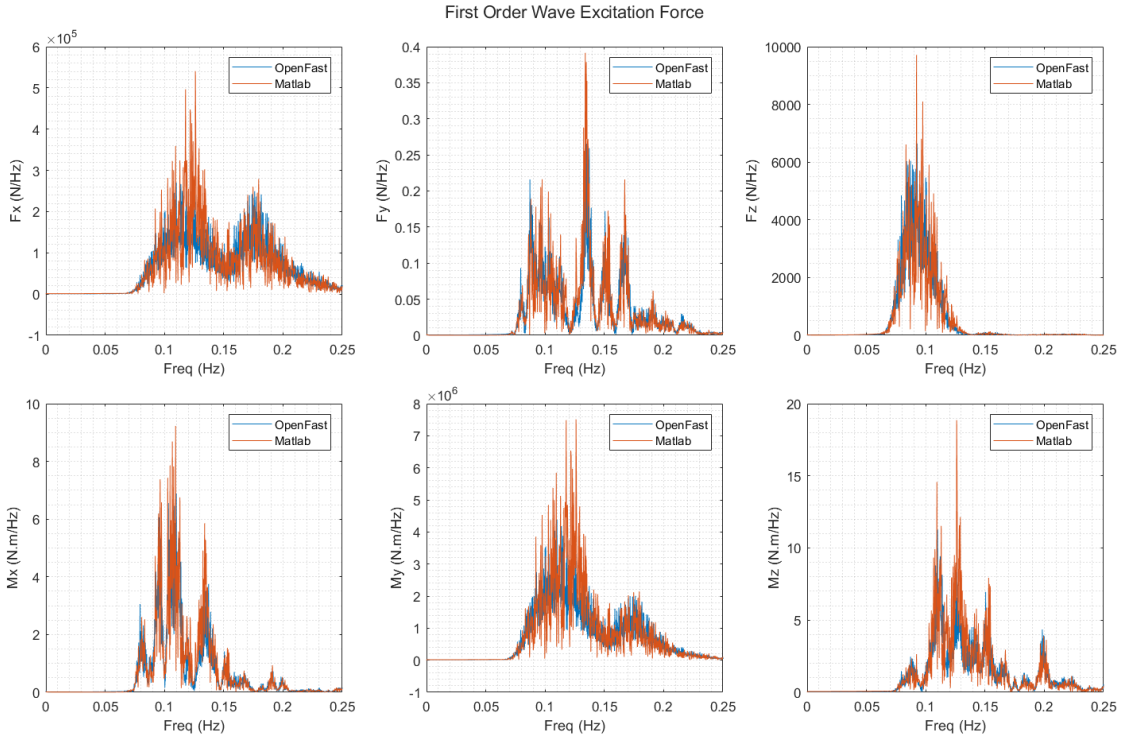

Figure 4.3: First order wave excitation force in frequency domain - Comparison between the MATLAB script and the OpenFast generated wave.

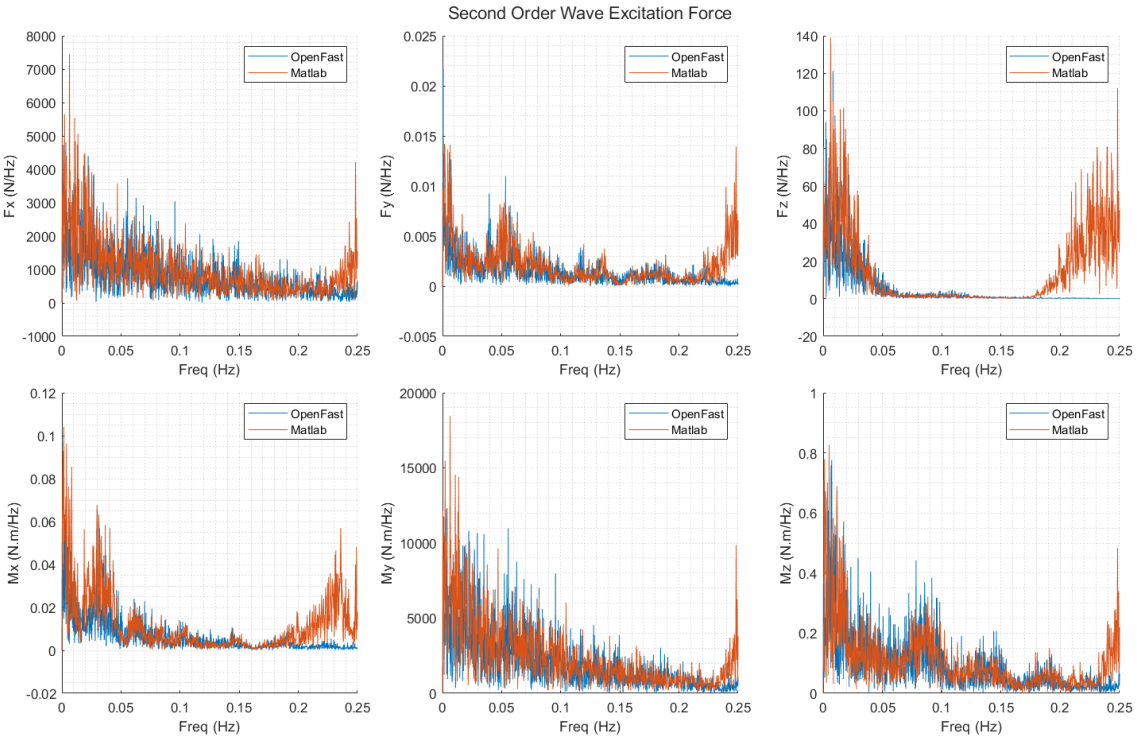

Figure 4.4: Second order wave excitation force in frequency domain - Comparison between the MATLAB script and the OpenFast generated wave.

The frequency domain spectra of the generated waves are shown in Figure 4.3 and 4.4 for first- and

second-order, respectively. For the first-order forces, it can be seen that the frequency spectra closely match. Additionally, it should be noted that the order of magnitude of the forces is quite considerable in surge and pitch degrees of freedom, slightly less in heave, and almost negligible in sway, roll, and yaw; which is expected for a wave with a heading of 0 degrees, acting on a symmetrical floater.

For the second-order forces this trend is similar. Although at the higher end of the frequency spectra from 0.15 to 0.25 Hz, the OpenFast second-order forces are reduced to 0. This is caused by a filter option that OpenFast uses at the higher end of the spectrum, such that only the lower end of the frequency spectrum is taken into account; no such filter was implemented in the MATLAB script.

If such a filter is applied, the spectral results match more closely. The applied low-pass filter is an infinite impulse response filter, with a steepness value of 0.8. The time domain result can be found in Figure 4.5, and the frequency domain result can be found in Figure 4.6. It can be seen that the magnitude of the second-order forces more closely matches the OpenFast results, though there is still some discrepancy in terms of heave force (F_z) and roll moment (M_x) in the 0.2 - 0.25 Hz range.

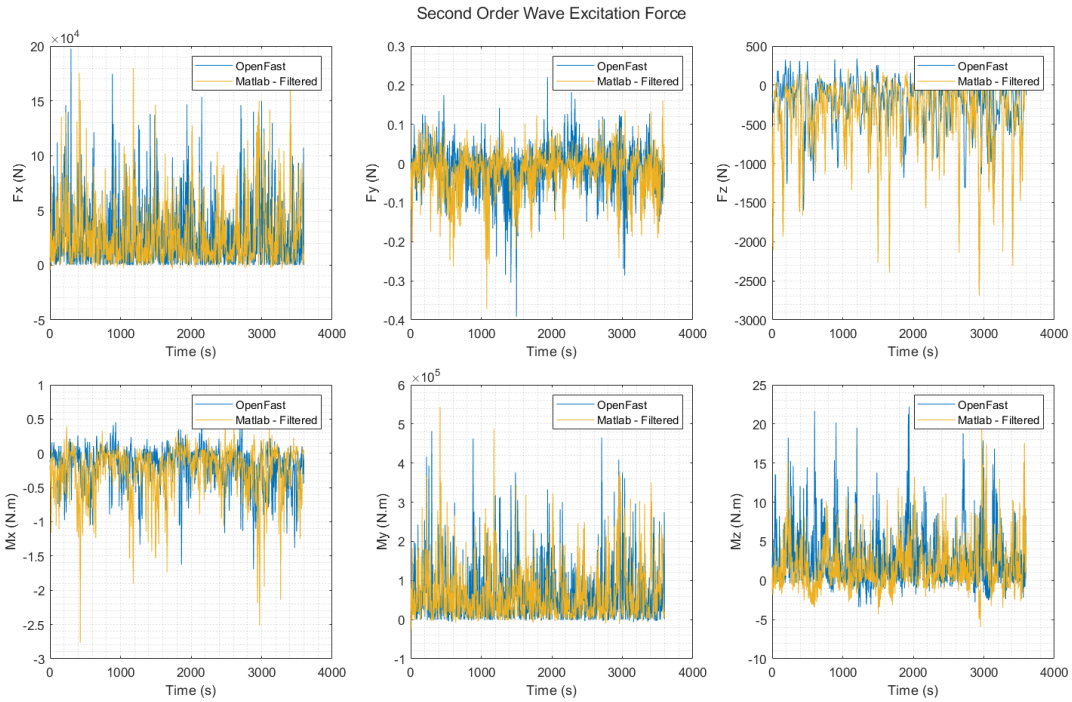

Figure 4.5: Time domain comparison of second-order forces between OpenFast and the filtered MATLAB-generated wave force.

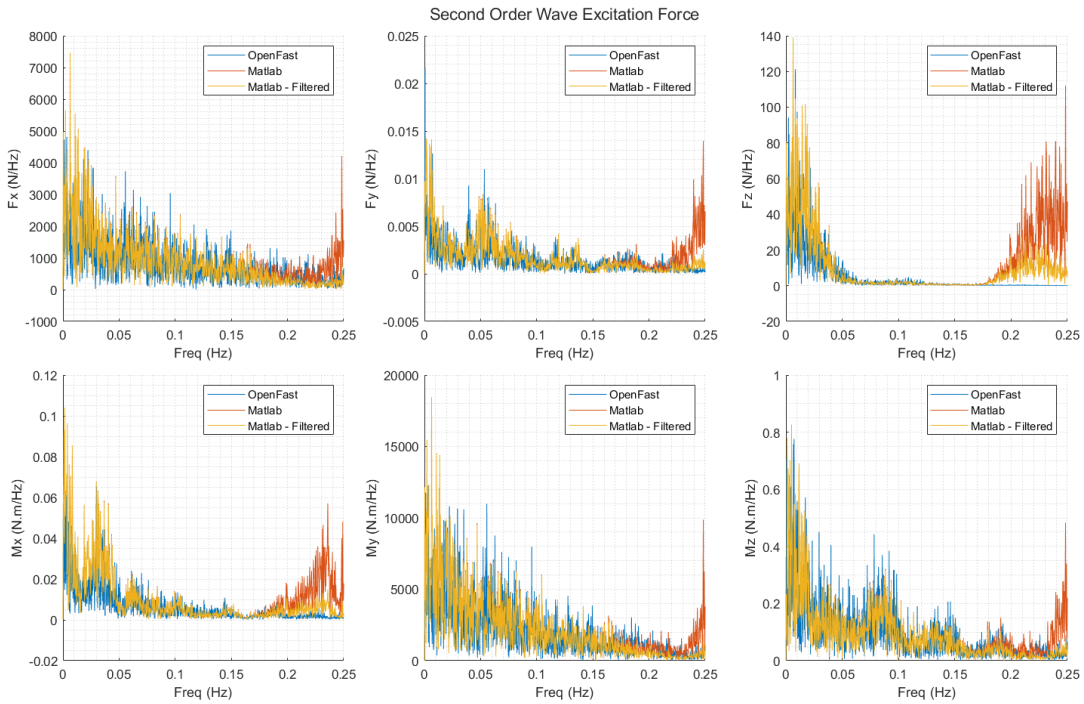

Figure 4.6: Frequency domain comparison of second-order forces between OpenFast and the filtered MATLAB-generated wave force.

This discrepancy is more easily distinguished in a Power Spectral Density graph, as shown in Figure 4.7. The heave force spectral density clearly shows a broad peak at roughly 0.2 Hz that is not present in the OpenFast result. It is reduced by the filter, but not enough to match the OpenFast result as closely as the other degrees of freedom.

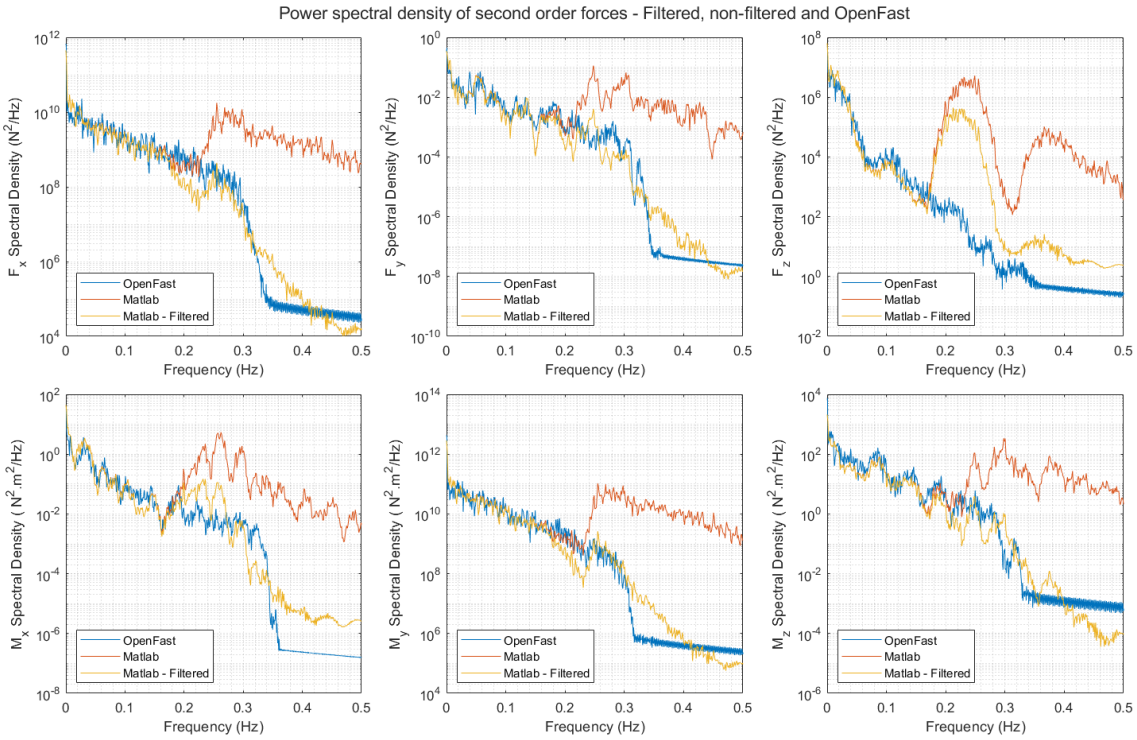

Figure 4.7: PSD of second-order wave excitation force in all degrees of freedom. Note the logarithmic y-axis.

4.2. Mooring Lines

The verification in this section is done by comparing the Simulink simulations to OpenFast simulations. For the Simulink side, the standalone model is used. Verification of the mooring line representations is done by comparing free decay tests of the standalone Simulink model to simulations done using OpenFast. Free decay test allows for the analysis of the stiffness and damping in single degrees of freedom by displacing the system initially. The result is an oscillating motion of the system, with which the damping and natural frequency can be determined.

4.2.1. Natural frequency & Damping

An important distinction to be made here is the difference between the damped frequency and the natural frequency of an oscillation. The relation between the two is shown in Equation 4.1.

$$f_n = \frac{f_d}{\sqrt{1-\zeta^2}} \tag{4.1}$$

Where f_n is the natural frequency, f_d is the damped frequency, and ζ is the damping ratio. Two common methods of determining these parameters are the logarithmic decrement method and the Hilbert transform method. The logarithmic decrement method determines the damping and damped frequency by using the height of the peaks and time difference between peaks, as shown in Equation 4.2 and Equation 4.3.

$$f_d = \frac{1}{T_d} \tag{4.2}$$

Where T_d is the damped period, i.e., the time difference between the peaks.

$$\zeta = \frac{\frac{\delta}{2\pi}}{\sqrt{1+(\frac{\delta}{2\pi})^2}} \tag{4.3}$$

Where δ is the logarithmic decrement, which can be calculated according to Equation 4.4

$$\delta = \log\left(\frac{Value(Peak1)}{Value(Peak2)}\right) \tag{4.4}$$

This method is the most common method of determining the damping and natural frequency of an oscillation, but it has some flaws. In this case, the chosen peaks often matter for determining the damping ratio, where for instance taking the first two peaks or the second and third peaks will result in different values. This makes it difficult to determine what the actual damping ratio of the oscillation is.

The second method, using the Hilbert transform, does not suffer from this problem as much. In essence, the Hilbert transform is a method of applying a 90-degree phase shift to the original signal. Then, combining this signal with the original signal, an envelope can be made along the original signal. Then, using curve fitting techniques, the original curve can be estimated by an exponential function, which is characterized by the natural frequency and damping ratio of the original signal. This is the method that is used in this study to determine the damping and natural frequency of decays in this study, and the exact method is as follows.

The Hilbert transform of a signal can be calculated according to Equation 4.5.

$$\tilde{x}(t) = \frac{1}{\pi}\int_{-\infty}^{\infty}\frac{x(t)}{t-\tau}d\tau \tag{4.5}$$

The resulting signal $\tilde{x}(t)$ is a complex-valued signal that has a phase lag of 90 degrees compared to the real signal $x(t)$. The envelope of the real and complex signal can be determined by taking the vector sum of the two signals, as shown in Equation 4.6.

$$|X|(t) = \sqrt{x(t)^2 + \tilde{x}(t)^2} \tag{4.6}$$

The envelope of the decaying oscillating signal can be characterized as an exponential function, as shown in Equation 4.7

$$|X|(t) = A_0 \exp^{-\zeta\omega_n} \tag{4.7}$$

The value of the exponent $\zeta\omega_n$ can be determined by using curve fitting techniques. In this study, a least squares fit of an exponential function is made to find the value of $\zeta\omega_n$. Figure 4.8 shows an example of a surge decay, with the Hilbert transform and the fitted curve. For the determination of the fitted curve, it should be noted that not the entire signal is taken into account. The first and latter parts of the signal are not useful due to the beginning and ending of the Hilbert transform not providing physical results. In black, the envelope that is considered is indicated, and the fit shows great conformity.

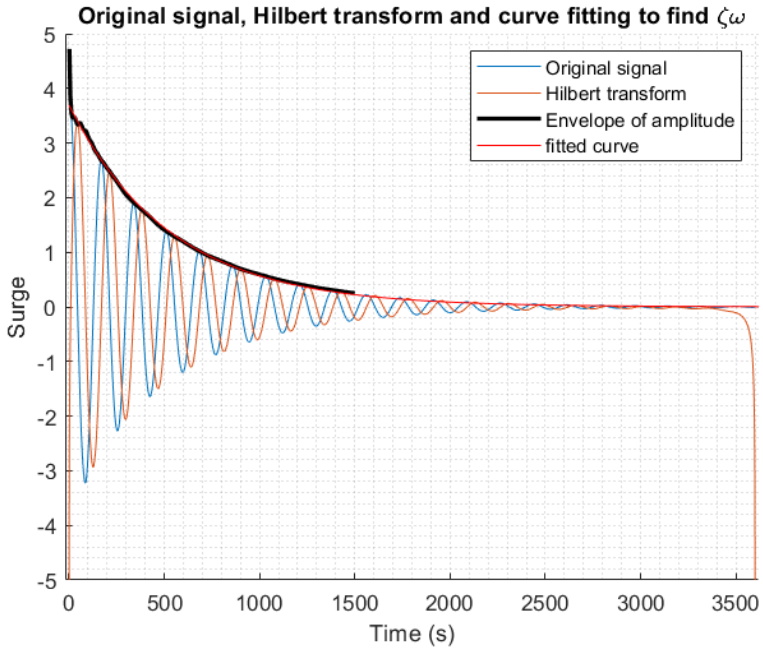

Figure 4.8: Example of a surge decay signal with the Hilbert transform, the amplitude envelope, and the fitted curve.

To find the individual values of ζ and ω_n, we also require the value of the damped angular frequency ω_d. This can also be found using the Hilbert transform, this time using the total phase. For any sinusoidal function, the phase of the signal can be found using the formulations in Equation 4.8.

$$\phi(t) = \omega_d t + \phi_0 \qquad \phi(t) = \tan^{-1}\left(\frac{\tilde{x}(t)}{x(t)}\right) \tag{4.8}$$

From these relations, the damped angular frequency can be found by determining the derivative of the phase signal, as done in Equation 4.9.

$$\omega_d = \frac{d\phi(t)}{dt} \tag{4.9}$$

From the total phase, a least squares linear fit is used to determine the slope of the curve, giving the derivative of the phase, thus the damped angular frequency of the signal. Using the same example signal as before, Figure 4.9 shows the phase diagram. The original phase is given on a domain of $[-\pi \quad \pi]$, which doesn't lend itself to curve fitting. Adding the contributions together gives a better

starting point, indicated as 'phase total' in the figure. Similarly to the previous step, one should be careful with what part of the signal is considered for the curve fitting, as more chaotic signals can show significant jumps in phase, which could introduce an error in the estimation of frequency.

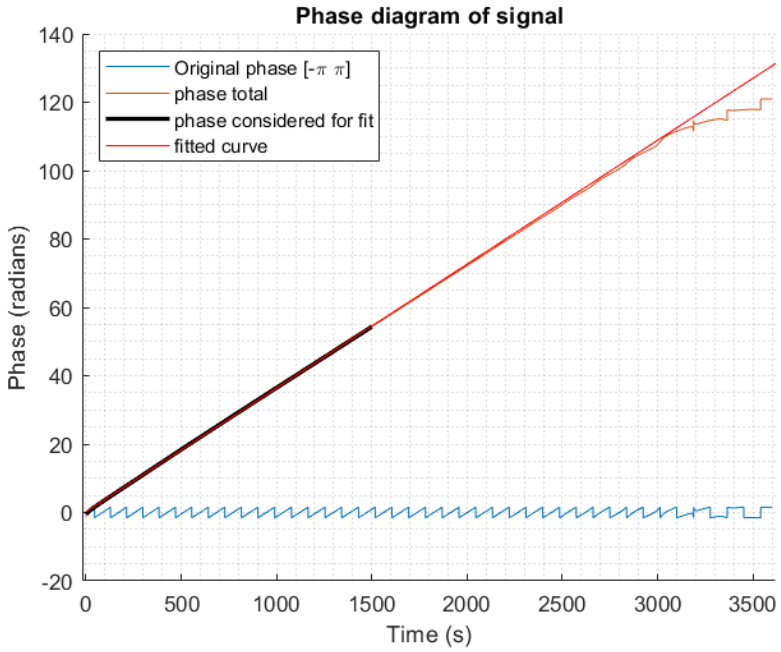

Figure 4.9: Phase diagram of the example signal, showing the process of determining the damped natural frequency from the Hilbert transform.

Then the natural frequency of the system can be found by rewriting Equation 4.1, as done in Equation 4.10.

$$\omega_n = \sqrt{\omega_d^2 + (\zeta\omega_n)^2} = 2\pi f_n \tag{4.10}$$

Finally, the damping ratio can be determined from Equation 4.11

$$\zeta = \frac{\zeta\omega_n}{\omega_n} \tag{4.11}$$

4.2.2. Standalone Decay Tests

The Simulink simulations will be verified by a comparison to OpenFast simulations. To this end, Decay tests are done in all six degrees of freedom in OpenFast and Simulink. For the OpenFast settings, the features of ElastoDyn, ServoDyn, HydroDyn, and MoorDyn modules are enabled. That is, InflowWind and AeroDyn modules are not considered in the analysis, to be able to make a good comparison to the standalone Simulink model, which also does not consider the aerodynamics. Additionally, wave modeling was not incorporated in either the standalone Simulink or the OpenFast simulation. The simulations were run for 3600 seconds to give time for all degrees of freedom to decay.

The initial conditions (IC) considered are shown in Table 4.2, as well as the natural frequencies and damping ratio determined by the Hilbert transform method. The results from the OpenFast simulations

Table 4.2: Damped & natural frequency and damping ratio of the DTU10MW wind turbine & TripleSpar floater in the OpenFast Decay tests.

	Surge	Sway	Heave	Roll	Pitch	Yaw
IC	4 (m)	4 (m)	1 (m)	2 (Deg)	2 (Deg)	2 (Deg)

were used as a baseline; if the resulting natural frequency and damping did not match, stiffness and damping values were added to match the results. That is, if the natural frequency result of the Simulink simulation was too high, negative stiffness was added to decrease the frequency. Similarly, linear and quadratic damping were used to match the damping ratio of the results. This procedure was done for all three mooring line representations: Linear (Lin), Quasi-static (QS), and Dynamic mooring representations (Dyn). The additional stiffness and damping matrices can be found in Appendix A.

As for Simulink, the standalone model was used at model scale. The results were then upscaled again to full scale to be able to compare to the OpenFast results. The time step required for a stable simulation differs between the models. At model scale, the total simulation time is approximately 73 seconds. At this scale, the linear and quasi-static mooring representations were run using a time step of 0.0025. The dynamic representation, however, requires a much smaller time step for numerical stability. The maximum required time step ended up being 5e-5 (1/20000) at model scale.

The discretization of the mooring lines was the same for both quasi-static and dynamic representations, at 20 segments and 21 nodes. This number of nodes was also found to be the optimal amount according to a study by Bayati et al., 2018. This translates to an unstretched segment length of 30 meters at full scale, or approximately 0.2 meters at model scale. This segment length provided the best balance between numerical stability and computational time, as decreasing segment length makes the computational time (for the dynamic model specifically) increase dramatically.

A comparison of the natural frequency and damping ratio between the OpenFast simulations and the Simulink simulations can be found in Table 4.3. The comparative differences between OpenFast and Simulink are shown in Table 4.4

Table 4.3: Natural frequency and damping of the DTU10MW wind turbine & TripleSpar floater in the OpenFast Decay tests.

	OpenFast		Simulink					
Mooring	MoorDyn		Lin		QS		Dyn	
DOFs	f_n	ζ	f_n	ζ	f_n	ζ	f_n	ζ
Surge	0.0058	0.0484	0.0058	0.0534	0.0058	0.0533	0.0058	0.0516
Sway	0.0058	0.0488	0.0058	0.0532	0.0058	0.0532	0.0058	0.0507
Heave	0.0594	0.0732	0.0597	0.0727	0.0593	0.0720	0.0598	0.0751
Roll	0.0389	0.0558	0.0394	0.0546	0.0394	0.0562	0.0393	0.0580
Pitch	0.0390	0.0558	0.0392	0.0533	0.0396	0.0587	0.0386	0.0603
Yaw	0.0133	0.0240	0.0133	0.0240	0.0133	0.0233	0.0131	0.0253

Table 4.4: Difference in natural frequency and damping compared to the baseline OpenFast simulations. Natural frequency and damping are calculated using the Hilbert Transform method.

	OpenFast		Simulink					
Mooring	MoorDyn		Lin		QS		Dyn	
DOFs	f_n	ζ	f_n	ζ	f_n	ζ	f_n	ζ
Surge	-	-	+0.2%	+10.2%	-0.2%	+10.0%	-0.0%	+6.5%
Sway	-	-	+0.4%	+9.1%	-0.1%	+9.1%	-0.1%	+4.1%
Heave	-	-	+0.6%	-0.8%	-0.1%	-1.6%	+0.8%	+2.6%
Roll	-	-	+1.3%	-2.3%	+1.2%	+0.6%	+1.0%	+3.8%
Pitch	-	-	+0.7%	-4.5%	+1.6%	+5.2%	-1.0%	+8.1%
Yaw	-	-	+0.2%	-0.2%	+0.6%	-3.2%	-1.0%	+5.3%

A time history comparison of the decay tests using the linear, quasi-static, and dynamic models can be seen in Figure 4.10, 4.11, and 4.12, respectively. Also included in the figures are the fitted curves of the damping and natural frequency from the Hilbert transform. It should be noted that the time axis for the heave, roll, and pitch decays is shortened to 1200 seconds to provide a better visual comparison.

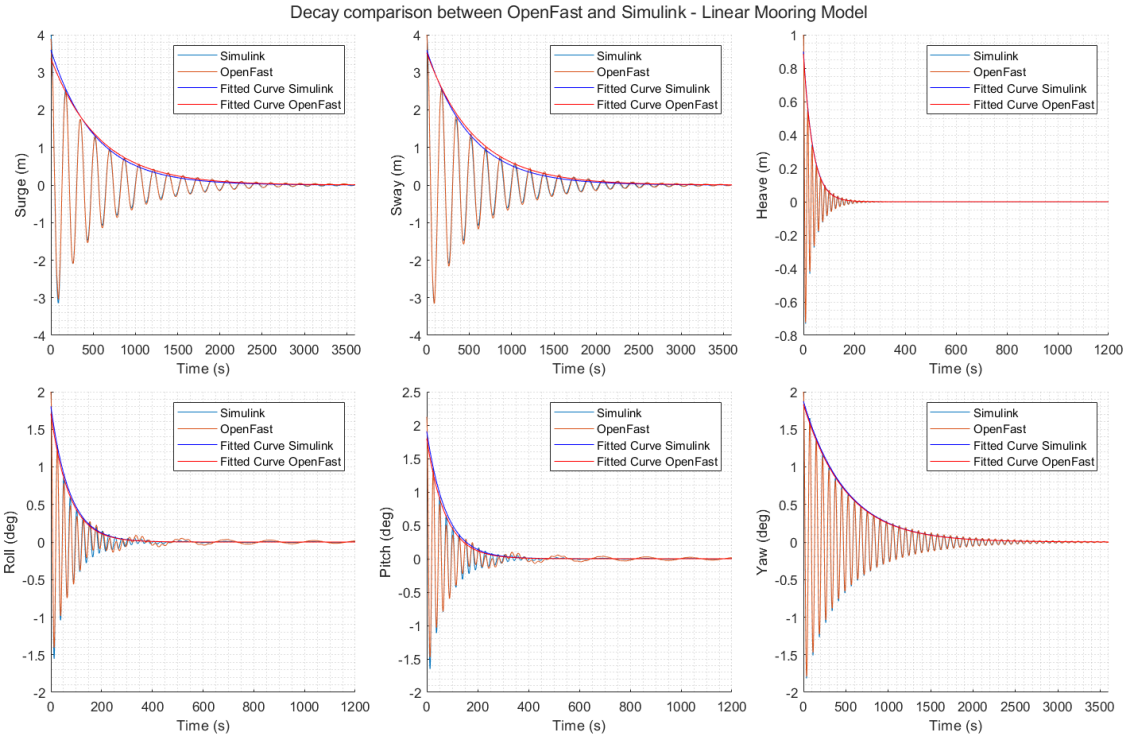

Figure 4.10: Comparison of decay tests between OpenFast and Simulink using the linear mooring representation.

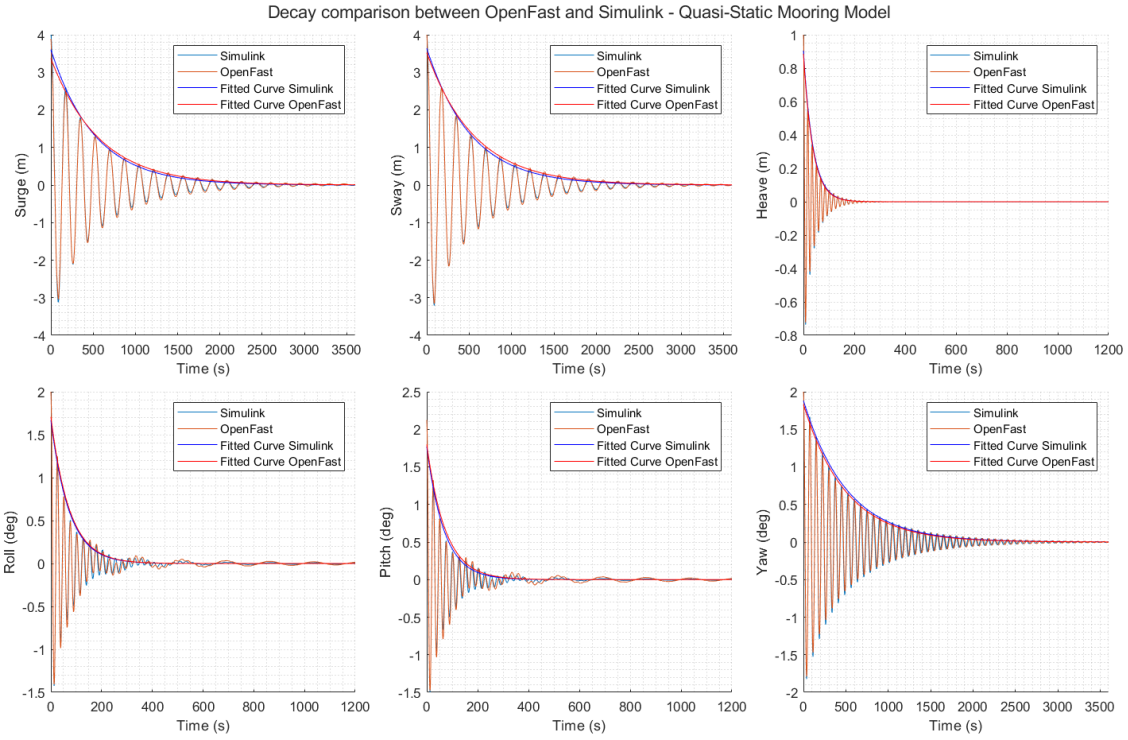

Figure 4.11: Comparison of decay tests between OpenFast and Simulink using the quasi-static mooring representation.

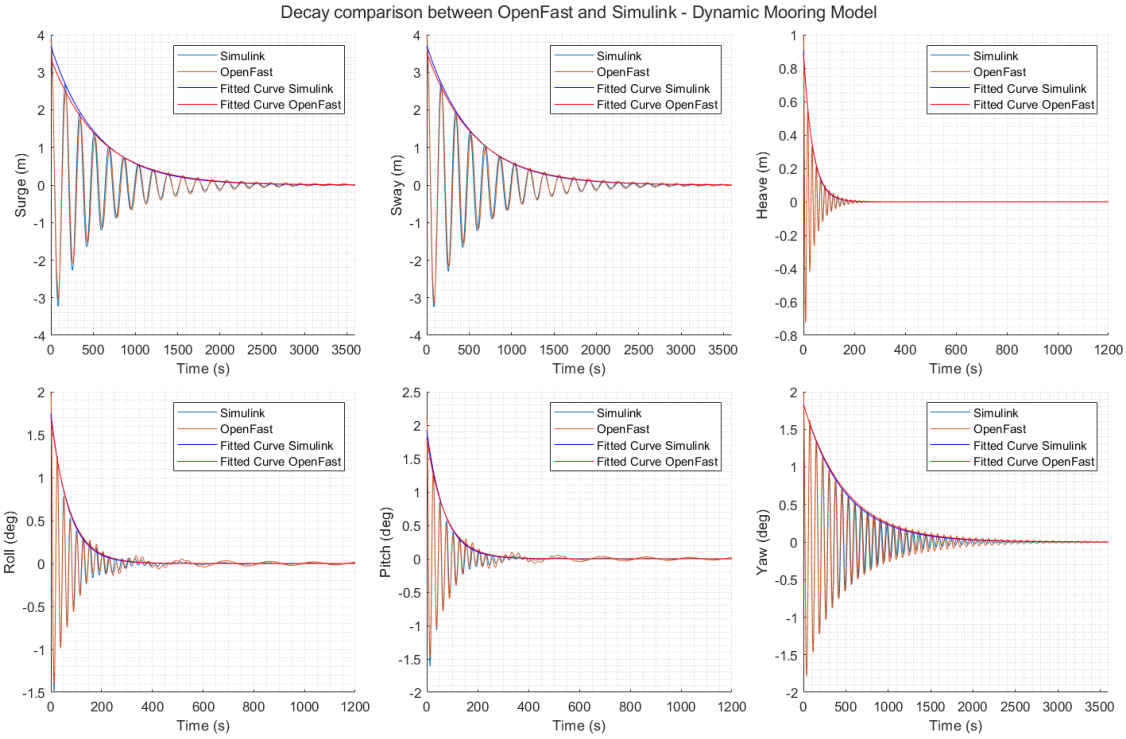

Figure 4.12: Comparison of decay tests between OpenFast and Simulink using the dynamic mooring representation.

For the linear case, good agreement is found especially in terms of natural frequency, with at most 1.3% difference in roll. In terms of damping, the agreement is still quite good, but especially in surge and sway, the damping is a bit higher for the Simulink results. In the roll and pitch degrees of freedom, it is noticeable that the OpenFast result shows an oscillation at the sway and surge frequency, respectively, that is more pronounced than the Simulink results. This is likely caused by a stronger coupling between the roll-sway and pitch-surge degrees of freedom compared to the Simulink model.

The quasi-static model and the dynamic model show similar results to the linear one in terms of surge and sway. However, for the roll and pitch decays, the models show more agreement in terms of coupling in roll-sway and pitch-surge, respectively.

4.2.3. Mooring Force Comparison

To get a better look at the workings of the mooring models specifically, a comparison is made in terms of mooring line tension. To this end, the previously shown decay tests are used, this time presenting the mooring tensions at the fairleads for individual mooring lines. The tension values are output from the OpenFast simulation directly. For the Simulink results, the individual vector components of the force in x, y, and z at the fairlead are added together, such that the magnitude of the vector gives the tension.

Firstly, the quasi-static model is examined. The results from the surge decay and pitch decay are shown in Figure 4.13a and 4.13b respectively. For the sake of brevity, this section only considers these decays as they are the most interesting; the results for the other decays are presented in Appendix B. The tension in the second and third line completely overlaps in these graphs, both for the OpenFast and the Simulink simulation, due to the symmetry plane of these mooring lines going through the x-axis. The most obvious take-away from these graphs is that the quasi-static slightly overestimates the total tension at the fairlead by approximately 10%. The overall shape of the graphs also shows a very good comparison, especially in the surge.

In Figure 4.13b, it can be seen that the oscillation frequency of the largest oscillation amplitude is in line with the frequency of the surge motion. The smaller amplitude, higher frequency component that can be seen in the first 200 seconds of the graph indicates the amplitude of the oscillation in fairlead tension due to a change in pitch angle. The amplitude of this oscillation is very comparable between OpenFast

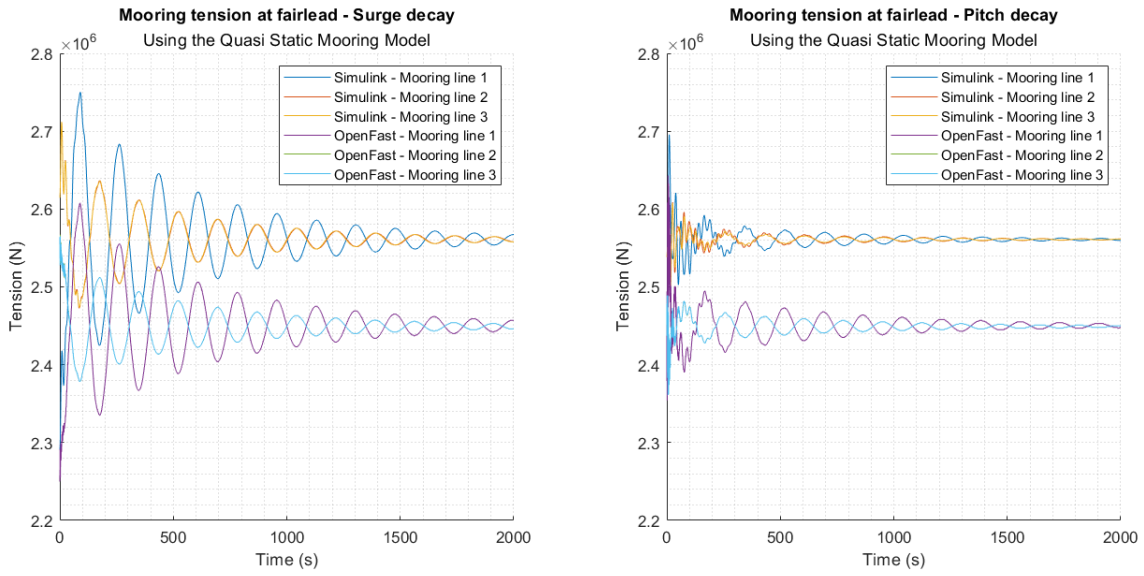

(a) Surge Decay

(b) Pitch Decay

Figure 4.13: Mooring tension at the fairleads in surge and pitch decay, using the quasi-static mooring model. Note that the responses of the second and third mooring lines completely overlap, because they are symmetrical in the x-axis.

and Simulink. The higher amplitude, lower frequency response caused by the pitch-surge coupling is more prominent in the OpenFast result than the Simulink, just like it was noted in subsection 4.2.2.

The mooring tension response in surge and pitch decay from the dynamic mooring model is shown in Figure 4.14a and 4.14b. Again, only surge and pitch are shown here; the other tension figures can be found in Appendix B. The offset in steady-state fairlead tension identified in the quasi-static model is no longer present in the dynamic representation. The dynamic model shows very good agreement both in surge as well as pitch. As noted before, the difference in oscillation amplitude in pitch is caused by the difference in pitch-surge coupling. Furthermore, in the pitch decay, it becomes evident that the Simulink response is more chaotic as the floater reaches steady state.

It should be noted, however, that the dynamic representation in Simulink generates a spike in mooring tension in the first time step that is not found in the OpenFast simulation. This spike in tension is immediately dissipated and does not influence the dynamics of the system significantly, so this was deemed acceptable.

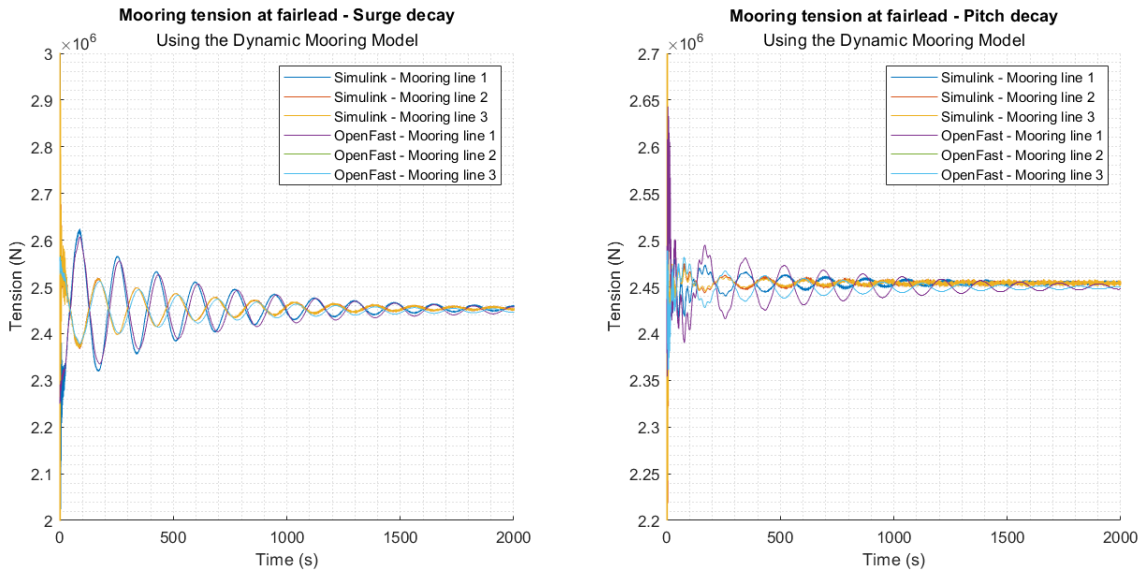

(a) Surge decay

(b) Pitch decay

Figure 4.14: Mooring tension at the fairleads in surge and pitch decay, using the dynamic mooring model.

4.3. Physical Model Verification

The previous sections have focused on the verification of aspects of the numerical simulation. This section will focus on the physical part of the experimental setup, i.e. verification of the performance of the wind turbine model, and verification of the Simulation in open-loop and closed-loop.

Unfortunately, it was not possible to test the dynamic mooring model representation due to restrictions in real-time simulation. As mentioned in subsection 3.3.3, the dynamic model forms the limiting factor in terms of time step for the solving of the dynamics of the system. The required time step to run the dynamic model reduces to 5e-5 s at model scale, which the real-time simulation machine was not able to keep up with. (Bayati et al., 2018) used the same numerical representation as OpenFast and this study in their dynamic mooring line representation. However, in their modeling approach, they consider the different contributions (Weight, tension, damping, et cetera) differently at certain nodes along the line. Their resulting model can resolve the dynamics at a time step of 8e-4 s at model scale, compared to the 5e-5 s at the model scale in this study. This implementation could have worked in this study as well; however, it was not possible to do thorough testing due to time limitations. For the wind tunnel tests, only the quasi-static and linear mooring model was used. For the analysis in the following sections, it will be noted in the text whether the quasi-static or linear model was used, or both. The text itself will only discuss either the linear or quasi-static model, but the data using the other mooring model will be presented in the appendix.

In the experimental campaign, files containing the simulation setup, Simulink model, and properties of the system had to be transferred to a computer to be able to build the Simulink model to be run on the real-time machine. In this process, a mistake was made in selecting the properties file of the floater. Previously, this properties file contained all stiffness and damping values related to the floater, which included the linear mooring system. Because the quasi-static and dynamic mooring systems already account for this stiffness, it was removed from the new properties file. However, when the new files were transferred to the computer, the wrong properties file was included. The old properties file was used, thus accounting for the mooring system twice. This increased the stiffness of the system, especially in sway and surge, which makes comparison to the previous analysis in terms of natural frequency inconsistent. This mistake was only discovered at the end of the experimental campaign, unfortunately, and the restricted time availability in the wind tunnel made it impossible to redo these experiments.

That is not to say that no analysis can be made of the results; comparisons between open- and closed-

loop can still be made, since the stiffness difference is applied in both open- and closed-loop. Additionally, the goal of the open- and closed-loop comparison is to verify the HIL setup itself, not the analysis of the system dynamics. Additionally, comparisons between wind & no-wind cases can be made, as well as effects of wind speed on damping & natural frequency, as will be done in the next chapter. In these analyses, the effect of aerodynamics is central, and the effect of slightly higher stiffness is not detrimental to the analysis of wind action and rotor operation. It has to be taken into account that the system used in the experimental campaign has a higher stiffness than the Standalone model tests, which do have the correct values, which unfortunately means that no connection to the full-scale benchmark can be made.

4.3.1. Open-Loop vs Closed-Loop

Comparison of open-loop and (no wind) closed-loop tests is used to verify that the HIL system is working accordingly. That is, all systems that could only be tested using the physical system, i.e., force feedback, force correction, actuation, and latency of the system. The comparison between open-loop and closed-loop allows for verifying the compensation of inertial forces in the force correction procedure. To reiterate, the difference between Open- and closed-loop is in the feedback of forces measured by the load cell. Since the numerical simulation running on the real-time machine already incorporates the effect of mass and inertia of the wind turbine, it is required to subtract this contribution from the measured forces and moments at the load cell.

Decay tests are done at two initial conditions, as can be seen in Table 4.5. The initial conditions are applied as external forces or moments to the floater, depending on the degree of freedom. The initial conditions are applied, after which artificial damping is added to eliminate any transients. When a steady state is reached at the desired initial condition, the artificial damping is removed, and the recording of the decay is started. After a few seconds, the external force is eliminated, and the system will decay in the desired degree of freedom. The table also shows the approximate offset in millimeters or degrees at model scale (offset$_{ms}$), as well as the offset at full scale (offset$_{fs}$) in meters or degrees to provide a point of reference. The results discussed further in this section are all at model scale.

Table 4.5: Initial conditions of Decay cases used in HIL simulation.

IC		Surge	Sway	Heave	Roll	Pitch	Yaw
IC1	Force/Moment (N/N.m)	3.2	3.2	24	6	6	0.6
	Offset$_{ms}$ (mm/deg)	27	27	6.5	2	2	2
	Offset$_{fs}$ (m/deg)	3.99	3.99	0.96	2	2	2
IC2	Force/Moment (N/N.m)	8	8	60	15	15	1.5
	Offset$_{ms}$ (mm/deg)	65	65	16.5	5	5	5
	Offset$_{fs}$ (m/deg)	9.62	9.62	2.4	5	5	5

The resulting decay graphs for the large displacement, and using the quasi-static mooring model, in time and frequency domain are shown in Figure 4.15 and Figure 4.16, respectively. For the sake of brevity, only the large displacement is shown here; the small displacement graphs and the graphs for the linear mooring model can be found in Appendix C. The time domain response in Figure 4.15 shows good agreement in all degrees of freedom, though there seems to be a very slight difference in natural frequency in the yaw case. The frequency spectra in Figure 4.16 show very good agreement in terms of location of the peaks on the frequency band, even for the yaw case. In terms of peak height, there is a slight difference, but this is not significant.

The decay statistics for open- and closed-loop are shown in Table 4.6, for both initial conditions, using the quasi-static mooring model. The decay statistics for the linear mooring model can also be found in Appendix C. The results were gathered using the Hilbert transform method shown before in subsection 4.2.1. For comparison, the difference between open- and closed-loop is shown in Table 4.7. In this table, the open-loop result is taken as baseline, and the percentage difference in the closed-loop to open-loop result is shown. The largest differences can be found in the roll and yaw decay, where the closed-loop results show a deviation in the damping ratio compared to open-loop. In terms of natural frequency, the decays show very good agreement, with all frequencies being within 2% of the open-loop result.

The difference in the yaw decay can be explained by the force correction of rotational degrees of freedom. As mentioned before in subsection 3.4.2, the correction methodology in rotational degrees of freedom does not correct for the inertial forces, because no acceleration measurement is available in rotational degrees of freedom. This is true for roll and pitch as well, but the effect is not as noticeable there because other contributions overshadow the effect of the inertial forces, but this is not the case in yaw.

Table 4.6: Decay stats of HIL decay tests, open-loop vs closed-loop, using the quasi-static mooring model.

IC	IC1				IC2			
	open-loop		closed-loop		open-loop		closed-loop	
	ζ	f_n	ζ	f_n	ζ	f_n	ζ	f_n
Surge	0.039	0.393	0.039	0.394	0.056	0.394	0.055	0.395
Sway	0.039	0.394	0.039	0.395	0.056	0.394	0.054	0.396
Heave	0.084	3.002	0.086	2.969	0.121	3.102	0.120	3.075
Roll	0.075	1.958	0.069	1.962	0.093	1.993	0.111	1.970
Pitch	0.062	2.010	0.065	2.024	0.095	2.034	0.095	2.047
Yaw	0.018	0.903	0.024	0.891	0.025	0.904	0.030	0.892

Table 4.7: Percentage-wise difference between open-loop and closed-loop decay results, using the quasi-static mooring model.

IC	IC1				IC2			
	open-loop		closed-loop		open-loop		closed-loop	
	ζ	f_n	ζ	f_n	ζ	f_n	ζ	f_n
Surge	-	-	+0.7%	+0.1%	-	-	-1.2%	+0.1%
Sway	-	-	+0.9%	+0.4%	-	-	-3.3%	+0.5%
Heave	-	-	+2.8%	-1.1%	-	-	-1.1%	-0.9%
Roll	-	-	-7.3%	+0.2%	-	-	+19.4%	-1.1%
Pitch	-	-	+4.8%	+0.7%	-	-	+0.1%	+0.6%
Yaw	-	-	+27.8%	-1.3%	-	-	+17.3%	-1.4%

4.3.2. Wind turbine Thrust Curves

The performance of the wind turbine is first tested in static cases, in terms of produced thrust, torque, and power at various operating points. Static cases, in this case, mean a test case in which the HIL simulation is not running, and no floater dynamics are simulated, such that only the wind turbine performance is tested. The thrust (F_T) and torque (T_x) are determined by the load cell, where thrust is equal to the force in the x-direction. The torque can be measured as the roll components of the measured force. Power (P) produced can be determined in 2 ways: calculated or measured power. The calculated power can be determined by using the rotational speed and the torque, i.e. $P = T_x \times \omega_r$, where ω_r is the rotational speed of the rotor. The measured power can be determined from the encoder of the motor/generator, though this value will generally be substantially lower due to mechanical losses in the gearbox and machinery, and electrical losses in the motor.

As mentioned before in subsection 3.2.2, the scaled wind turbine model is a thrust-matched scale model of the DTU10MW turbine. The goal of recreating the rotor thrust at model scale is then the most important factor, which is what we find in Figure 4.17. At the rated wind speed of 4 m/s, the scale model will under-predict the aerodynamic torque and power generation of the full-scale turbine, but the difference is acceptable for the purposes of this study. Additionally, because no pitch control is available to control aerodynamic loads on the wind turbine model, the thrust, torque, and power keep increasing above the rated wind speed, contrary to the reference wind turbine.

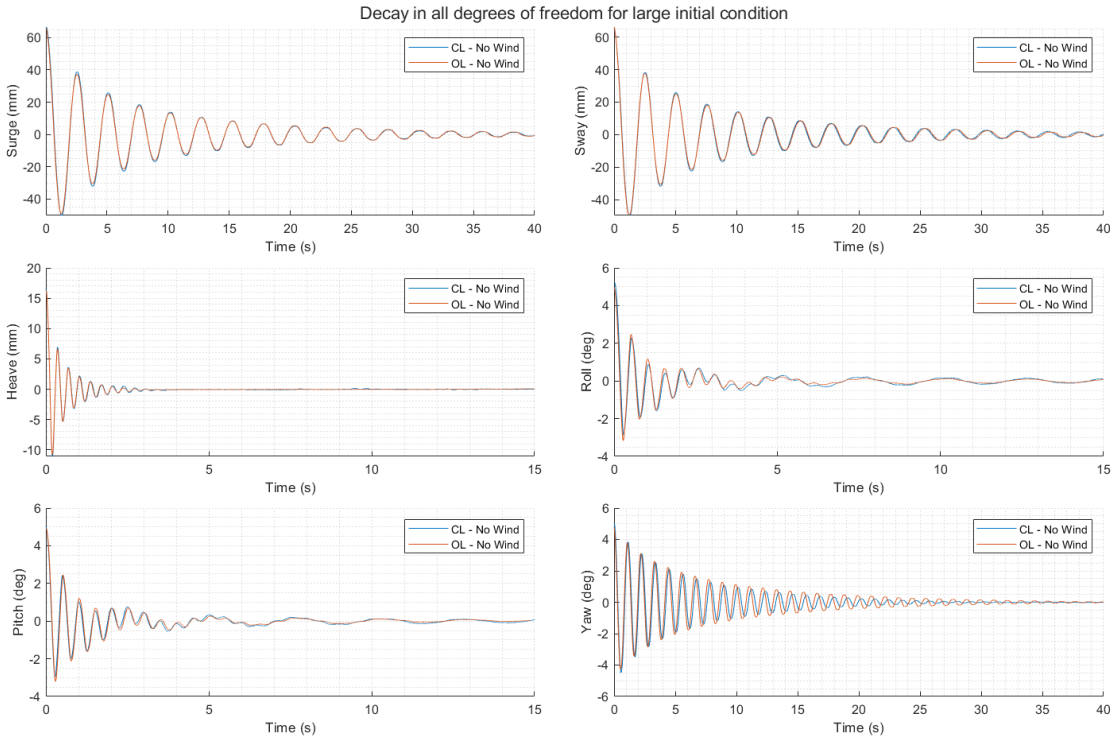

Figure 4.15: Comparison of open-loop vs closed-loop - IC2 - Using Quasi-static mooring model

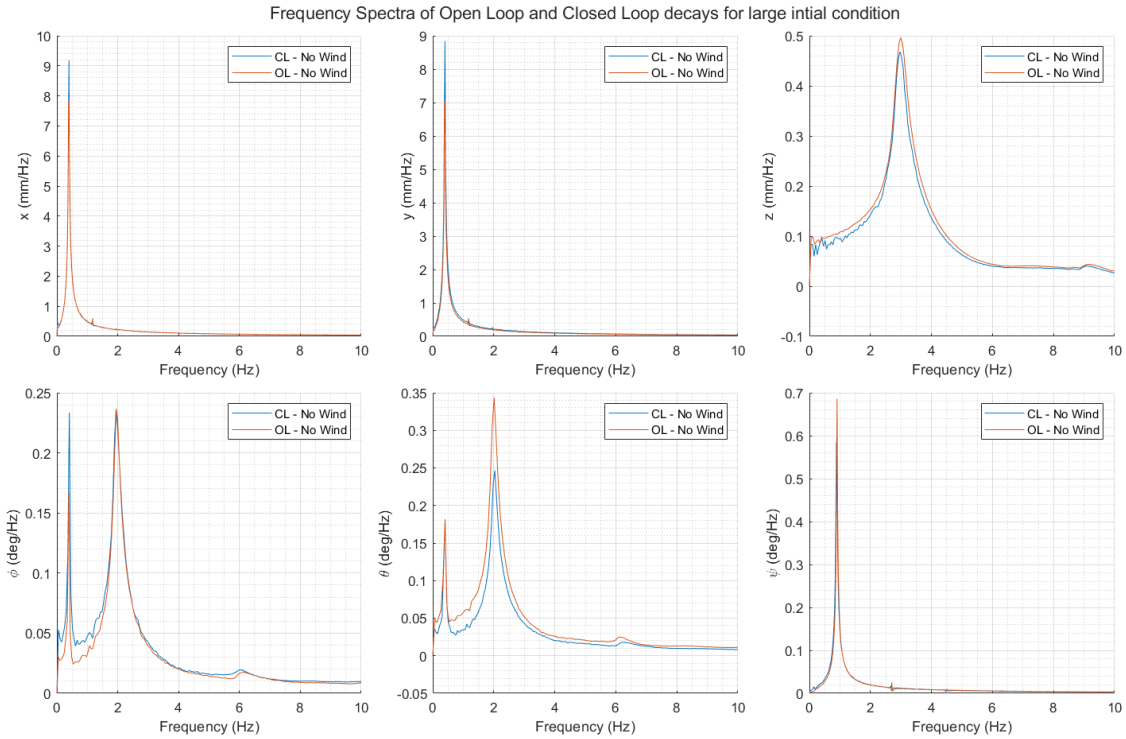

Figure 4.16: Frequency spectra of open-loop and closed-loop - IC2 - Using Quasi-static mooring model

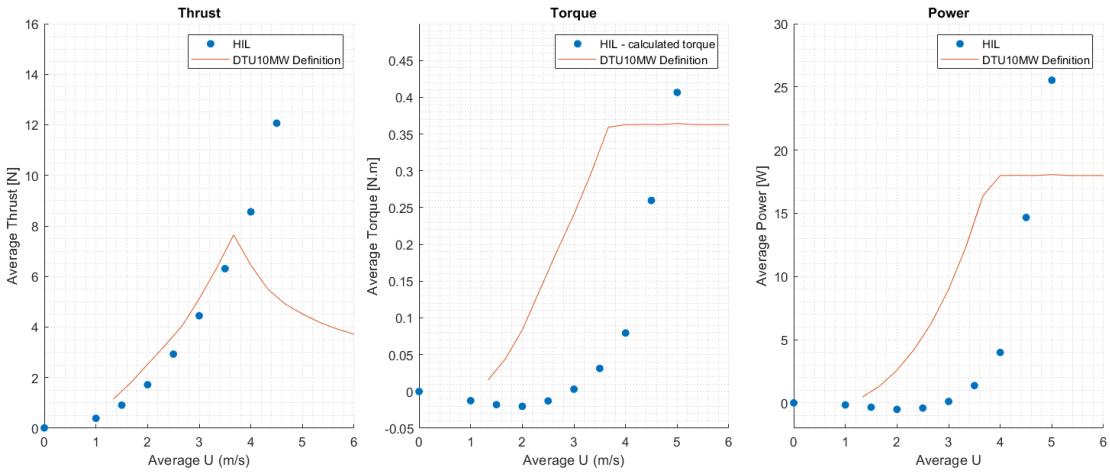

Figure 4.17: Thrust, torque, and power curves. Comparison between the definition of the DTU10MW wind turbine (scaled to model scale) and the experimental results obtained in the HIL tests.

5

Results

This chapter will present the results from the numerical modeling presented in the previous chapters. Firstly, section 5.1 will present the effect of second-order wave forces on floater motion, as well as mooring line tension at the fairlead, simulated in the standalone Simulink model. The rest of the chapter will present the HIL wind tunnel results, where in section 5.2 the effect of aerodynamic forcing on the system was tested in combination with wave cases, subject to both first- and second-order wave excitation forces. Finally, a more fundamental study is done on the effect of aerodynamic damping on surging, pitching, and yawing motion in section 5.3. For a variety of wind speeds, decay tests are done in these degrees of freedom to quantify the increase in aerodynamic damping for increasing wind speeds.

5.1. Wave Action on Floater in Standalone

This section will present the interaction between wave forces on the floater, in the standalone model, to be able to compare the dynamic mooring model to the quasi-static mooring model. With established confidence in the mooring line representations, the effect of the first- and second-order wave forces can be investigated. To this end, simulations were run in Simulink and OpenFast, with wave forces of different values of significant wave height (H_s) and peak period (T_p), here referred to as weak and strong. Additionally, a comparison is made between the different mooring line models. The wave cases considered are the first and fourth wave cases presented in Table 4.1.

The floater displacement for the weak and strong wave forces is shown in Figure 5.1 and 5.2 respectively. Pictured are the displacements in surge and pitch, since these are most affected by the wave forces in 0-degree heading. This figure shows only the Simulink results for the quasi-static model. A comparison between the linear, quasi-static, and dynamic mooring line model is shown in Figure 5.5 and 5.6.

The weak wave forces comparison in Figure 5.1 shows that the inclusion of second-order forces greatly affects the displacement of the floater. Both Simulink and OpenFast simulations show a mean offset in surge that is consistent with the inclusion of the mean drift forces that Newman's Approximation is based on. Pitch shows similar results; the inclusion of second-order forces causes a mean offset in the negative pitch direction, though compared to surge, this is only a small offset. The strong wave forces are shown in Figure 5.2. The comparison in surge shows that the oscillation subjected to second-order forces is closer in magnitude compared to the small wave forces. This might be caused by a difference in stiffness between OpenFast and Simulink at smaller displacements. The OpenFast and Simulink models were matched to each other using decays with an initial condition of 4 meters in surge, very comparable to the magnitude of the oscillation in the strong wave forces, thus providing a better match.

Frequency spectra can provide more insight into the results. These can be found in Figure 5.3 and 5.4. The frequency spectrum is split into 2 distinct regions, from 0 to 0.025 Hz and from 0.025 to 0.25 Hz, to better visualize the results. The contribution of the first-order wave forces is mostly found around the peak period of the generated sea state, i.e., around 0.125 and 0.1 Hz for the weak and strong cases,

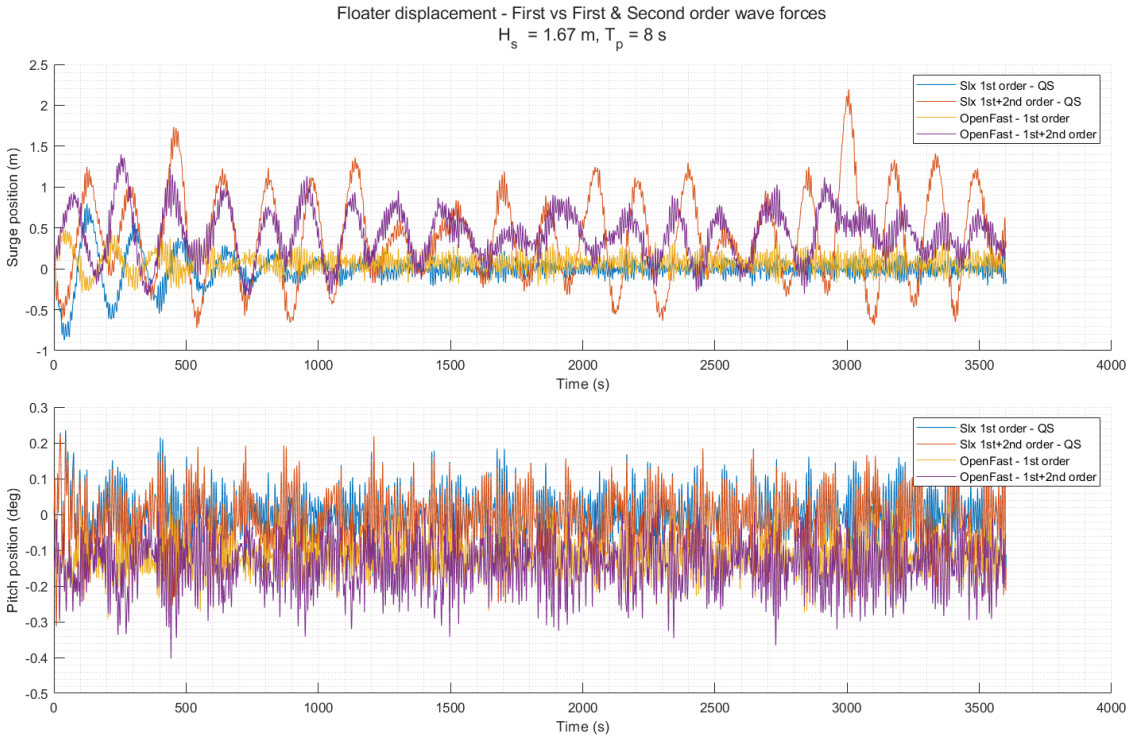

Figure 5.1: Effect of weak first and second order wave forces on floater displacement in Surge and Pitch, comparison between OpenFast and Simulink results.

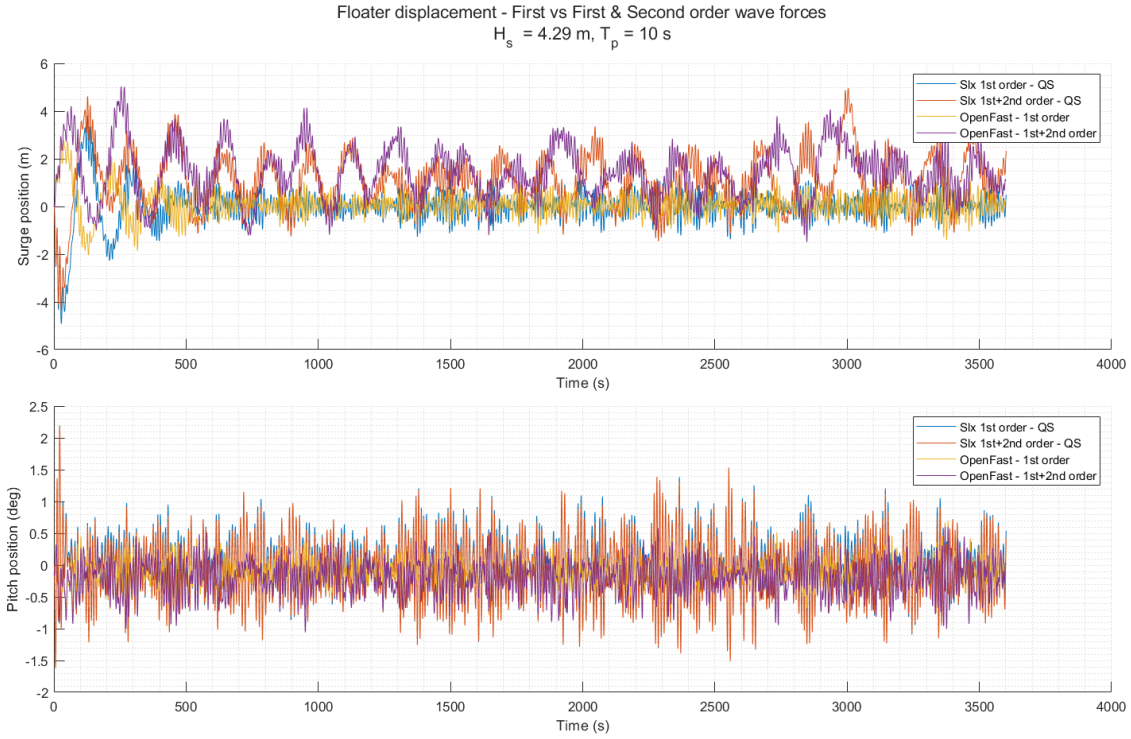

Figure 5.2: Effect of strong first and second order wave forces on floater displacement in Surge and Pitch, comparison between OpenFast and Simulink results.

respectively. The effect of second-order forces can be seen at the natural frequency of the surge and pitch frequency, at approximately 0.006 Hz and 0.04 Hz. In these frequency regions, there is a clear peak in floater displacement caused by the inclusion of second-order forces.

A comparison between the different mooring models is presented in Figure 5.5 and 5.6, for the weak and strong wave forces, respectively. The models show very good agreement in surge and pitch. In terms of magnitude, the dynamic model shows a slightly larger amplitude in surge, while the quasi-static and linear models show slightly larger amplitudes in pitch, but these differences are negligible.

Finally, the mooring force components of the dynamic mooring model in reaction to first, and first- and second-order wave forces are shown in Figure 5.7 and 5.8 respectively. For this case, only the reaction to the strong wave forces is shown for the sake of brevity. The dynamic mooring line model shows very good agreement with OpenFast in terms of mooring force components, though the data is a bit more chaotic, likely caused by the sampling rate of the output data of OpenFast. It can be seen that the mooring line forces are much more variable when the second-order forces are included, caused by the larger oscillation amplitudes of motion of the floater.

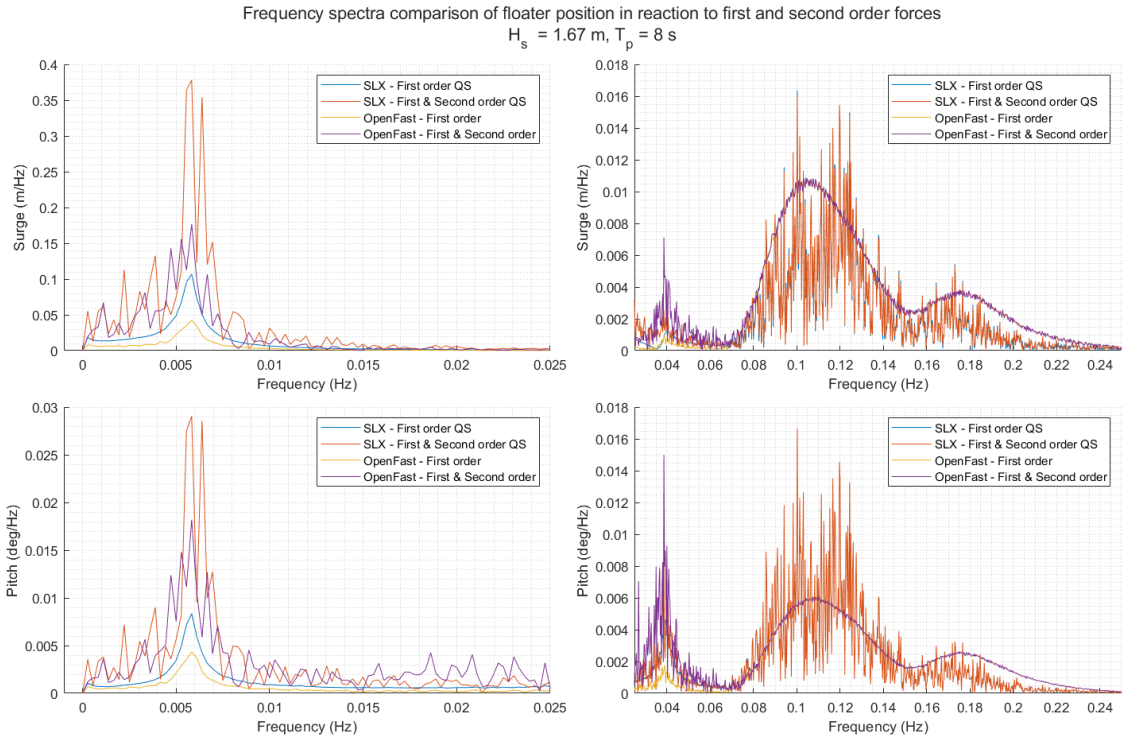

Figure 5.3: Frequency spectra of floater displacement in reaction to weak first- and second-order wave forces.

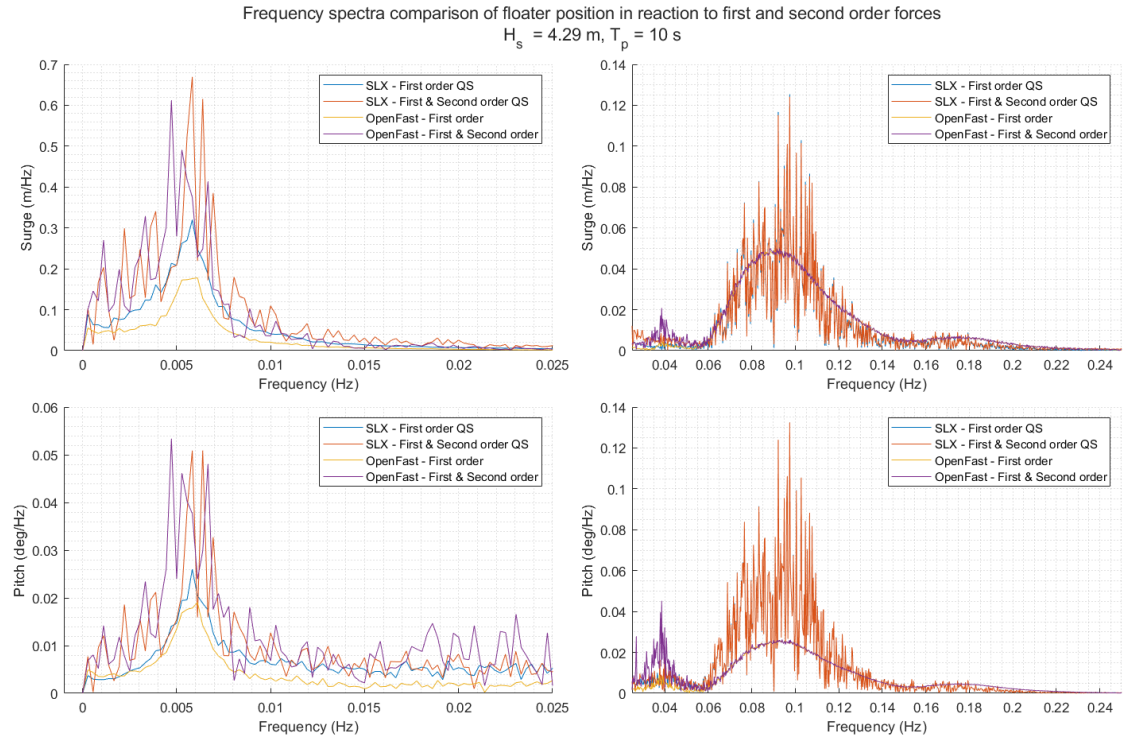

Figure 5.4: Frequency spectra of floater displacement in reaction to strong first- and second-order wave forces.

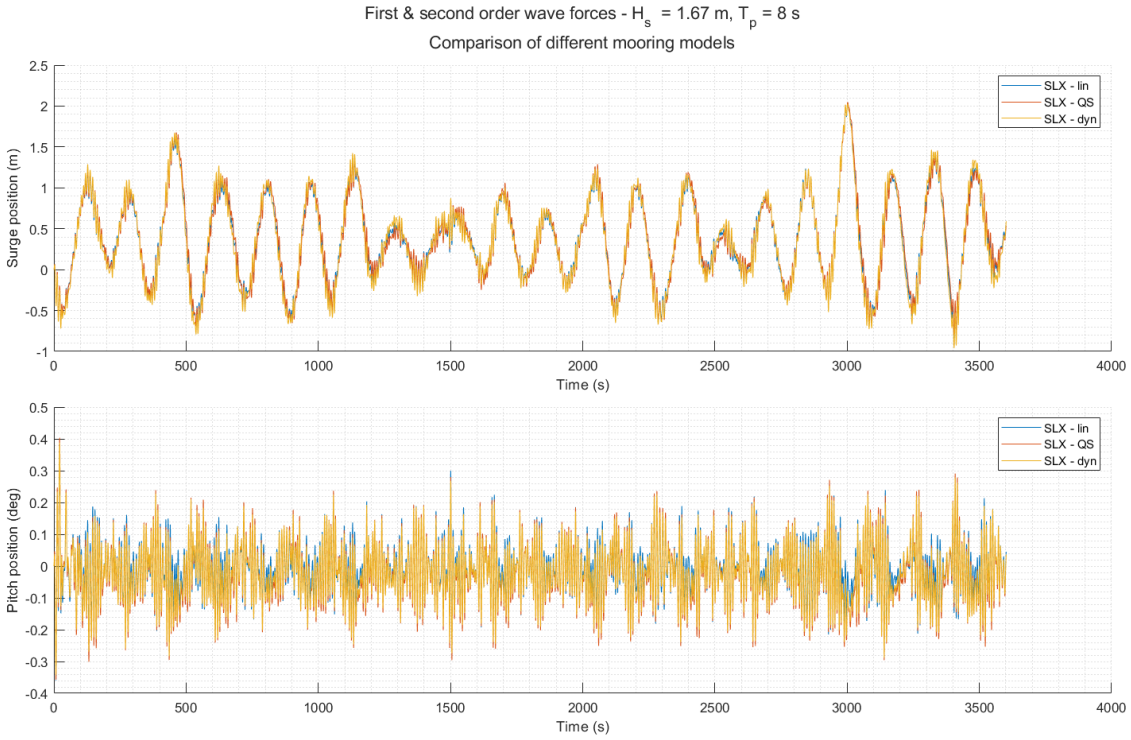

Figure 5.5: Comparison of floater position using the different mooring representations, in reaction to weak first- and second-order wave forces.

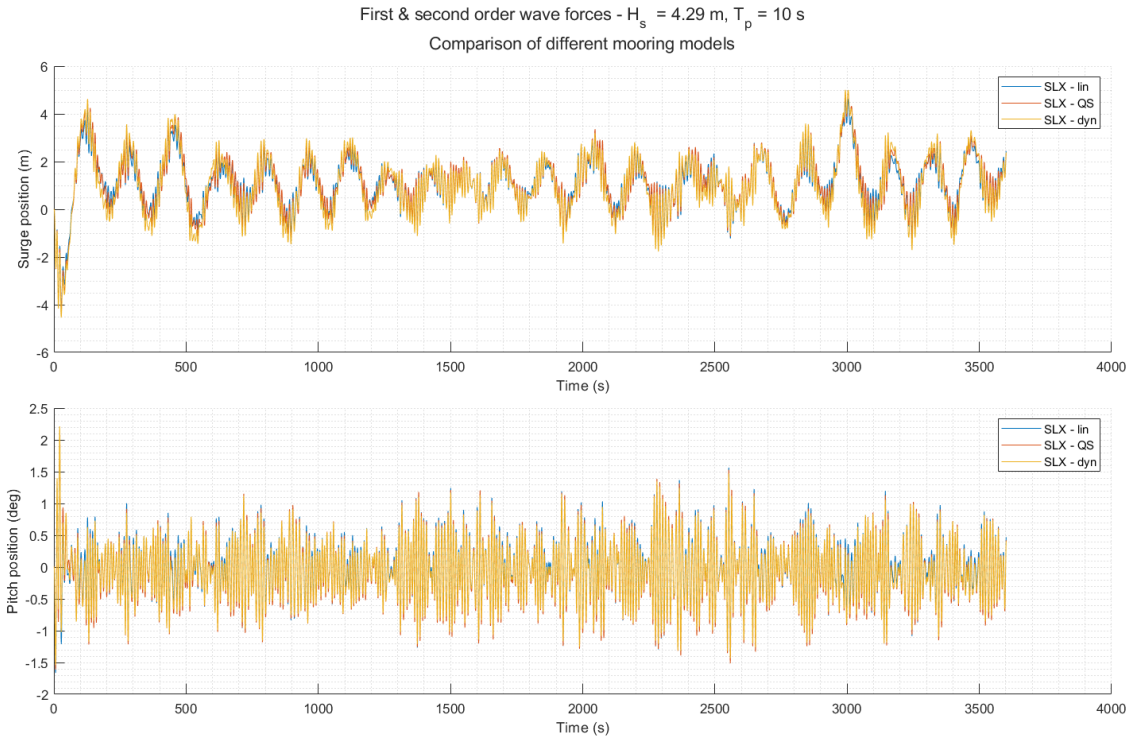

Figure 5.6: Comparison of floater position using the different mooring representations, in reaction to strong first- and second-order wave forces.

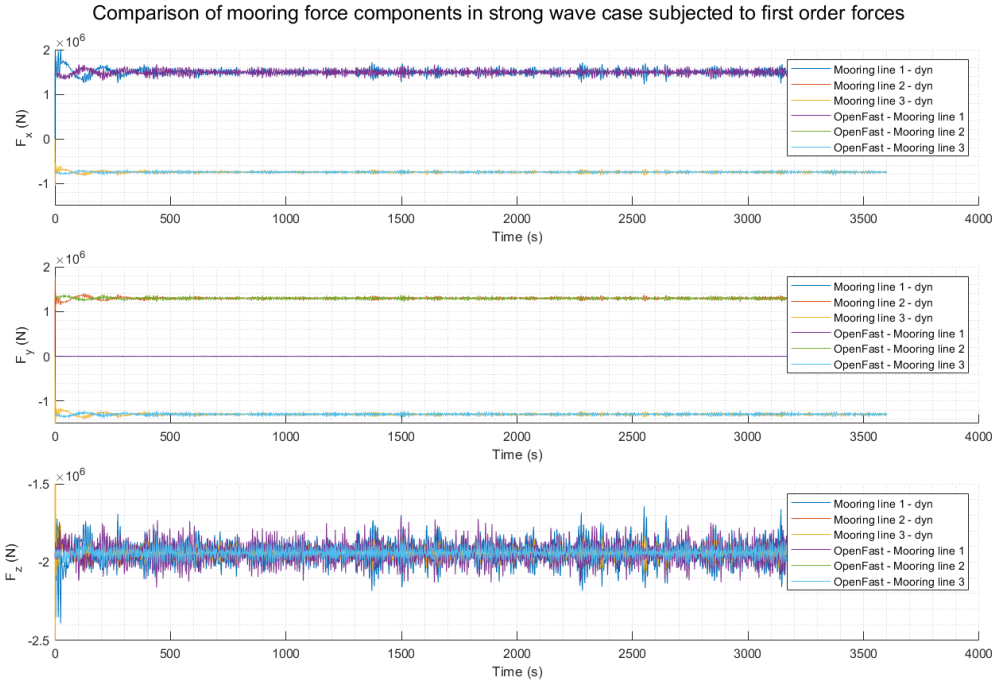

Figure 5.7: Mooring force comparison in x, y, and z components in response to first-order wave forces between OpenFast simulation and Simulink results, using the dynamic mooring model.

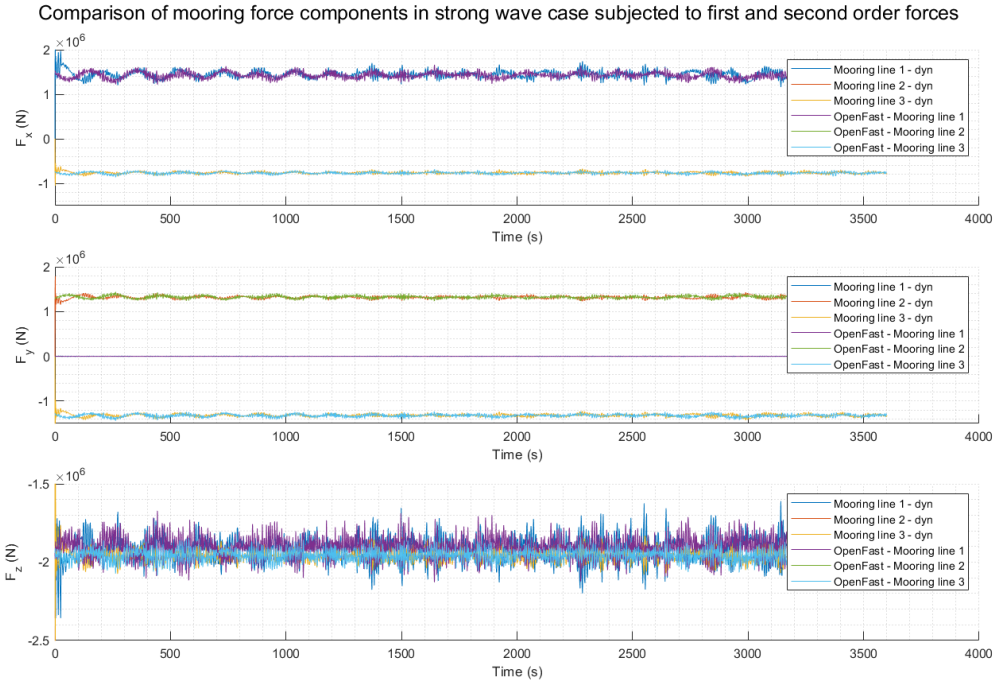

Figure 5.8: Mooring force comparison in x, y, and z components in response to first- and second-order wave forces between OpenFast simulation and Simulink results, using the dynamic mooring model.

5.2. HIL Combined Wind-Wave Cases

The previous section compared the wave action on the floater for first and second order forces, as well as comparing the different mooring line models in a standalone simulation. This section will present the HIL wind tunnel experiment results, where the closed-loop model presented in subsection 4.3.1, is used with wind to measure aerodynamic effects in combined wind-wave cases.

One of the main use cases of HIL wind tunnel tests is to be able to create a representative environment for the analysis of combined wind-wave action. Combined wind-wave cases are presented here for a number of real-world operating conditions to establish the effects of aerodynamic loading on the dynamics of the system.

The effect of wave forces on floater dynamics is examined for both first-order and first- and second-order cases. The severity of the wave cases is determined by their significant wave height and peak period. The wave cases presented here are taken from (Pegalajar-Jurado et al., 2018), and are representative of design load case 1.2. For each of these wave cases also a wind speed is chosen that corresponds to the severity of the wave case, since in real-world conditions, wave severity is related to wind speed. The wave cases 1 through 4 are shown in Table 5.1, where U_{fs} and U_{ms} is the wind speed at full scale and model scale respectively, and $\omega_{r,fs}$ and $\omega_{r,ms}$ is the rotor rotational speed at full scale and model scale respectively.

The waves were generated at a length of 7200 seconds (2 hours) at full scale, which translates to roughly 145 seconds at model scale. The results are saved approximately 15 seconds after applying the wave forces, such that transients of startup effects are gone. Furthermore, the simulation is not run for more than the length of a single wave because the repetition of wave force time histories introduces non-physical effects. As a final note, the wave generation used for these cases uses the same seed for the generation of random angles.

Table 5.1: Wave cases considered in verification of wave forces on floater dynamics.

Case	WC1	WC2	WC3	WC4
H_s (m)	1.67	2.2	3.04	4.29
T_p (s)	8	8	9.5	10
U_{fs} (m/s)	7.11	10.3	11.4	11.4
U_{ms} (m/s)	2.37	3.43	3.8	3.8
$\omega_{r,fs}$ (rpm)	6.04	8.27	9.6	9.6
$\omega_{r,ms}$ (rpm)	298	408	473.6	473.6

The results saved by the simulation are all at model scale, for better reference to the results shown in chapter 3 and chapter 4, the results are scaled up to full scale. The surge and pitch displacement for wave cases 1 & 2 can be seen in Figure 5.9 and for wave cases 3 & 4 in Figure 5.10 in the time domain. The wind causes a mean offset in surge direction, which causes the wind turbine model to drift outside the workspace of the Hexapod at high wind speeds. To combat this effect, a (non-physical) offset in surge is applied during the simulation. In the results shown here, the mean offset in surge is removed.

For analysis, it is easier to look at the results in the frequency domain. The power spectral density is shown in Figure 5.11 for WC 1 & 2 and in Figure 5.12 for WC 3 & 4. The graphs are split into a low-frequency domain and a wave-frequency domain to provide a better visualization of the results. In the low frequency range of Figure 5.11, it can be seen that the inclusion of second-order forces greatly affects the surge and pitch displacement. However, in WC 3 and 4, the second-order forces mainly influence the surge displacement, as the influence of the second-order forces in the pitch degree of freedom in the low frequency range is minimal.

The effect of aerodynamic forces in wave cases is also investigated; the wave cases 1 through were repeated without wind to provide a comparison. To this end, the Cross Power Spectral Density (CPSD) is used. The absolute value of the CPSD of the aerodynamic surge force & surge, and aerodynamic pitching moment & pitch can be seen in Figure 5.13 and Figure 5.14, for wave cases 1 and 4, respectively. Only wave cases 1 and 4 are shown here for the sake of brevity; figures for wave cases 2 and 3, as well as results using the linear mooring model, can be found in Appendix D. The CPSD gives an

indication of the correlation between two signals. I.e., if the signals are correlated, a peak is present in the frequency domain. The magnitude of a peak indicates to what extent. At the wave frequency, the influence of the wind is negligible, as the motion of the floater is dominated by the hydrodynamic loading, which can be seen in the agreement between the wind and no-wind cases.

However, in the low frequency range, the effect of aerodynamic forces can be seen. The results of WC 1 clearly show that the wind cases have significantly higher values for the cross-spectral density in the low frequency range, indicating that the aerodynamic force and moment have a strong influence on the displacement of the floater. The results of WC 4, however, paint a different picture. In the frequency range of 0 - 0.02 Hz, the wind and no-wind cases closely align, indicating little influence due to wind. However, at the 0.02 - 0.05 Hz range, the no-wind cases show a higher peak, indicating that the wind adds a damping effect to the system. The results in WC2 and WC3 show a transition from wind adding energy in the surge and pitch frequency (as in WC1) and subtracting energy from the system, by providing extra damping to the system (as in WC4). These results indicate that the effect of wind in a wave case depends on the considered wave case. In relatively mellow seas, the effect of wind increases the motion of the system in surge and pitch degrees of freedom. In harsher seas, however, the wind acts as a damping factor and reduces the total motion of the floating platform. However, it should be noted that the wind does induce a mean offset from the 0 position, both in surge and pitch.

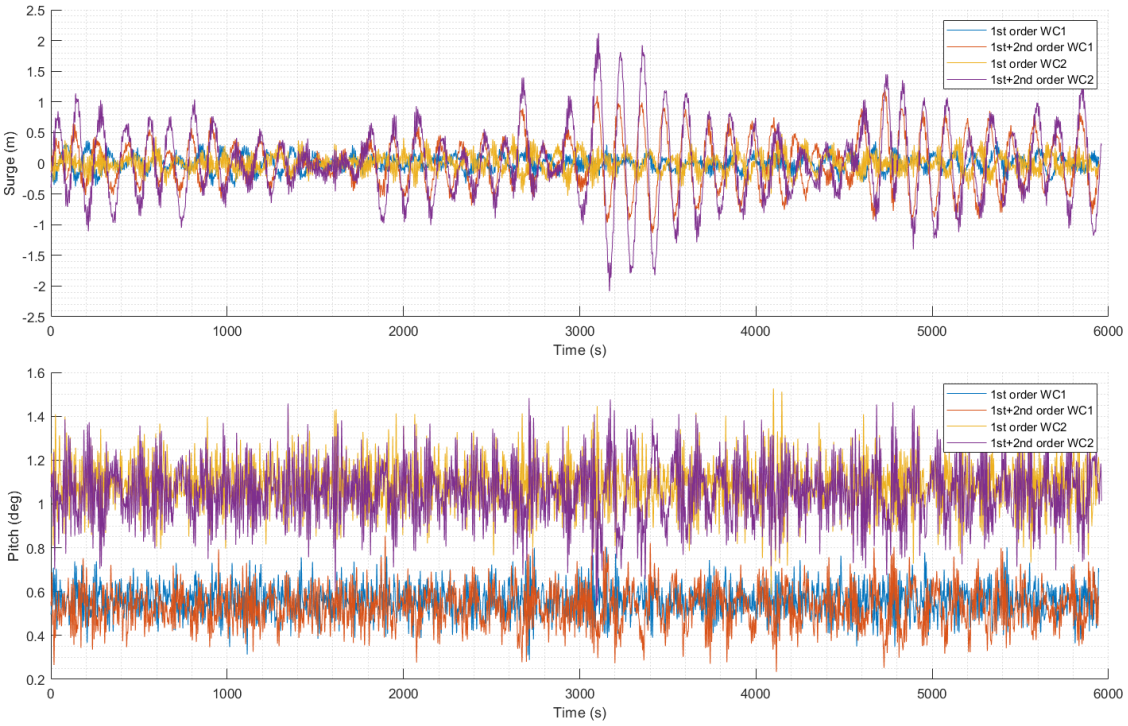

Figure 5.9: Effect of second-order wave excitation forces in terms of the reaction of the floater in surge and pitch, for wave cases 1 and 2.

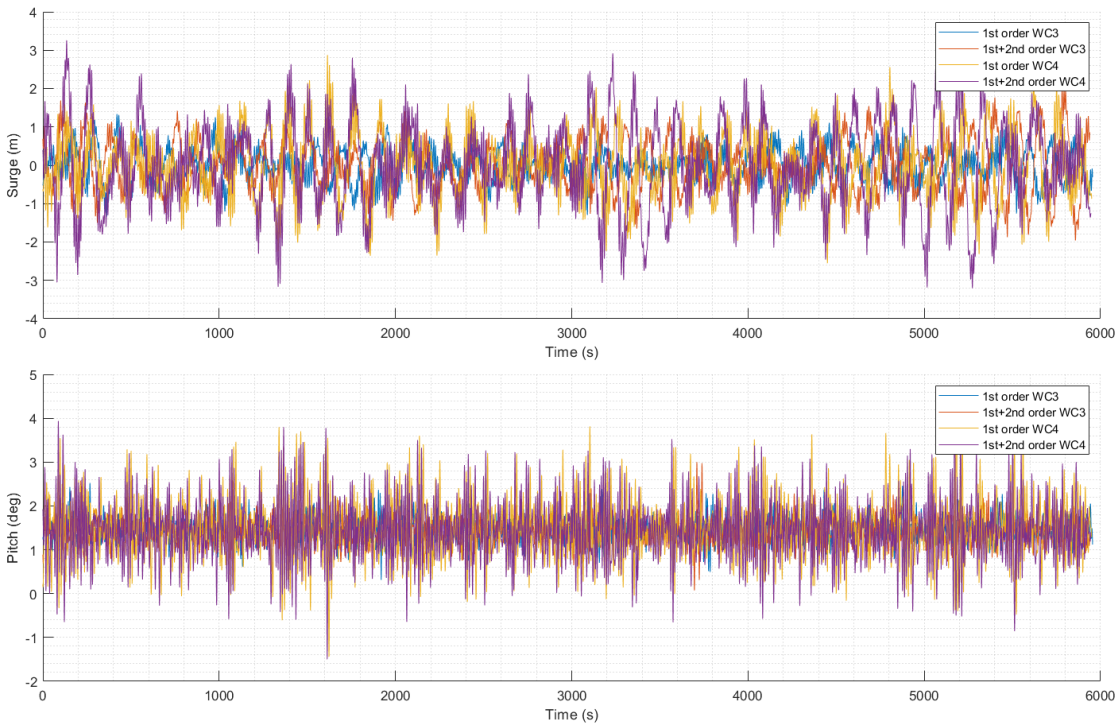

Figure 5.10: Effect of second-order wave excitation forces in terms of the reaction of the floater in surge and pitch, for wave cases 3 and 4.

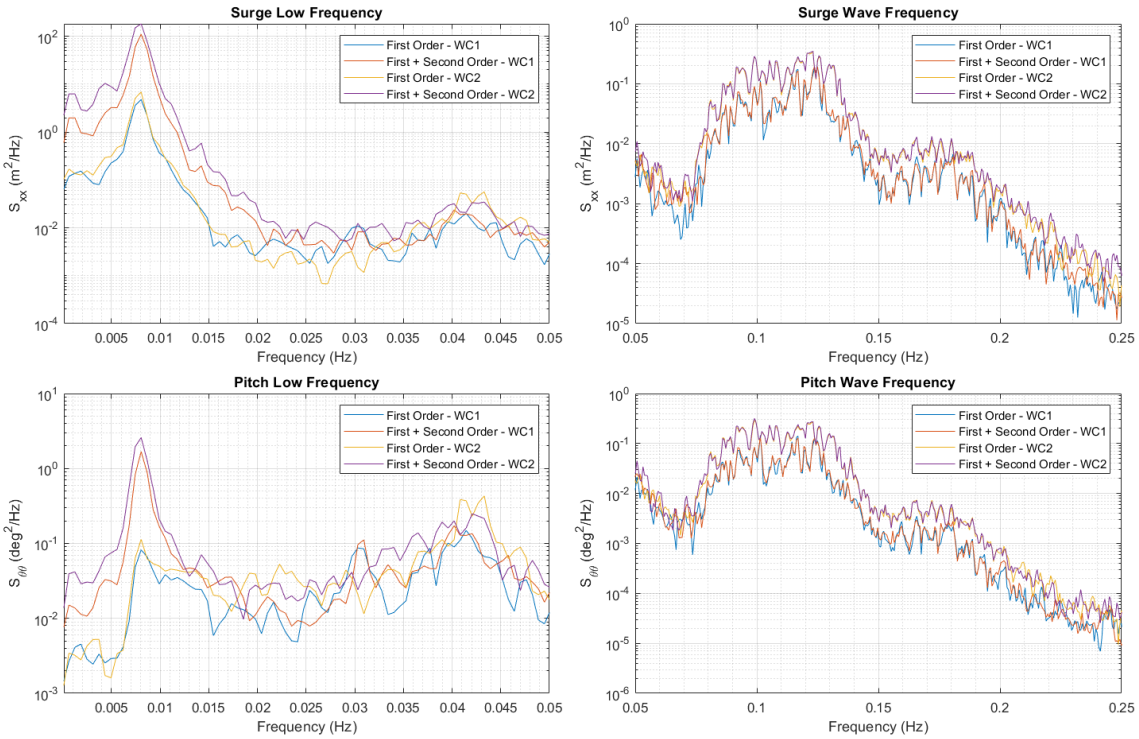

Figure 5.11: Power spectral density of floater position at low frequency and wave frequency, for wave cases 1 and 2.

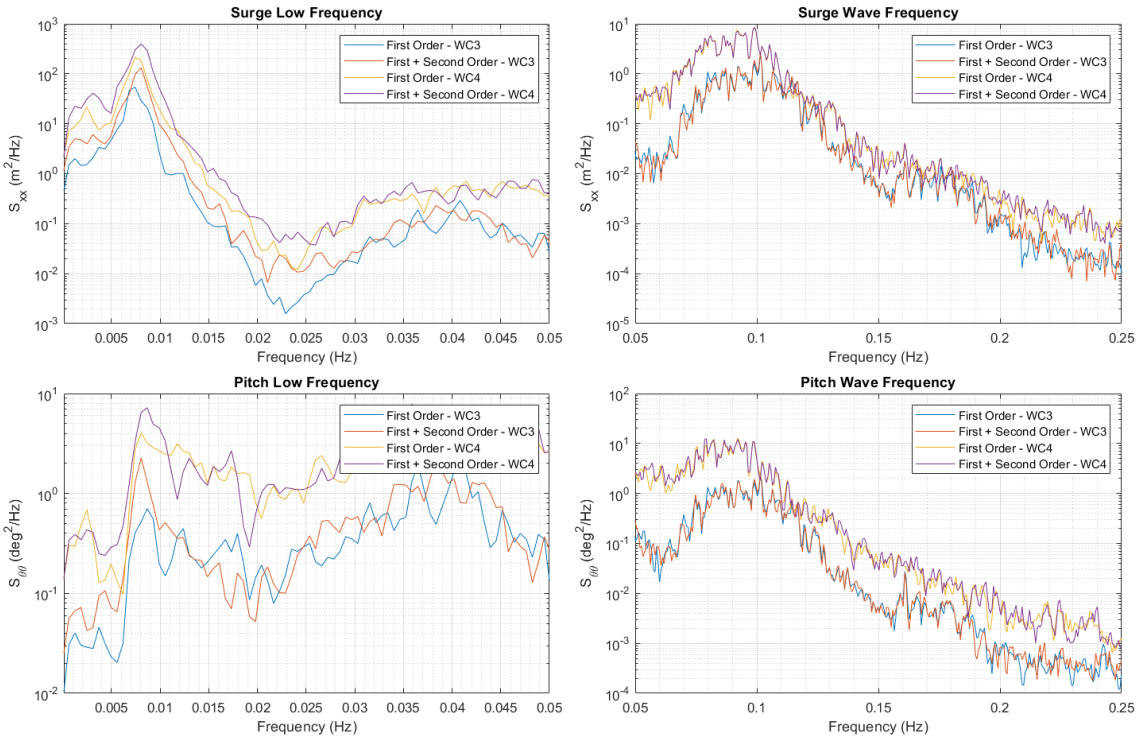

Figure 5.12: Power spectral density of floater position at low frequency and wave frequency, for wave cases 3 and 4.

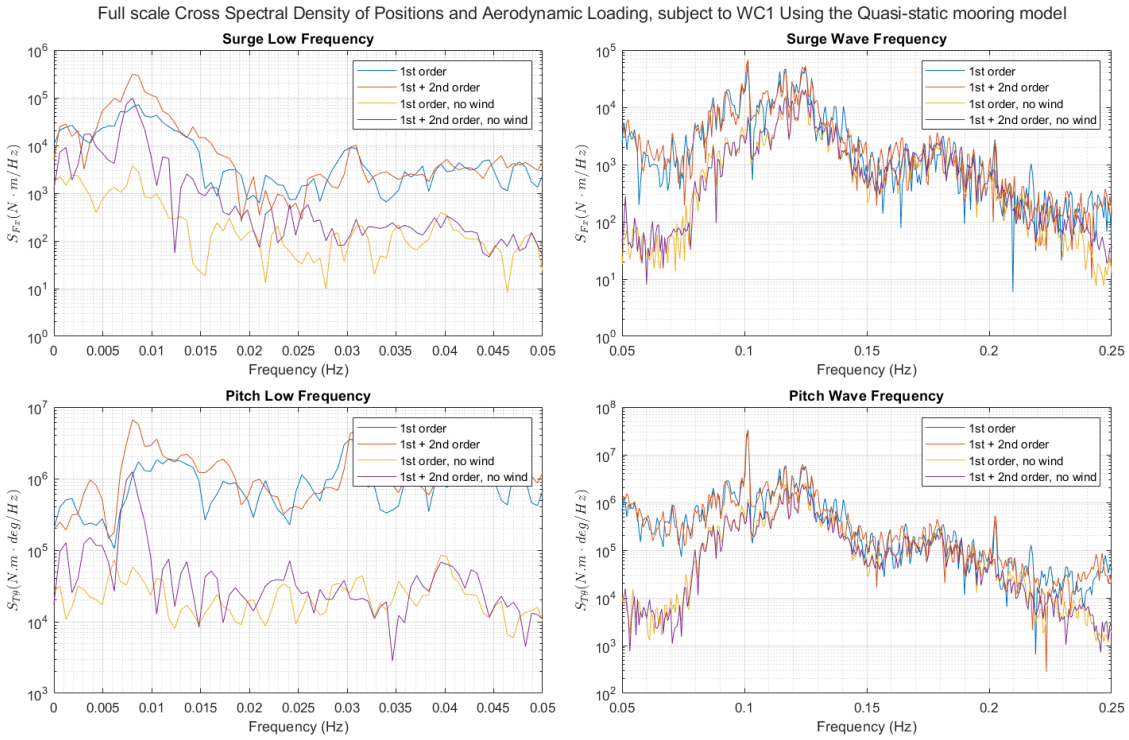

Figure 5.13: Cross Spectral Density of aerodynamic surge force & surge position, and Aerodynamic pitching moment & pitch inclination, subjected to WC1.

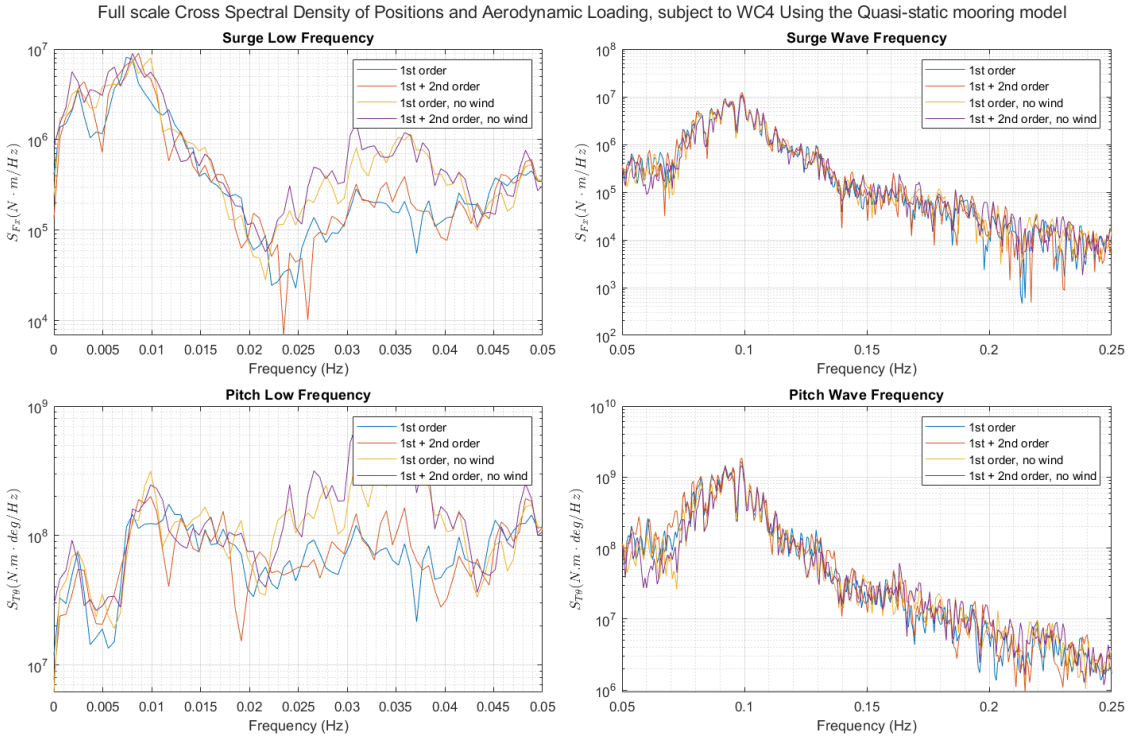

Figure 5.14: Cross Spectral Density of aerodynamic surge force & surge position, and Aerodynamic pitching moment & pitch inclination, subjected to WC4.

5.3. Aerodynamic Damping

Aerodynamic forces affect the natural frequency and damping ratio of the system. Aerodynamic forces have comparatively larger effects on floating wind turbines than their bottom-fixed counterparts, though the magnitude of their effects is found to vary quite substantially (C. Chen & Duffour, 2018). However, few studies have been able to experimentally quantify the effects of aerodynamic damping on the dynamics of floating wind turbines, partly due to difficulties in accurate modeling. HIL experiments such as this study prove invaluable to be able to experimentally test these combined aero- and hydrodynamic effects. There are some limitations to keep in mind; the current setup has limitations in terms of control strategies. The lack of pitch-control or torque-control makes the setup less than ideal for comparison to real-world applications, especially for wind speeds above rated, where pitch or torque control are normally invaluable for limiting aerodynamic forces. The current setup keeps the rotor at a constant speed, which has to be manually set, and is increased linearly with wind speed to maintain constant TSR.

The previous section showed that aerodynamic forces can act as a damping mechanism in certain wind-wave scenarios. This section will aim to quantify the effect of aerodynamic damping on surging, pitching, and yawing motion of floating wind turbines. The effect of aerodynamic damping is analyzed with a multitude of decay tests, with increasing wind speed, to determine the effect of aerodynamic forces on the damping and natural frequency of motion in surge, pitch, and yaw. This study is more of a fundamental study, in that high wind without waves is not quite physical, although other floating aspects are of course still applied (radiation forces, mooring forces). However, this is a good opportunity to isolate the aerodynamic damping effect on a floating wind turbine and analyze the effects. To this end, decay tests will be done using wind speeds of 0 - 5 m/s. It was decided not to go higher than 5 m/s, since at a wind speed of 6 m/s the rotational speed of the rotor would be 720 RPM (i.e. 12 Hz), which would get dangerously close to the natural frequency of the tower at 12.5 Hz. The natural frequency and damping of the motion can be determined in the same way as before, using the Hilbert Transform.

The time domain results for the range of decays in surge, pitch, and yaw can be seen on the left side in Figure 5.15. The color gradient of the results indicates an increase in wind velocity from blue to red. In surge, the effect of an increase in wind speed is not particularly noticeable in the time domain until the motion has almost decayed, at which point the high wind cases show more chaotic motion as a result of the aerodynamic forces. In surge and yaw, however, the effect is more pronounced. Already in the first peaks, there is a noticeable difference between the no-wind and wind cases, with a clear increase in damping as the wind speed increases. This effect is more clearly visible in the frequency domain.

The right side of Figure 5.15 shows the frequency spectra. The surge spectrum does show a slight decrease in the height of the peak at the surge natural frequency. The pitch and yaw spectrum, however, show quite substantial decreases in the peak at their respective frequency. Additionally, the peak in pitch frequency moves slightly to the right on the frequency band, indicating an increase in stiffness in this degree of freedom.

The Hilbert Transform method was used to determine the damping ratio and natural frequencies for each decay. The results are plotted in bar graphs. Figure 5.16 shows the damping ratio in the figures at the top, and the natural frequency of each decay in the bottom figures. The damping ratio of surge, pitch, and yaw is influenced by the wind speed. There are some outliers, however, in general, a trend can be seen in all degrees of freedom, but in surge at 4.5 m/s and in pitch at 4 and 5 m/s, the damping ratio does not quite fit this trend. In pitch at rated wind speed, the damping ratio increases by up to 70%, to 0.13, quite a stark increase. In yawing motion, the effect is even stronger. At rated wind speed, the damping ratio in yawing motion increases by up to 100% to 0.065, and shows an increasing trend at wind speeds above rated.

The natural frequency shown on the lower half of Figure 5.16 confirms what was mentioned before, the natural frequency in surge and yaw is quite constant in relation to wind speed, but pitch shows a slight increase in natural frequency for increasing wind speed, indicating an increase in stiffness in the pitch natural frequency.

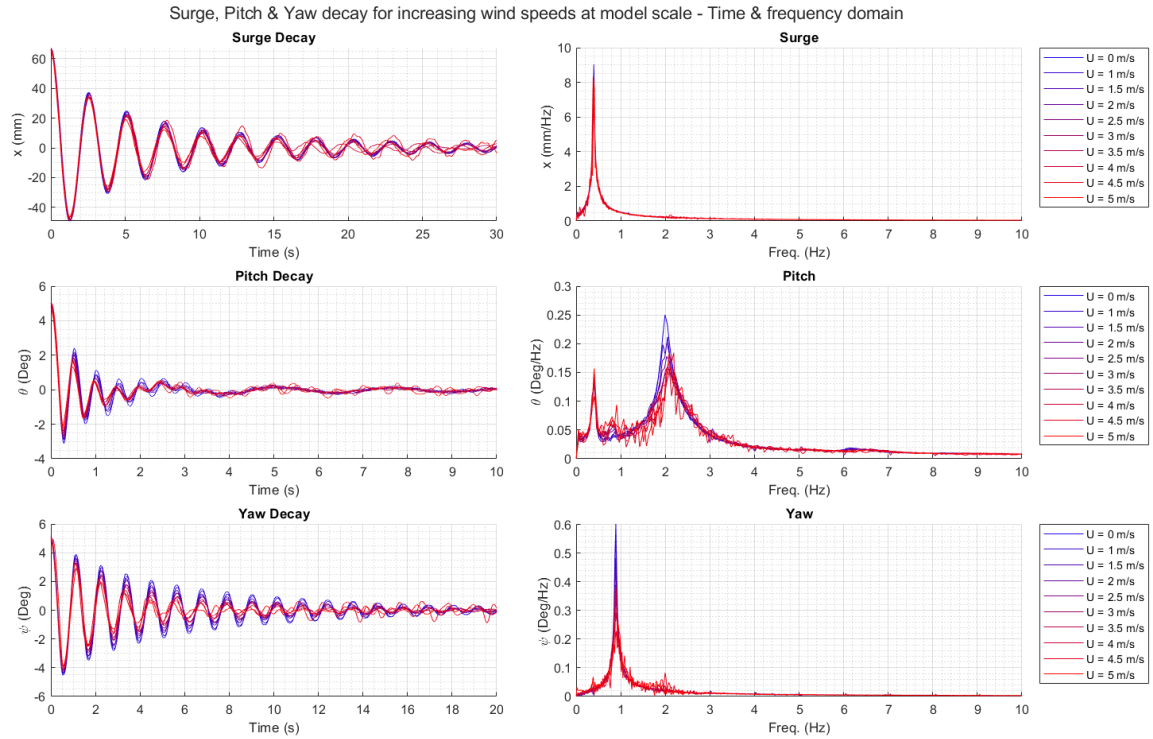

Figure 5.15: Time (left) and frequency (right) domain of the decays in surge, pitch and yaw.

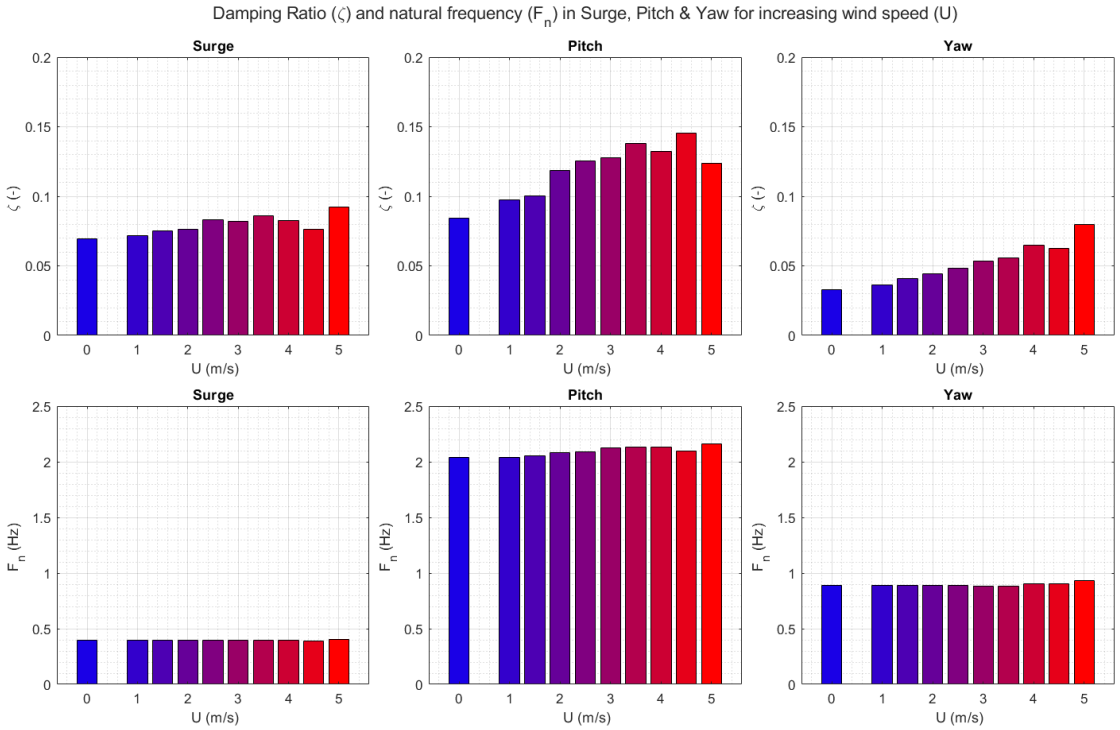

Figure 5.16: Bar graph of damping ratio and natural frequency fo the decays, as a function of inflow wind velocity.

6

Conclusion

The aim of this study was to develop a higher fidelity modeling approach for the TU Delft HIL floating wind turbine system. This was done by implementing higher-order hydrodynamic formulations and the development of a quasi-static and dynamic mooring model. Additionally, the goal was to analyze these systems in wind tunnel experiments.

The research objective was split into separate research questions, the answers to which are imperative to realizing the research goal. This section will conclude the study by answering the research questions and discussing the assumptions and decisions made during the thesis. Finally, some suggestions for future research are proposed.

To what extent do the higher order wave forces affect the dynamic behavior of the FOWT system in a hybrid testing environment?

The second-order difference-frequency wave excitation forces were considered using Newman's approximation. This approximation gives a balance between computational time and accuracy, providing a low-cost alternative to the full quadratic transfer functions required for the full difference-frequency second-order forces. The implementation of the calculation of the second-order forces was verified versus the forces generated by OpenFast, and a good agreement was found. The analysis finds significant increases in floater displacement, in surge and pitch specifically, in wave cases including second-order forces. Besides the increase in oscillation magnitude, there is also a mean drift (or zero-frequency) component causing a mean offset of the zero position. It is therefore recommended to include these contributions in numerical simulations of this kind to accurately model the sea state. It should be noted that the effect of the second-order forces depends on the floater type considered. In this case, for the slack-moored Triple Spar Floater, the second-order difference-frequency wave forces are of importance. However, for taut-moored floater platforms such as TLPs, it is known from literature that the sum-frequency wave excitation forces play a large role.

Does the inclusion of a quasi-static or dynamic mooring line system significantly affect the floater dynamics? Does the increase in fidelity justify the increase in computational cost?

The quasi-static mooring model was implemented using a catenary model, as it is implemented in the Mooring Analysis Programme (MAP++). The dynamic mooring model was implemented as a lumped-mass model, using a similar implementation to the one used in the MoorDyn subroutine of OpenFast. Both models were verified against OpenFast results in decay and wave tests. The models both use MoorDyn input files as input to generate the mooring representation in Simulink. The Hilbert Transform method was used to match the natural frequencies and damping of the Simulink results to the OpenFast results. The mooring tension components at the fairlead show that the Simulink implementation of the dynamic mooring line model shows great agreement with the dynamic model used in the MoorDyn subroutine of OpenFast. The quasi-static model fairlead tensions are approximately 10% higher in magnitude than the OpenFast results, but give acceptable results.

The quasi-static mooring model, however, produces these results at a much larger time step than the

dynamic mooring model. The quasi-static model was able to produce these results at a time step of 0.025 seconds at model-scale, while the dynamic model required a minimum time step of 5e-5 seconds to reach a stable simulation. This also made it impossible to use the dynamic model in the HIL wind tunnel tests, as the real-time simulation machine was not able to simulate in real-time at this small of a time step. It can be concluded that the dynamic mooring representation is not a viable approach in this particular HIL setup, at least not in its current form. There are possibilities, though, to make it possible to run a dynamic model, but revisions are necessary, either in the numerical modeling approach or in the physical setup.

Nevertheless, the quasi-static model performed well in the HIL tests. The current setup allows for determining fairlead and anchor reaction forces, giving more information about the mooring system than in the previous setup. Furthermore, this setup allows for rapid testing of different types of mooring configurations, requiring only an input file in the format of a MoorDyn input file, though some revisions might be required for the testing of more complicated mooring line setups such as interconnected lines or net configurations, which might require to be solved using a dynamic approach.

What is the effect of aerodynamic forces on the damping & natural frequency of a FOWT, in a hybrid testing environment?

The Hardware-in-the-Loop system was tested in the OJF wind tunnel to analyze the effects of aerodynamic damping on the floating wind turbine in surging, pitching, and yawing motion. Decay tests were executed in these degrees of freedom for a range of wind speeds. The results show a slight increase in the damping ratio in surge, with an increase in the damping ratio of 50% at rated wind speed in pitching motion, and almost doubling the damping ratio at rated wind speed in yawing motion. The aerodynamic damping did not significantly increase the natural frequency of the surging and yawing motion; the pitching decay did see a slight increase in natural frequency, suggesting that the aerodynamic damping could increase the natural frequency of the pitching motion by up to 10% at rated wind speed.

In wave cases, it was found that the aerodynamic force has an aggravating effect in relatively mellow sea states, increasing oscillation magnitude in surge and pitch. However, as the harshness of sea states increases, the effect of aerodynamic forces starts to work as a damping mechanism, reducing the observed oscillation magnitude. In this research, it was only tested how this affects sea states with wind speeds up to the rated wind speed; however, for pitch-controlled wind turbines, the aerodynamic thrust force decreases after the rated wind speed, which means that this trend might be reversed above rated, but as of now the current set-up is not able to analyze this accurately, as no pitch control is currently present.

Suggestions for future work

Due to limitations in time and available resources, not every aspect has been modeled as accurately as it could have been. Additionally, some wind tunnel test cases have been omitted due to time constraints in the wind tunnel. Some suggestions are presented here that could be taken into account in future studies.

- The dynamic mooring model was not able to run at the required time step for real-time simulation; future works could look into improving the computational efficiency of the dynamic model, for instance by employing a similar strategy as done by (Bayati et al., 2018), where they don't take into account all force contributions for certain line sections, which reduces computational load.
- Add compatibility for more complex mooring line setups, like net formations or interconnected lines. However, this might require a dynamic mooring line representation. For real-time simulation, this problem would have to be solved first.
- The second-order difference-frequency wave excitation forces were included in terms of Newman's approximation; future studies could look into the difference between using this approximation and using the full difference-frequency quadratic transfer function.
- Study the effects of wind-wave misalignment and multidirectional waves. Multidirectional waves require data from the floater in all directions. For the TripleSpar floater, at the time of this study,

only wave forces from 180 and 0 degrees heading were available, which was not dense enough to provide a good interpolation of data for the other directions.

- The force correction methodology currently measures the forces only in the 3 translational degrees of freedom and calculates the torques in the rotational degrees of freedom based on these. Measuring the torques directly could improve the methodology by reducing inaccuracies, thus creating a more robust force correction.
- Previous research has looked into adapting the current modeling approach to a 15 MW wind turbine reference turbine. It was not possible at the time due to a multitude of circumstances, but if more resources could be dedicated to these problems, this might be solved.
- The current wind turbine model has no control system, and the motor is set to a fixed speed. Various levels of control could be added to improve the functionality of the wind turbine and better represent real turbines. This could be done in terms of pitch control (collective or individual). This would allow for the accurate testing of operational wind speeds between rated and cut-out speeds, where some control measure is typically required for reducing aerodynamic forcing on the rotor.

Bibliography

Ambrosini, S., Bayati, I., Facchinetti, A., & Belloli, M. (2020). Methodological and technical aspects of a two-degrees-of-freedom hardware-in-the-loop setup for wind tunnel tests of floating systems. *Journal of Dynamic Systems, Measurement, and Control*, *142*, 061002.

Arapogianni, A., Genachte, A.-B., Ochagavia, R. M., Castell, J. P. V. D., Korbijn, A. R. T. J., Huera-Huarte, N. C. B. F. J., Schuon, F., de Laleu, A. U. J. S. V., Tunbjer, J. M. A., Roth, R., Azau, S., Bourgeois, S., Casey, Z., Moccia, J., Radvilaite, V., Scola, J., & Wilkes, J. (2013). *Deep water the next step for offshore wind energy*. www.ewea.org/report/deep-water

Bachynski, E., Kvittem, M., Luan, C., & Moan, T. (2014). Wind-wave misalignment effects on floating wind turbines: Motions and tower load effects. *Journal of Offshore Mechanics and Arctic Engineering*, *136*(4), 041902.

Bachynski, E., Thys, M., Sauder, T., Chabaud, V., & Sæther, L. (2016). Real-time hybrid model testing of a braceless semi-submersible wind turbine: Part ii—experimental results. *International Conference on Offshore Mechanics and Arctic Engineering*, *49972*, V006T09A040.

Bacic, M. (2005). On hardware-in-the-loop simulation. *Proceedings of the 44th IEEE Conference on Decision and Control*, 3194–3198.

Bak, C., Zahle, F., Bitsche, R., Kim, T., Yde, A., Henriksen, L. C., Natarajan, A., & Hansen, M. (2013). Description of the dtu 10 mw reference wind turbine. *DTU Wind Energy Report-I-0092*, *5*.

Barj, L., Jonkman, J., Robertson, A., Stewart, G., Lackner, M., Haid, L., Matha, D., & Stewart, S. (2014). Wind/wave misalignment in the loads analysis of a floating offshore wind turbine. *32nd ASME wind energy symposium*, 0363.

Barooni, M., Ashuri, T., Velioglu Sogut, D., Wood, S., & Ghaderpour Taleghani, S. (2022). Floating offshore wind turbines: Current status and future prospects. *Energies*, *16*(1), 2.

Bauduin, C., & Naciri, M. (2000). A contribution on quasi-static mooring line damping. *J. Offshore Mech. Arct. Eng.*, *122*(2), 125–133.

Bayati, I., Belloli, M., Facchinetti, A., & Giappino, S. (2013). Wind tunnel tests on floating offshore wind turbines: A proposal for hardware-in-the-loop approach to validate numerical codes. *Wind Engineering*, *37*(6), 557–568.

Bayati, I., Facchinetti, A., Fontanella, A., & Belloli, M. (2018). 6-dof hydrodynamic modelling for wind tunnel hybrid/hil tests of fowt: The real-time challenge. *International Conference on Offshore Mechanics and Arctic Engineering*, *51319*, V010T09A078.

Bayati, I., Jonkman, J., Robertson, A., & Platt, A. (2014). The effects of second-order hydrodynamics on a semisubmersible floating offshore wind turbine. *Journal of Physics: Conference Series*, *524*(1), 012094.

Belloli, M., Bayati, I., Facchinetti, A., Fontanella, A., Giberti, H., La Mura, F., Taruffi, F., & Zasso, A. (2020). A hybrid methodology for wind tunnel testing of floating offshore wind turbines. *Ocean Engineering*, *210*, 107592.

Borg, M., Collu, M., & Kolios, A. (2014). Offshore floating vertical axis wind turbines, dynamics modelling state of the art. part ii: Mooring line and structural dynamics. *Renewable and Sustainable Energy Reviews*, *39*, 1226–1234.

Brodtkorb, P. A., Johannesson, P., Lindgren, G., Rychlik, I., Rydén, J., & Sjö, E. (2000). Wafo-a matlab toolbox for analysis of random waves and loads. *ISOPE International Ocean and Polar Engineering Conference*, ISOPE–I.

Butterfield, S., Musial, W., Jonkman, J., & Sclavounos, P. (2007). *Engineering challenges for floating offshore wind turbines* (tech. rep.). National Renewable Energy Lab.(NREL), Golden, CO (United States).

Carmo, L., de Mello, P., Monaro, R., Mas-Soler, J., Simos, A., & e Silva, D. F. d. C. (2024). Numerical modeling of wave basin experiments of a floating wind turbine with active thrust emulation: A discussion of important aspects. *Ocean Engineering*, *309*, 1–20.

Chen, C., & Duffour, P. (2018). Modelling damping sources in monopile-supported offshore wind turbines. *Wind Energy*, *21*(11), 1121–1140. https://doi.org/https://doi.org/10.1002/we.2218

Chen, J., & Hu, Z. (2018). Experimental investigation of aerodynamic effect–induced dynamic characteristics of an oc4 semi-submersible floating wind turbine. *Proceedings of the Institution of Mechanical Engineers, Part M: Journal of Engineering for the Maritime Environment*, *232*(1), 19–36.

Collina, A., Facchinetti, A., Fossati, F., & Resta, F. (2004). Hardware in the loop test-rig for identification and control application on high speed pantographs. *Shock and Vibration*, *11*(3-4), 445–456.

Cummins, W. (1962). The impulse response function and ship motion. *Report 1661, Department of the Navy, David W. Taylor Model Basin, Hydromechanics Laboratory, Research and Development Report, October 1962*.

de Ridder, E., Otto, W., Zondervan, G., Huijs, F., & Vaz, G. (2014). Development of a scaled-down floating wind turbine for offshore basin testing. *33rd International Conference on Offshore Mechanics and Arctic Engineering*, 1–11.

Du, W., Zhao, Y., He, Y., & Liu, Y. (2016). Design, analysis and test of a model turbine blade for a wave basin test of floating wind turbines. *Renewable Energy*, *97*, 414–421.

Duarte, T., Gueydon, S., Jonkman, J., & Sarmento, A. (2014). Computation of wave loads under multidirectional sea states for floating offshore wind turbines. *International conference on offshore mechanics and arctic engineering*, *45547*, V09BT09A023.

Duarte, T., Sarmento, A., Alves, M., & Jonkman, J. (2013). *State-space realization of the wave-radiation force within fast* (tech. rep.). National Renewable Energy Lab.(NREL), Golden, CO (United States).

Duarte, T. M., Sarmento, A. J., & Jonkman, J. M. (2014). Effects of second-order hydrodynamic forces on floating offshore wind turbines. *32nd ASME Wind Energy Symposium*, 0361.

Edrington, C., Steurer, M., Langston, J., El-Mezyani, T., & Schoder, K. (2015). Role of power hardware in the loop in modeling and simulation for experimentation in power and energy systems. *Proceedings of the IEEE*, *103*(12), 2401–2409.

Facchinetti, A., & Mauri, M. (2009). Hardware-in-the-loop overhead line emulator for active pantograph testing. *IEEE Transactions on Industrial Electronics*, *56*(10), 4071–4078.

Fleischer, C., Sauer, D., Barreras, J., Schaltz, E., & Christensen, A. (2016). Development of software and strategies for battery management system testing on hil simulator. *2016 Eleventh International Conference on Ecological Vehicles and Renewable Energies (EVER)*, 1–12.

Fontanella, A., Facchinetti, A., Daka, E., & Belloli, M. (2023). Modeling the coupled aero-hydro-servo-dynamic response of 15 mw floating wind turbines with wind tunnel hardware in the loop. *Renewable Energy*, *219*, 119442.

Fontanella, A., Liu, Y., Azcona, J., Pires, O., Bayati, I., Gueydon, S., De Ridder, E., Van Wingerden, J., & Belloli, M. (2020). A hardware-in-the-loop wave-basin scale-model experiment for the validation of control strategies for floating offshore wind turbines. *Journal of Physics: Conference Series*, *1618*, 032038.

Fontanella, A., Da Pra, G., & Belloli, M. (2023). Integrated design and experimental validation of a fixed-pitch rotor for wind tunnel testing. *Energies*, *16*(5), 2205.

Fowler, M., Kimball, R., Thomas III, D., & Goupee, A. (2013). Design and testing of scale model wind turbines for use in wind/wave basin model tests of floating offshore wind turbines. *32nd International conference on offshore mechanics and arctic engineering*, 1–11.

Giberti, H., & Ferrari, D. (2015). A novel hardware-in-the-loop device for floating offshore wind turbines and sailing boats. *Mechanism and Machine Theory*, *85*, 82–105.

Gil, J., Tur, M., Gregori, S., Correcher, A., Pedrosa, A. M., & Fuenmayor, F. J. (2024). Hardware-in-the-loop simulations of a railway pantograph with a finite element periodic catenary model. *Vehicle System Dynamics*, *62*(3), 695–718.

Hall, M., & Goupee, A. (2015). Validation of a lumped-mass mooring line model with deepcwind semisubmersible model test data. *Ocean Engineering*, *104*, 590–603.

Hall, M., Goupee, A., & Jonkman, J. (2018). Development of performance specifications for hybrid modeling of floating wind turbines in wave basin tests. *Journal of Ocean Engineering and Marine Energy*, *4*, 1–23.

Hasselmann, K., Barnett, T., Bouws, E., Carlson, H., Cartwright, D., Enke, K., Ewing, J., Gienapp, A., Hasselmann, D., Kruseman, P., et al. (1973). Measurements of wind-wave growth and swell

decay during the joint north sea wave project (jonswap). *Ergaenzungsheft zur Deutschen Hydrographischen Zeitschrift, Reihe A*.

Henderson, A. R., & Witcher, D. (2010). Floating offshore wind energy—a review of the current status and an assessment of the prospects. *Wind Engineering*, *34*(1), 1–16.

Hmedi, M., Uzunoglu, E., Zeng, C., Gaspar, J., & Guedes Soares, C. (2023). Experimental challenges and modelling approaches of floating wind turbines. *Journal of Marine Science and Engineering*, *11*(11), 2048.

Isermann, R., Schaffnit, J., & Sinsel, S. (1999). Hardware-in-the-loop simulation for the design and testing of engine-control systems. *Control Engineering Practice*, *7*(5), 643–653.

Jensen, J. J. (2001). *Load and global response of ships* (Vol. 4). Elsevier.

Jonkman, B., Platt, A., Mudafort, R. M., Branlard, E., Sprague, M., Ross, H., Slaughter, D., jjonkman, HaymanConsulting, cortadocodes, Hall, M., Vijayakumar, G., Buhl, M., Russell9798, Bortolotti, P., RyanDavies19, reos-rcrozier, Ananthan, S., S., M., … Wang, L. (2024, October). *Openfast/openfast: V3.5.4* (Version v3.5.4). Zenodo. https://doi.org/10.5281/zenodo.14010255

Karimirad, M. (2013). Modeling aspects of a floating wind turbine for coupled wave–wind-induced dynamic analyses. *Renewable Energy*, *53*, 299–305.

Kaven, L., Frehn, A., Basler, M., Jassmann, U., Röttgers, H., Konrad, T., Abel, D., & Monti, A. (2022). Impact of multi-physics hil test benches on wind turbine certification. *Energies*, *15*(4), 1336.

Lauss, G. F., Faruque, M. O., Schoder, K., Dufour, C., Viehweider, A., & Langston, J. (2015). Characteristics and design of power hardware-in-the-loop simulations for electrical power systems. *IEEE Transactions on Industrial Electronics*, *63*(1), 406–417.

Lee, C. (1995). *Wamit theory manual*. Massachusettes Institute of Technology Department of Ocean Engineering.

Lee, K., Hwang, D., Lee, S., Kim, Y., et al. (2004). Development of antilock braking controller using hardware in-the-loop simulation and field test. *30th Annual Conference of IEEE Industrial Electronics Society, 2004. IECON 2004*, *3*, 2137–2141.

Lemmer, F., Raach, S., Schlipf, D., Faerron-Guzmán, R., & Cheng, P. W. (2020). *FAST model of the SWE-TripleSpar floating wind turbine platform for the DTU 10MW reference wind turbine*. https://doi.org/10.18419/darus-514

Li, H., & Bachynski-Polić, E. (2021). Validation and application of nonlinear hydrodynamics from cfd in an engineering model of a semi-submersible floating wind turbine. *Marine Structures*, *79*, 103054.

Limpaecher, E., Salcedo, R., Corbett, E., Manson, S., Nayak, B., & Allen, W. (2017). Lessons learned from hardware-in-the-loop testing of microgrid control systems. *Grid of the Future Symposium*.

Lin, P. (2008). *Numerical modeling of water waves*. CRC Press.

Liu, F., Chen, J., & Qin, H. (2017). Frequency response estimation of floating structures by representation of retardation functions with complex exponentials. *Marine Structures*, *54*, 144–166.

Liu, Y., Xiao, Q., Incecik, A., Peyrard, C., & Wan, D. (2017). Establishing a fully coupled cfd analysis tool for floating offshore wind turbines. *Renewable Energy*, *112*, 280–301.

Lu, H., Chang, S., Chen, C., Fan, T., & Chen, J. (2022). Replacement of force-to-motion relationship with state–space model for dynamic response analysis of floating offshore structures. *Applied Ocean Research*, *119*, 102977.

Manolas, D., Karvelas, C., Kapogiannis, I., Riziotis, V., Spiliopoulos, K., & Voutsinas, S. (2018). A comprehensive method for the structural design and verification of the innwind 10mw tri-spar floater. *Journal of Physics: Conference Series*, *1104*(1), 012025.

Martin, H., Kimball, R., Viselli, A., & Goupee, A. (2014). Methodology for wind/wave basin testing of floating offshore wind turbines. *Journal of Offshore Mechanics and Arctic Engineering*, *136*.

Masciola, M., Jonkman, J., & Robertson, A. (2014). Extending the capabilities of the mooring analysis program: A survey of dynamic mooring line theories for integration into fast. *International Conference on Offshore Mechanics and Arctic Engineering*.

Masciola, M., Jonkman, J., & Robertson, A. (2013). Implementation of a multisegmented, quasi-static cable model. *ISOPE International Ocean and Polar Engineering Conference*, ISOPE–I.

Matha, D., Schlipf, M., Pereira, R., & Jonkman, J. (2011). Challenges in simulation of aerodynamics, hydrodynamics, and mooring-line dynamics of floating offshore wind turbines. *ISOPE International Ocean and Polar Engineering Conference*, ISOPE–I.

Meng, Q., Hua, X., Chen, C., Zhou, S., Liu, F., & Chen, Z. (2022). Analytical study on the aerodynamic and hydrodynamic damping of the platform in an operating spar-type floating offshore wind turbine. *Renewable Energy*, *198*, 772–788.

Moskowitz, L. (1964). Estimates of the power spectrums for fully developed seas for wind speeds of 20 to 40 knots. *Journal of geophysical research*, *69*(24), 5161–5179.

Nauri, I., Ihwanudin, M., Mindarta, E., Harly, M., Putra, A., Awanggapati, B., Ismail, H., et al. (2020). Development of integrated hardware-in-the-loop (hil) test bench anti-lock brake system (abs) instrument. *Journal of Physics: Conference Series*, *1700*, 012097.

Ogilvie, T. (1964). Recent progress toward the understanding and prediction of ship motions. *Proc. of the 5th Symposium on Navan Hydrodynamics, Bergen, Norway*, 3–79.

Otter, A., Murphy, J., Pakrashi, V., Robertson, A., & Desmond, C. (2022). A review of modelling techniques for floating offshore wind turbines. *Wind Energy*, *25*(5), 831–857.

Pegalajar-Jurado, A., Bredmose, H., Borg, M., Straume, J. G., Landbø, T., Andersen, H. S., Yu, W., Müller, K., & Lemmer, F. (2018). State-of-the-art model for the lifes50+ oo-star wind floater semi 10mw floating wind turbine. *Journal of Physics: Conference Series*, *1104*(1), 012024.

Petersheim, M. D., & Brennan, S. N. (2009). Scaling of hybrid-electric vehicle powertrain components for hardware-in-the-loop simulation. *Mechatronics*, *19*, 1078–1090.

Philippe, M., Babarit, A., & Ferrant, P. (2013). Modes of response of an offshore wind turbine with directional wind and waves. *Renewable energy*, *49*, 151–155.

Pugi, L., Paolieri, G., Giorgetti, M., Berzi, L., Viviani, R., Cabrucci, L., & Bocciolini, L. (2023). Hil testing of wheel slide protection systems: Criteria for continuous updating and validation. *Railway Engineering Science*, *31 (2)*, 108–121.

Puleva, T., Rouzhekov, G., Slavov, T., & Rakov, B. (2016). Hardware in the loop (hil) simulation of wind turbine power control. *Mediterranean Conference on Power Generation, Transmission, Distribution and Energy Conversion (MedPower 2016)*, 1–8.

Sauder, T., Chabaud, V., Thys, M., Bachynski, E., & Sæther, L. (2016). Real-time hybrid model testing of a braceless semi-submersible wind turbine: Part i—the hybrid approach. *International conference on offshore mechanics and arctic engineering*, *49972*, V006T09A039.

SBM Offshore. (2021). Sbm tlp floater concept [Online; accessed July 2nd, 2025]. https://www.empireengineering.co.uk/wp-content/uploads/2021/08/SBM-Offshore-wind-floater-scaled-e1630067766590.jpg

Sharma, J., & Dean, R. (1981). Second-order directional seas and associated wave forces. *Society of Petroleum Engineers Journal*, *21*(01), 129–140.

Suh, M., Seok, C., Kim, Y., Chung, J., Kim, S., Lee, J., & Lee, S. (1998). Hardware-in-the-loop simulation for abs. *SAE transactions*, 483–489.

Taghipour, R., Perez, T., & Moan, T. (2008). Hybrid frequency–time domain models for dynamic response analysis of marine structures. *Ocean Engineering*, *35*(7), 685–705.

Taruffi, F., Novais, F., & Viré, A. (2024). An experimental study on the aerodynamic loads of a floating offshore wind turbine under imposed motions. *Wind Energ. Sci.*, *9*, 343–35. https://doi.org/10.5194/wes-9-343-2024

Thinakaran, S. (2024). *Numerical modeling of dynamics of a fowt - for hardware-in-loop testing in wind tunnels* [Master's thesis, Delft University of Technology].

The open jet facility [online; accessed April 4th, 2025]. (2025). https://www.tudelft.nl/lr/organisatie/afdelingen/flow-physics-and-technology/facilities/low-speed-wind-tunnels/open-jet-facility

Verma, R., Del Vecchio, D., & Fathy, H. K. (2008). Longitudinal vehicle dynamics scaling and implementation on a hil setup. *Dynamic Systems and Control Conference*, 979–986.

Wang, C., Utsunomiya, T., Wee, S., & Choo, Y. (2010). Research on floating wind turbines: A literature survey. *The IES Journal Part A: Civil & Structural Engineering*, *3*(4), 267–277.

Wang, H. (2022). Taut mooring. In *Encyclopedia of ocean engineering* (pp. 1933–1937). Springer.

Wang, J., Song, Y., Li, W., Guo, J., & Monti, A. (2014). Development of a universal platform for hardware in-the-loop testing of microgrids. *IEEE Transactions on Industrial Informatics*, *10*(4), 2154–2165.

Yang, C., Chen, P., Cheng, Z., Xiao, L., Chen, J., & Liu, L. (2023). Aerodynamic damping of a semi-submersible floating wind turbine: An analytical, numerical and experimental study. *Ocean Engineering*, *281*, 114826.

Young, I. (2017, April). Regular, irregular waves and the wave spectrum. Encyclopedia of Maritime; Offshore Engineering. https://doi.org/10.1002/9781118476406.emoe078

Zhang, W., Calderon-Sanchez, J., Duque, D., & Souto-Iglesias, A. (2024). Computational fluid dynamics (cfd) applications in floating offshore wind turbine (fowt) dynamics: A review. *Applied Ocean Research*, *150*, 104075.

Zhong, W., Zhao, W., Wan, D., & Zhao, Y. (2024). Comparison study on mooring line models for hydrodynamic performances of floating offshore wind turbines. *Ocean Engineering*, *296*, 117083.

A

Additional Stiffness & Damping Matrices

The matrices presented here contain coefficients in the 6 DOFs of the system. The matrices contain only diagonal entries. These entries are, in order of first row to last: surge, sway, heave, roll, pitch and yaw. The units of these coefficients are for stiffness (K) N/m in translational DOF, and N/rad in rotational DOF respectively. For $D^{(1)}$ and $D^{(2)}$, the units in translational and rotational DOF are: $N.s/m$, $N.s/rad$ and $N.s^2/m^2$, $N.s^2/rad^2$, respectively.

Linear Mooring

$$K = \begin{pmatrix} -9.5e3 & 0 & 0 & 0 & 0 & 0 \\ 0 & -9.5e3 & 0 & 0 & 0 & 0 \\ 0 & 0 & -5.8e5 & 0 & 0 & 0 \\ 0 & 0 & 0 & 2.2e9 & 0 & 0 \\ 0 & 0 & 0 & 0 & 2.3e9 & 0 \\ 0 & 0 & 0 & 0 & 0 & -1.8e7 \end{pmatrix} \quad \text{(A.1a)}$$

$$D^{(1)} = \begin{pmatrix} -2.0e4 & 0 & 0 & 0 & 0 & 0 \\ 0 & -2.0e4 & 0 & 0 & 0 & 0 \\ 0 & 0 & 6.0e5 & 0 & 0 & 0 \\ 0 & 0 & 0 & 1.6e9 & 0 & 0 \\ 0 & 0 & 0 & 0 & 1.4e9 & 0 \\ 0 & 0 & 0 & 0 & 0 & 3.0e7 \end{pmatrix} \quad \text{(A.1b)}$$

$$D^{(2)} = \begin{pmatrix} 1.4e6 & 0 & 0 & 0 & 0 & 0 \\ 0 & 1.4e6 & 0 & 0 & 0 & 0 \\ 0 & 0 & 4.3e7 & 0 & 0 & 0 \\ 0 & 0 & 0 & 2.0e11 & 0 & 0 \\ 0 & 0 & 0 & 0 & 2.0e11 & 0 \\ 0 & 0 & 0 & 0 & 0 & 3.2e10 \end{pmatrix} \quad \text{(A.1c)}$$

Quasi-static Mooring

$$K = \begin{pmatrix} -1.6e4 & 0 & 0 & 0 & 0 & 0 \\ 0 & -1.6e4 & 0 & 0 & 0 & 0 \\ 0 & 0 & -6.5e5 & 0 & 0 & 0 \\ 0 & 0 & 0 & 2.0e9 & 0 & 0 \\ 0 & 0 & 0 & 0 & 2.3e9 & 0 \\ 0 & 0 & 0 & 0 & 0 & -4.0e7 \end{pmatrix} \quad \text{(A.2a)}$$

$$D^{(1)} = \begin{pmatrix} 0 & 0 & 0 & 0 & 0 & 0 \\ 0 & 0 & 0 & 0 & 0 & 0 \\ 0 & 0 & 6.0e5 & 0 & 0 & 0 \\ 0 & 0 & 0 & 1.2e9 & 0 & 0 \\ 0 & 0 & 0 & 0 & 1.2e9 & 0 \\ 0 & 0 & 0 & 0 & 0 & 2.8e7 \end{pmatrix} \quad \text{(A.2b)}$$

$$D^{(2)} = \begin{pmatrix} 1.0e6 & 0 & 0 & 0 & 0 & 0 \\ 0 & 1.0e6 & 0 & 0 & 0 & 0 \\ 0 & 0 & 4.0e6 & 0 & 0 & 0 \\ 0 & 0 & 0 & 4.0e11 & 0 & 0 \\ 0 & 0 & 0 & 0 & 4.0e11 & 0 \\ 0 & 0 & 0 & 0 & 0 & 3.0e10 \end{pmatrix} \quad \text{(A.2c)}$$

Dynamic Mooring

$$K = \begin{pmatrix} -2.5e3 & 0 & 0 & 0 & 0 & 0 \\ 0 & -2.5e3 & 0 & 0 & 0 & 0 \\ 0 & 0 & -4.4e5 & 0 & 0 & 0 \\ 0 & 0 & 0 & 2.1e9 & 0 & 0 \\ 0 & 0 & 0 & 0 & 2.3e9 & 0 \\ 0 & 0 & 0 & 0 & 0 & -1.5e7 \end{pmatrix} \quad \text{(A.3a)}$$

$$D^{(1)} = \begin{pmatrix} 0 & 0 & 0 & 0 & 0 & 0 \\ 0 & 0 & 0 & 0 & 0 & 0 \\ 0 & 0 & 1.2e5 & 0 & 0 & 0 \\ 0 & 0 & 0 & 8.3e8 & 0 & 0 \\ 0 & 0 & 0 & 0 & 1.2e9 & 0 \\ 0 & 0 & 0 & 0 & 0 & 3.4e6 \end{pmatrix} \quad \text{(A.3b)}$$

$$D^{(2)} = \begin{pmatrix} 5.0e5 & 0 & 0 & 0 & 0 & 0 \\ 0 & 4.5e5 & 0 & 0 & 0 & 0 \\ 0 & 0 & 1.2e12 & 0 & 0 & 0 \\ 0 & 0 & 0 & 2e11 & 0 & 0 \\ 0 & 0 & 0 & 0 & 8.5e10 & 0 \\ 0 & 0 & 0 & 0 & 0 & 5.0e8 \end{pmatrix} \quad \text{(A.3c)}$$

B

Mooring Tension Figures

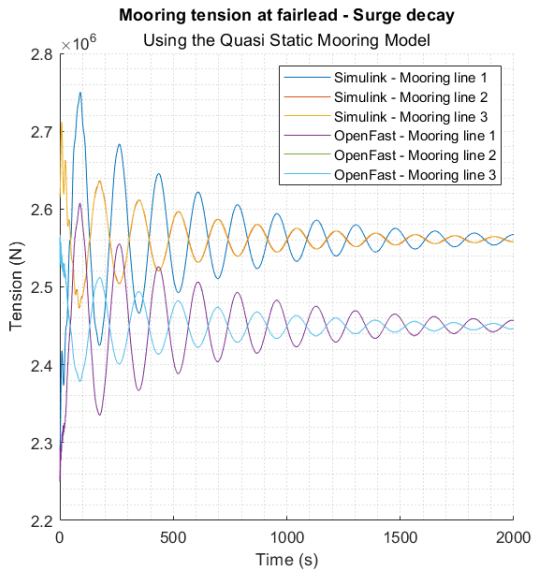

(a) Surge decay

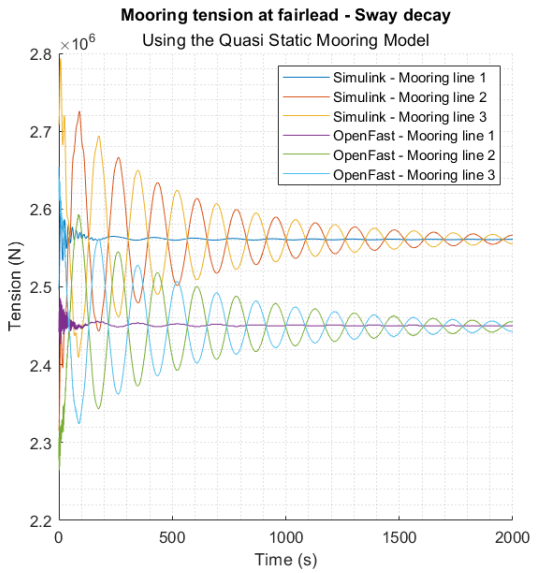

(b) Sway decay

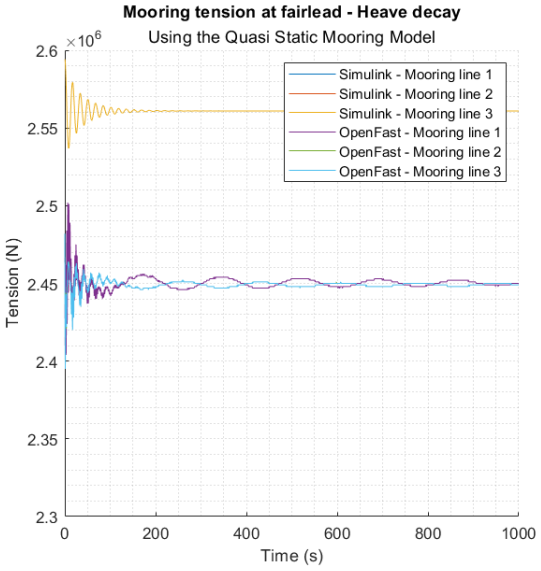

(c) Heave decay

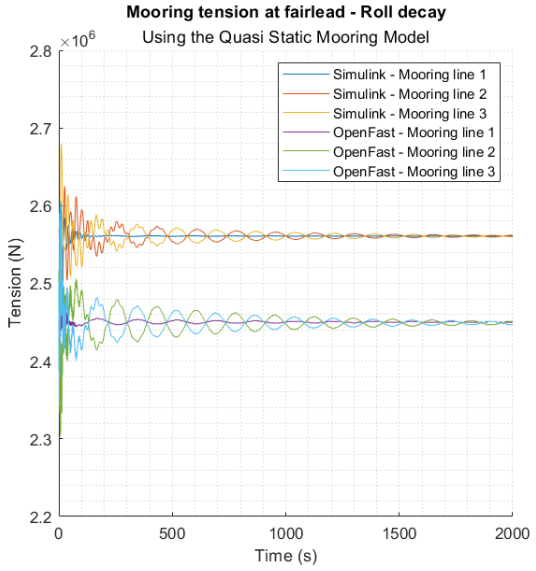

(d) Roll decay

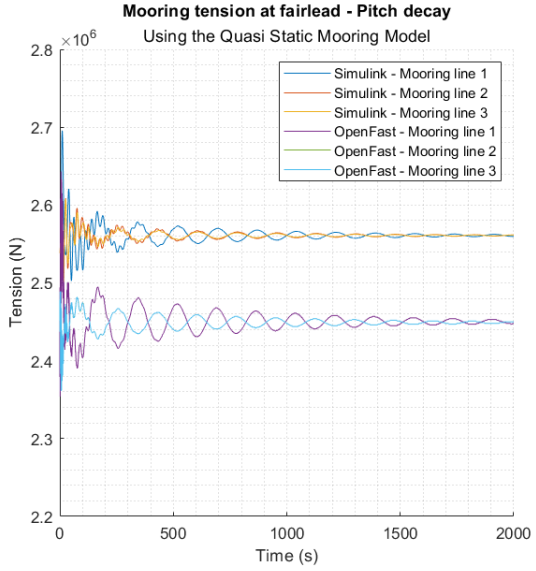

(e) Pitch decay

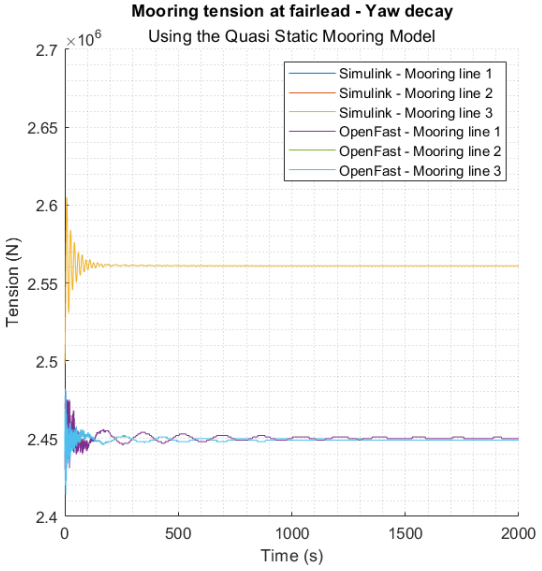

(f) Yaw decay

Figure B.1: Mooring tension at the fairleads in all DOFs, using the quasi-static mooring model.

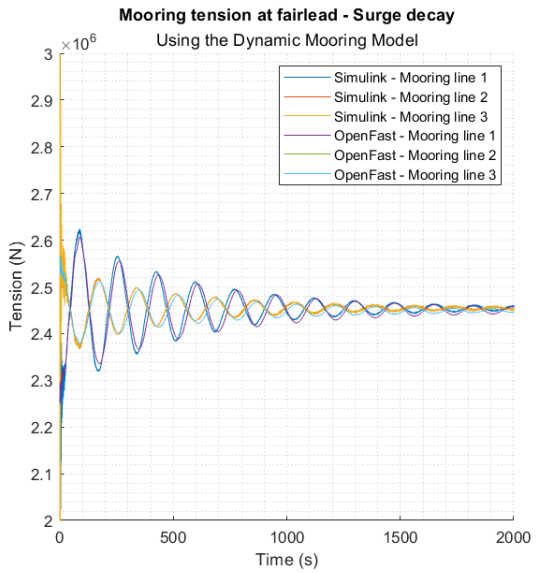

(a) Surge decay

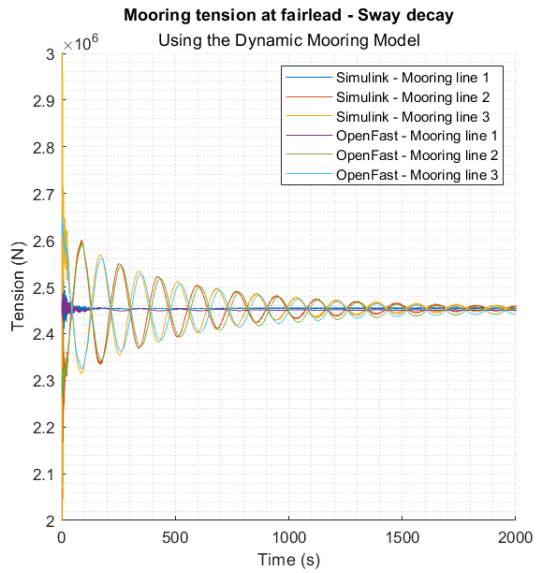

(b) Sway decay

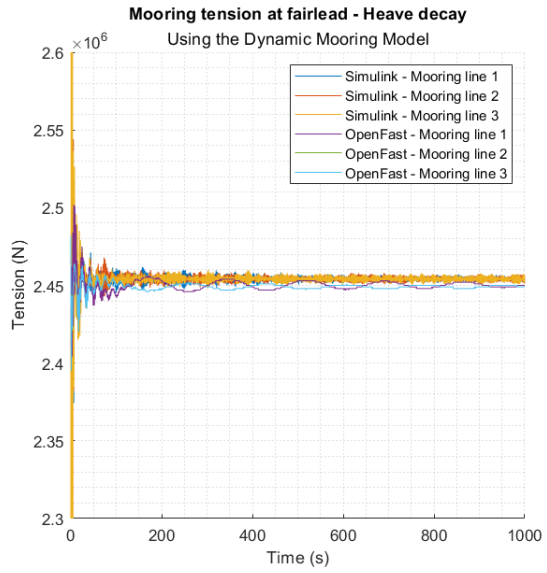

(c) Heave decay

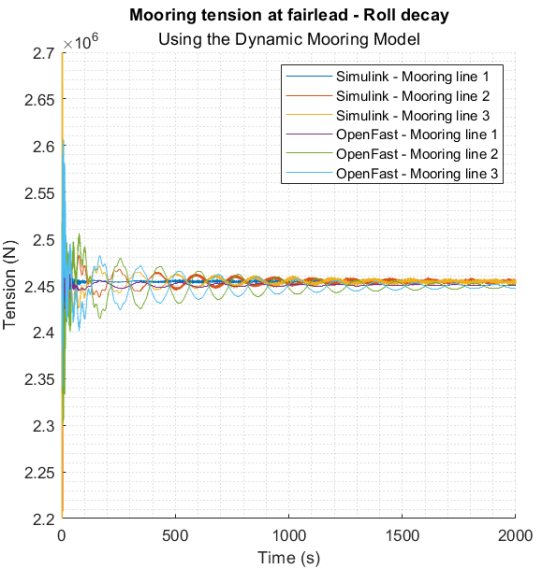

(d) Roll decay

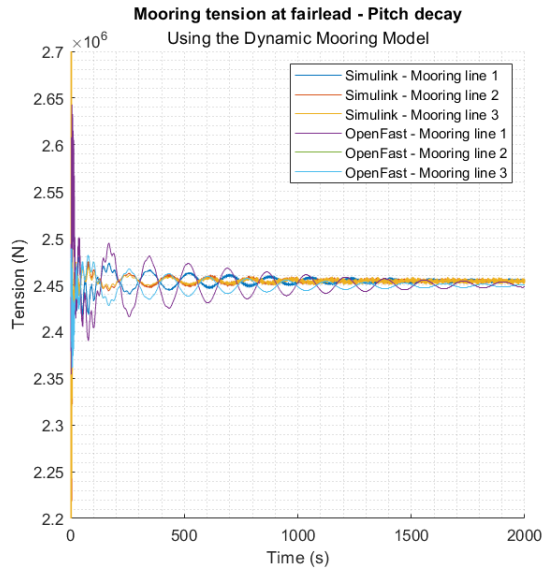

(e) Pitch decay

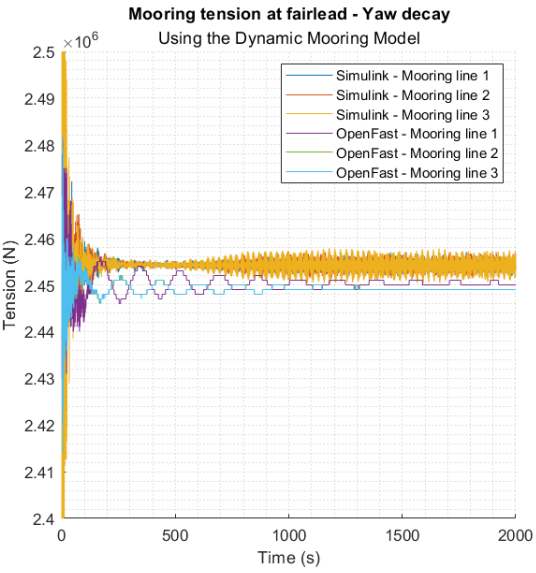

(f) Yaw decay

Figure B.2: Mooring tension at the fairleads in all DOFs, using the dynamic mooring model.

C

OL vs CL figures

Table C.1: Decay stats of HIL decay tests, open-loop vs closed-loop, using the linear mooring model.

IC	IC1				IC2			
	open-loop		closed-loop		open-loop		closed-loop	
	ζ	F_n	ζ	F_n	ζ	F_n	ζ	F_n
Surge	0.039	0.395	0.039	0.393	0.054	0.396	0.055	0.394
Sway	0.037	0.407	0.038	0.393	0.053	0.395	0.055	0.394
Heave	0.085	2.989	0.086	2.992	0.121	3.083	0.118	3.094
Roll	0.068	1.938	0.069	1.989	0.103	1.963	0.100	2.003
Pitch	0.060	2.029	0.065	2.010	0.089	2.062	0.093	2.034
Yaw	0.018	0.907	0.024	0.887	0.025	0.909	0.029	0.887

Table C.2: Percentage wise difference between open-loop and closed-loop decay results, using the linear mooring model.

IC	IC1				IC2			
	open-loop		closed-loop		open-loop		closed-loop	
	ζ	F_n	ζ	F_n	ζ	F_n	ζ	F_n
Surge	-	-	-0.4%	-0.5%	-	-	+1.0%	-0.6%
Sway	-	-	+2.1%	-3.5%	-	-	+3.1%	-0.4%
Heave	-	-	+1.0%	+0.1%	-	-	-1.8%	+0.3%
Roll	-	-	+1.4%	+2.6%	-	-	-3.4%	+2.0%
Pitch	-	-	+8.2%	-1.0%	-	-	+5.1%	-1.3%
Yaw	-	-	+34.3%	-2.2%	-	-	+16.7%	-2.4%

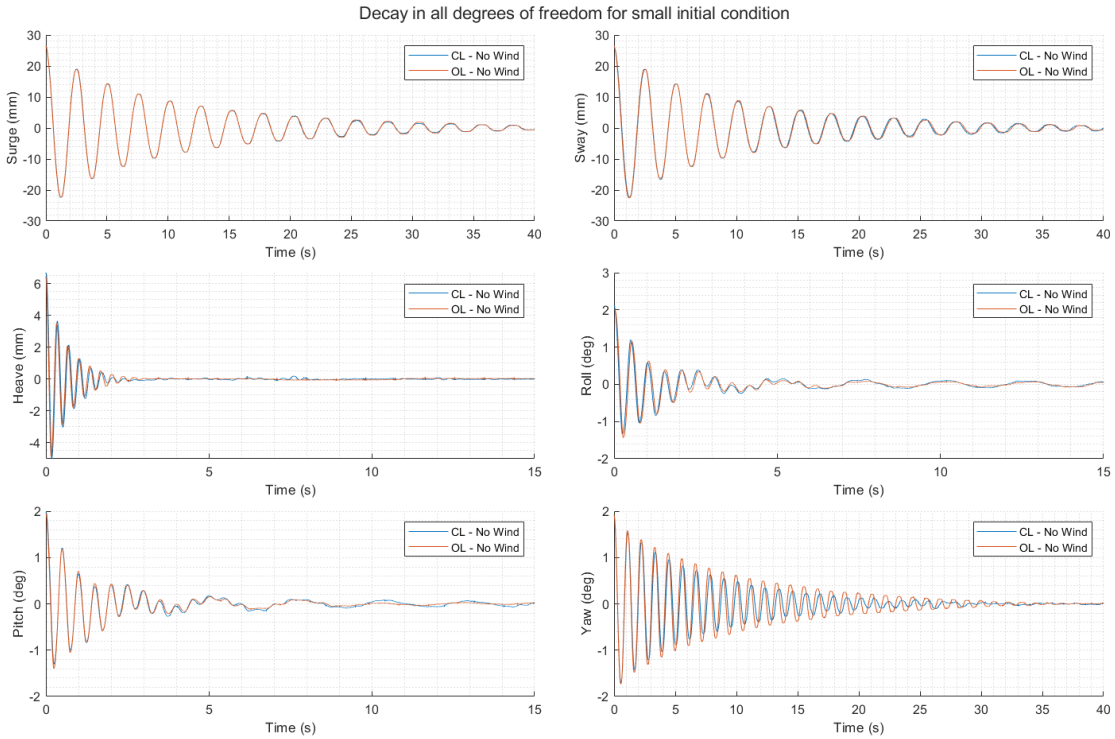

Figure C.1: Comparison of open-loop vs closed-loop - IC1 - QS mooring model

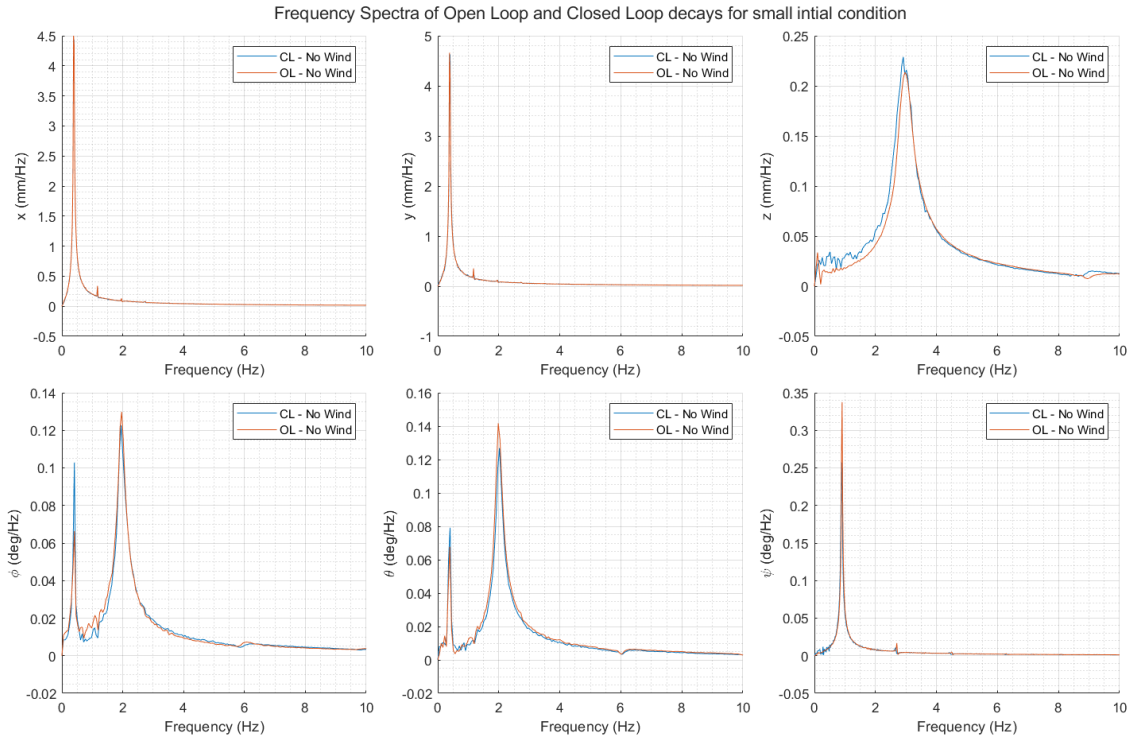

Figure C.2: Frequency spectra of open-loop and closed-loop - IC1 - QS mooring model

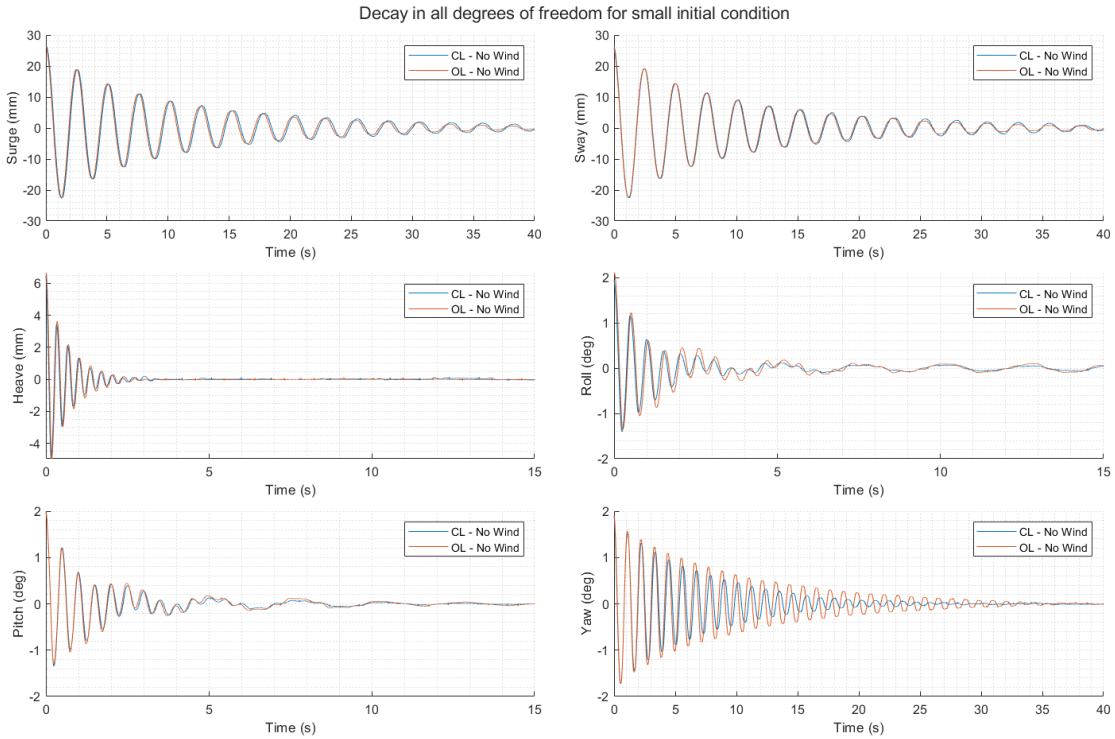

Figure C.3: Comparison of open-loop vs closed-loop - IC1 - lin mooring model

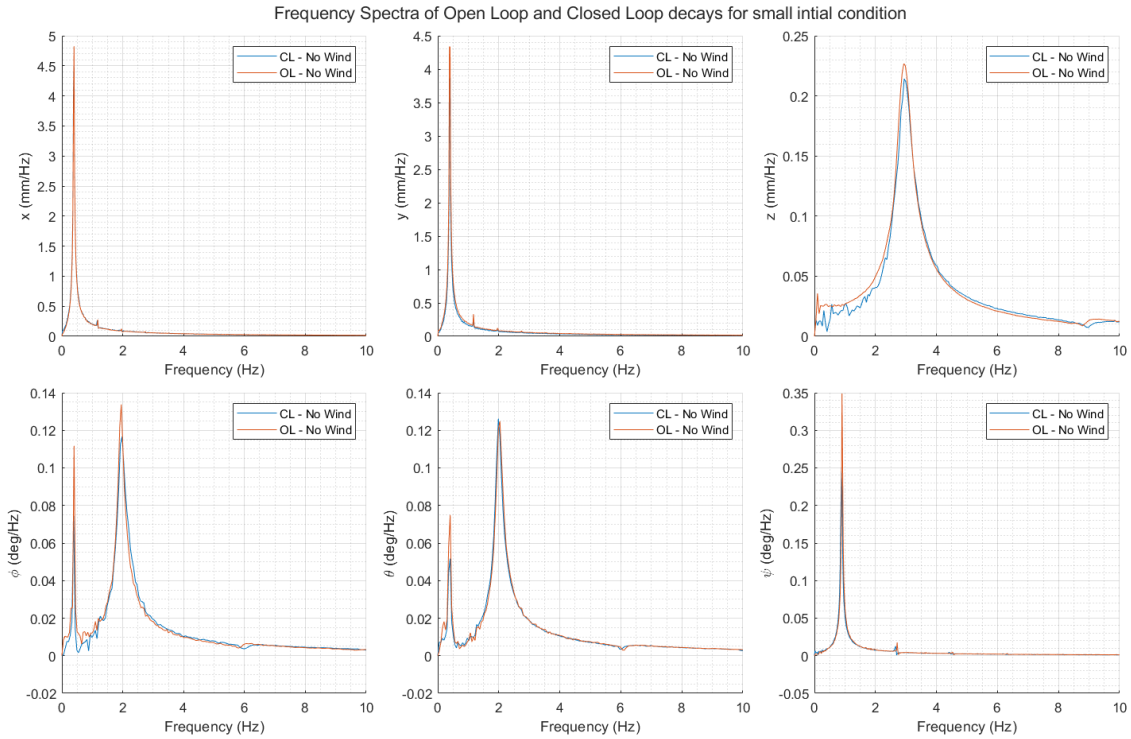

Figure C.4: Frequency spectra of open-loop and closed-loop - IC1 - lin mooring model

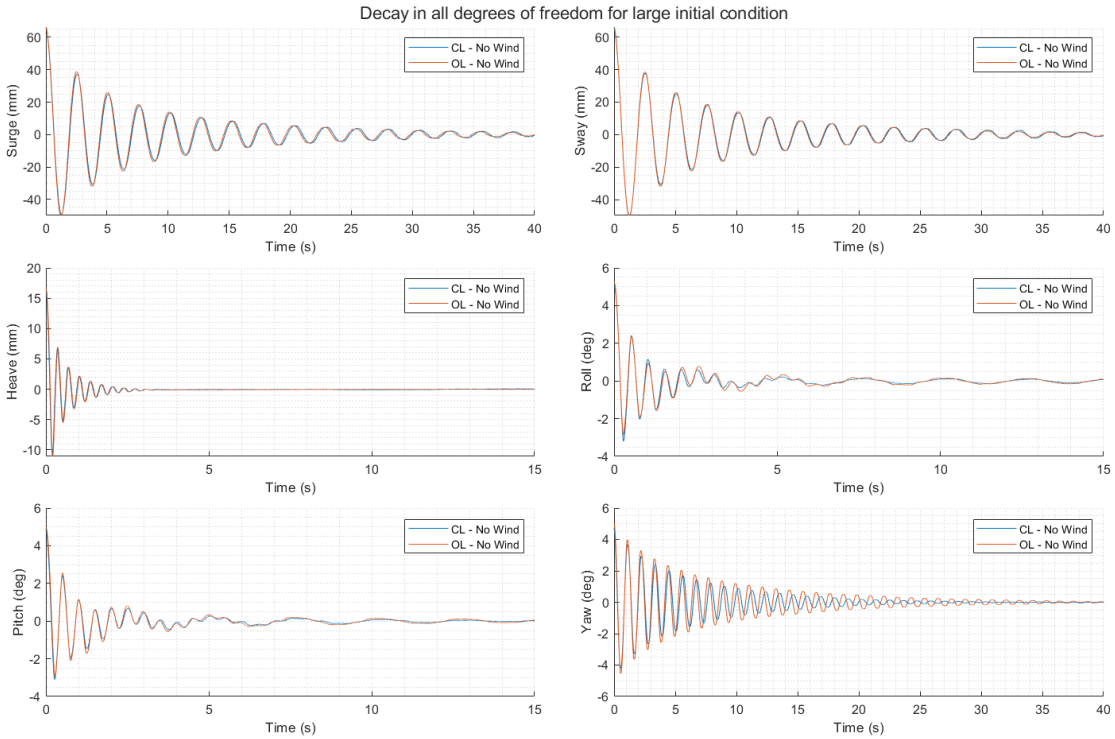

Figure C.5: Comparison of open-loop vs closed-loop - IC2 - lin mooring model

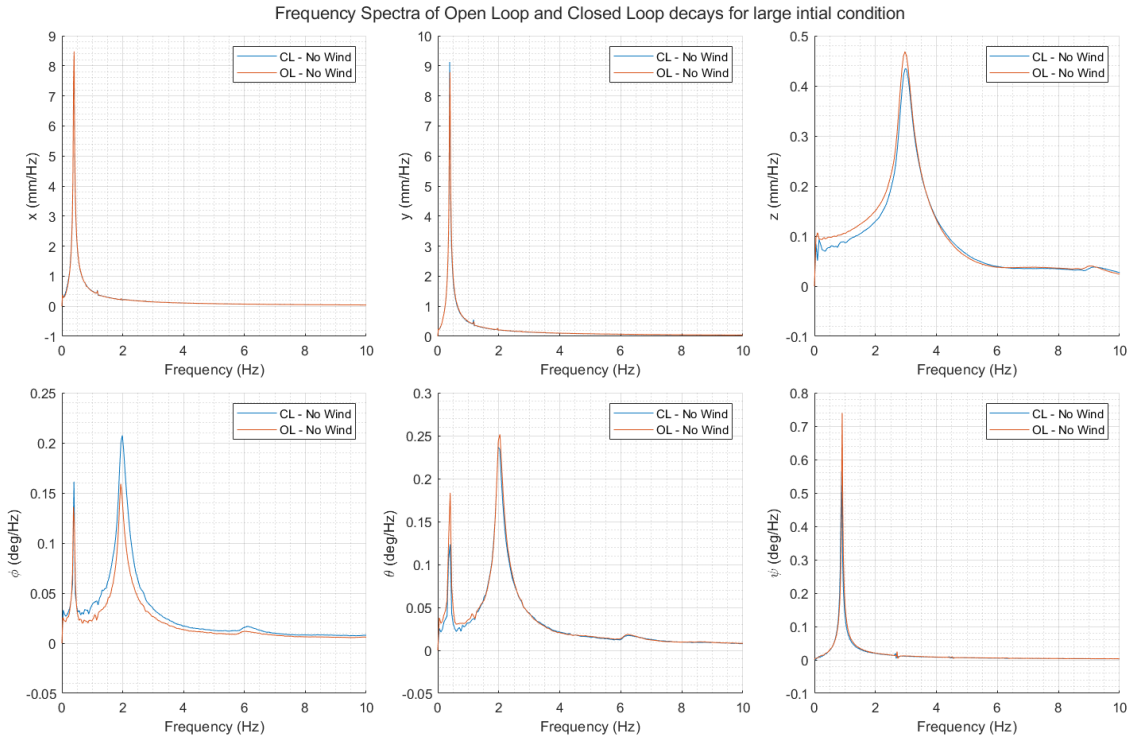

Figure C.6: Frequency spectra of open-loop and closed-loop - IC2 - lin mooring model

D

CPSD Figures

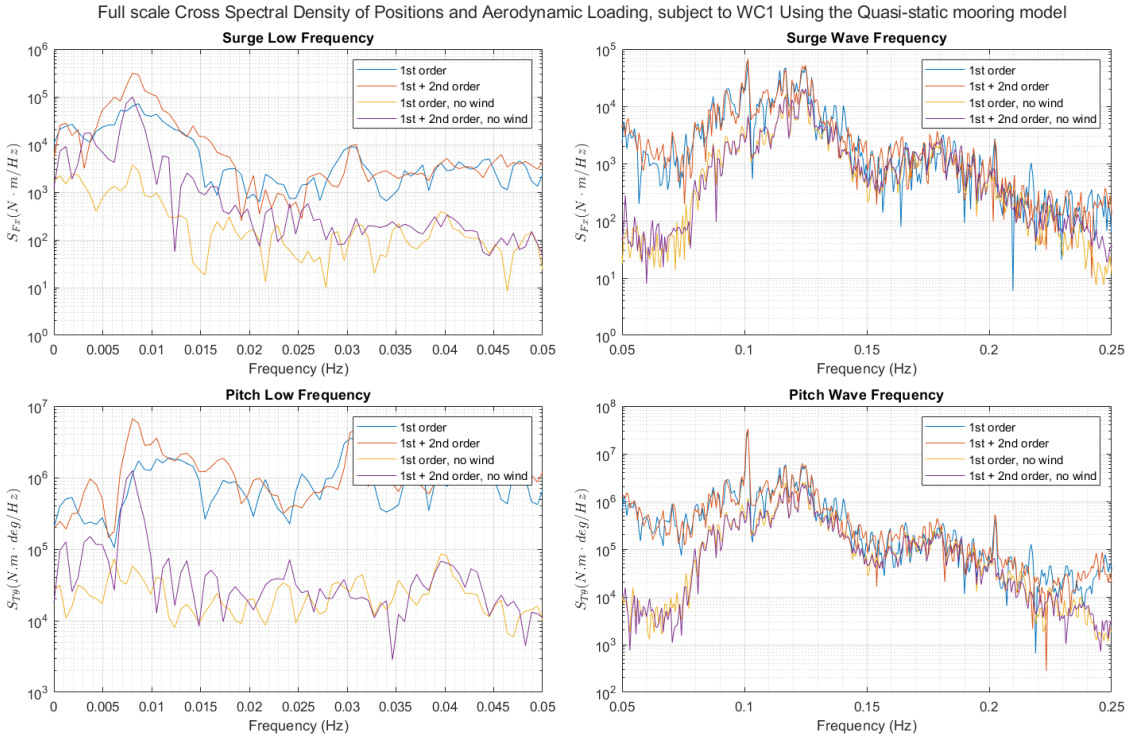

Figure D.1: Cross Spectral Density of aerodynamic surge force & surge position, and Aerodynamic pitching moment & pitch inclination, subjected to WC1.

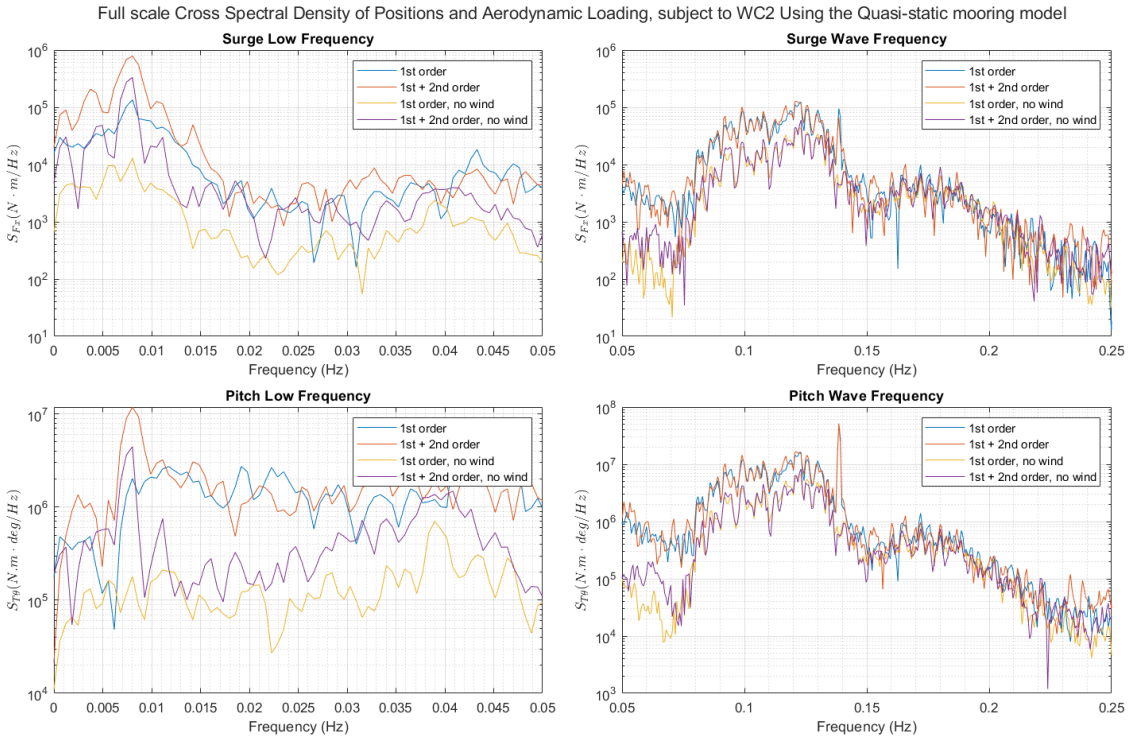

Figure D.2: Cross Spectral Density of aerodynamic surge force & surge position, and Aerodynamic pitching moment & pitch inclination, subjected to WC2.

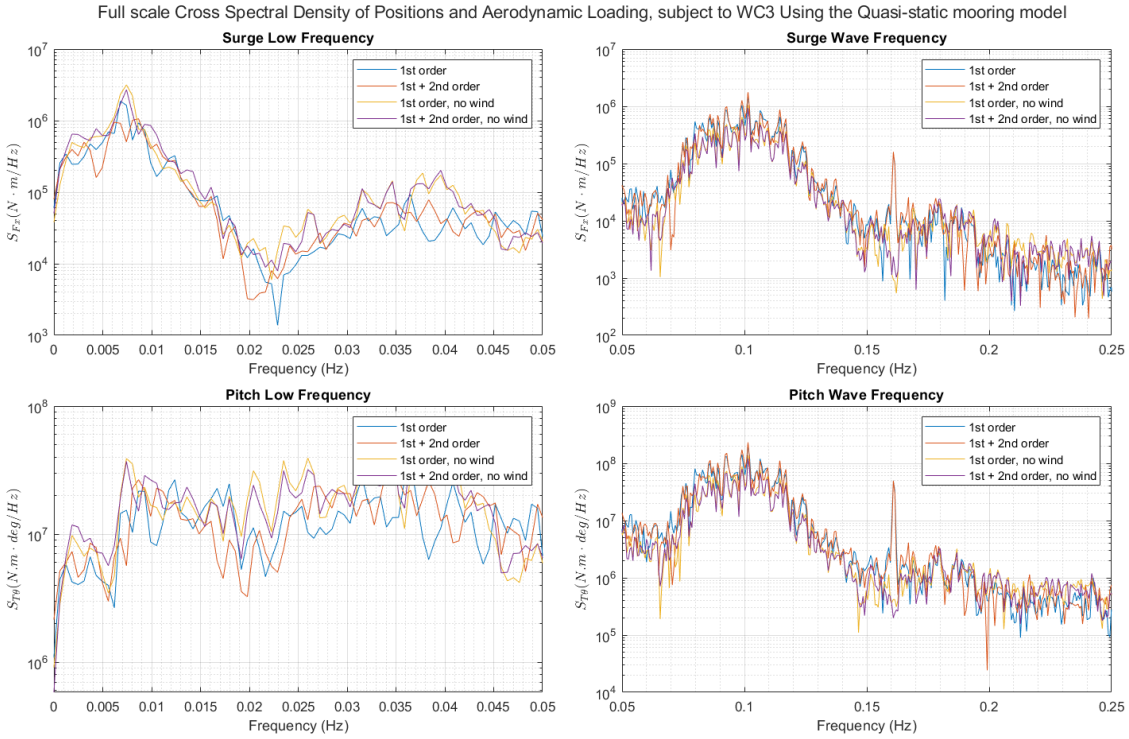

Figure D.3: Cross Spectral Density of aerodynamic surge force & surge position, and Aerodynamic pitching moment & pitch inclination, subjected to WC3.

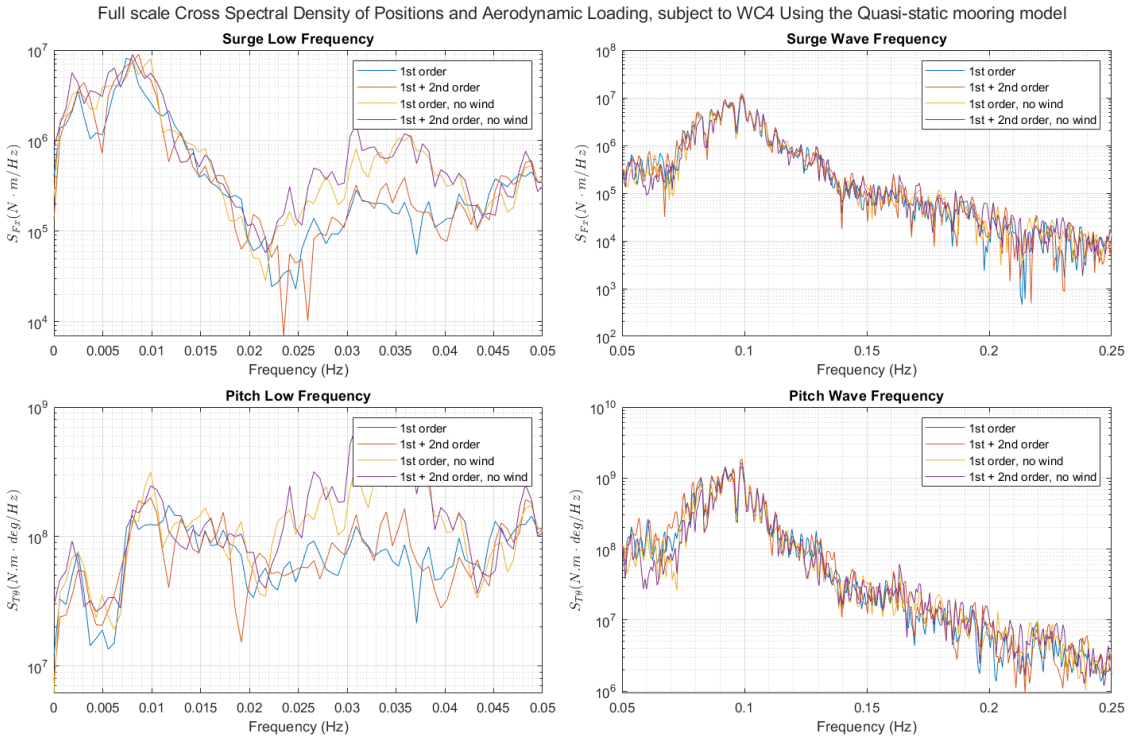

Figure D.4: Cross Spectral Density of aerodynamic surge force & surge position, and Aerodynamic pitching moment & pitch inclination, subjected to WC4.